Titre: Title:	Development of Accurate Voltage Source-based RMS Models of Type III and Type IV Wind Parks Suitable for Transient Studies
Auteur: Author:	Mingxuan Zhao
Date:	2025
Type:	Mémoire ou thèse / Dissertation or Thesis
Référence: Citation:	Zhao, M. (2025). Development of Accurate Voltage Source-based RMS Models of Type III and Type IV Wind Parks Suitable for Transient Studies [Thèse de doctorat, Polytechnique Montréal]. PolyPublie. https://publications.polymtl.ca/65822/

POLYTECHNIQUE MONTRÉAL

affiliée à l'Université de Montréal

Development of Accurate Voltage Source-based RMS Models of Type III and Type IV Wind Parks Suitable for Transient Studies

MINGXUAN ZHAO

Département de génie électrique

Thèse présentée en vue de l'obtention du diplôme de *Philosophiæ Doctor*

Génie électrique

Mars 2025

POLYTECHNIQUE MONTRÉAL

affiliée à l'Université de Montréal

Cette thèse intitulée :

Development of Accurate Voltage Source-based RMS Models of Type III and Type IV Wind Parks Suitable for Transient Studies

présenté par **Mingxuan ZHAO**

en vue de l'obtention du diplôme de *Philosophiæ Doctor*

a été dûment accepté par le jury d'examen constitué de :

Antoine LESAGE-LANDRY, président
Ilhan KOCAR, membre et directeur de recherche
Siqi BU, membre
Tao XUE, membre
Osman Bulent TOR, membre externe

ACKNOWLEDGEMENTS

First, I would like to thank my director Prof. Ilhan Kocar who supported me in many ways during my PhD. He has been very supportive, available and provided me all the guidance and advice I needed to realize my PhD project and develop my teaching skills.

Also, many thanks to Dr. Yuanzhu Chang and Dr. Tao Xue from the Hong Kong Polytechnic University for having me involved with their research projects and their supports with my thesis.

Moreover, I would like to thank DIgSILENT for providing access to PowerFactory and their support during modelling of wind parks.

Despite the distance, I will always be grateful to my parents for their unconditional support that allows me to chase my dreams. They are an important part of what I became.

Finally, a special thanks to EPRI and everyone else who helped me during my PhD for their support in different ways.

RÉSUMÉ

Avec le développement rapide des énergies renouvelables, l'intégration des ressources basées sur des onduleurs (IBR) dans le réseau à tous les niveaux de tension a considérablement augmenté ces dernières années. Parmi les IBR, les parcs éoliens (WP) représentent une part substantielle, leur capacité d'installation augmentant rapidement dans le monde entier. Des convertisseurs électroniques sont généralement nécessaires pour connecter les IBR au réseau électrique. Par exemple, les WP de type IV utilisent des générateurs synchrones (SG) pour produire de l'électricité. Cependant, la sortie des SG est intrinsèquement instable en termes de tension et de fréquence, ce qui nécessite l'utilisation de convertisseurs électroniques pour réguler leur sortie. Contrairement aux SG traditionnels, le comportement des IBR varie selon les différents scénarios, en fonction de la conception de leur contrôleur. Par conséquent, une modélisation précise des IBR est essentielle pour les études de systèmes électriques impliquant l'intégration des IBR. De nombreux outils logiciels existants, tels que les programmes de transitoires électromagnétiques (EMT) et MATLAB Simulink, fournissent des modèles détaillés des WP de type III et de type IV pour les simulations dans le domaine temporel et sont largement utilisés dans les études de systèmes électriques. Cependant, les simulations EMT pour les grands réseaux avec des niveaux élevés d'intégration IBR nécessitent beaucoup de calculs et prennent du temps, ce qui rend certaines études, telles que les analyses d'oscillation de puissance et de stabilité transitoire, difficiles. En revanche, les simulations RMS (Root Mean Square) sont efficaces sur le plan informatique et largement utilisées pour les études de systèmes électriques à grande échelle. Cependant, la plupart des modèles RMS existants de WP sont trop simplifiés, souvent représentés comme des sources de courant contrôlées. Cette simplification excessive peut conduire à des résultats inexacts ou même à des réseaux instables lorsque la pénétration IBR est élevée. Cette recherche vise à relever ces défis en étudiant les modèles WP de type III et de type IV existants, en développant ces modèles à partir de zéro dans PowerFactory et en les convertissant en modèles RMS adaptés aux études RMS. Contrairement aux modèles traditionnels basés sur la source de courant, les modèles RMS développés sont basés sur la source de tension et ressemblent étroitement à leurs homologues EMT. La précision de ces modèles RMS est validée par des études d'oscillation de puissance et de stabilité transitoire. En plus de fournir des résultats de simulation précis, les modèles RMS démontrent une efficacité considérablement améliorée, étant au moins dix fois plus rapides que les modèles EMT. Cette efficacité permet de réaliser des économies de

temps considérables dans les études par essais et erreurs. De plus, toutes les simulations sont réalisées dans le même environnement logiciel, ce qui élimine les erreurs potentielles liées à l'utilisation de plusieurs plateformes logicielles.

ABSTRACT

With the rapid development of renewable energy, the integration of inverter-based resources (IBRs) into the grid at all voltage levels has increased significantly in recent years. Among IBRs, wind parks (WPs) comprise a substantial portion, with their installation capacity growing rapidly worldwide.

Electronic converters are typically required to connect IBRs to the power grid. For example, Type IV WPs use synchronous generators (SGs) to produce power. However, the output of SGs is inherently unstable in terms of voltage and frequency, necessitating the use of electronic converters to regulate their output. Unlike traditional SGs, the behavior of IBRs varies across different scenarios, depending on their controller design. As a result, accurate modeling of IBRs is critical for power system studies involving IBR integration.

Many existing software tools, such as electromagnetic transient (EMT) programs and MATLAB Simulink, provide detailed models of Type III and Type IV WPs for time-domain simulations and are widely used in power system studies. However, EMT simulations for large networks with high levels of IBR integration are computationally intensive and time-consuming, making certain studies—such as power swing and transient stability analyses—challenging. In contrast, root mean square (RMS) simulations are computationally efficient and widely used for large-scale power system studies. However, most existing RMS models of WPs are overly simplified, often represented as controlled current sources. This oversimplification can lead to inaccurate results or even unstable networks when IBR penetration is high.

This research aims to address these challenges by studying existing Type III and Type IV WP models, developing these models from scratch in PowerFactory, and converting them into RMS models suitable for RMS studies. Unlike traditional current source-based models, the developed RMS models are voltage source-based and closely resemble their EMT counterparts. The accuracy of these RMS models is validated through power swing and transient stability studies. In addition to providing accurate simulation results, the RMS models demonstrate significantly improved efficiency, being at least ten times faster than EMT models. This efficiency enables substantial time savings for trial-and-error-based studies. Furthermore, all simulations are conducted within the same software environment, eliminating potential errors associated with using multiple software platforms.

TABLE OF CONTENTS

LIST OF TABLES

LIST OF FIGURES

LIST OF SYMBOLS AND ABBREVIATIONS

ARC	Auto Reclosure
AVM	Average Value Model
CCT	Critical Clearance Time
CSC	Coupled Sequence Controller
CT	Current Transformer
DFIG	Doubly Fed Induction Generator
DSC	Decoupled Sequence Controller
DSRF-PLL	Double Synchronous Reference Frame PLL
FRT	Fault Ride Through
FSC	Full Scale Converter
GSC	Grid Side Converter
HVRT	High Voltage Ride Through
IBR	Inverter Based Resource
LVRT	Low Voltage Ride Through
MPPT	Maximum Power Point Tracking
MSC	Machine Side Converter
OOS	Out of Step
OST	Out of Step Tripping

PF	Power Factory
PLL	Phase Locked Loop
PMSG	Permanent Magnet Synchronous Generator
POI	Point of Interconnection
POTT	Permissive Overreaching Transfer Trip
PSB	Power Swing Blocking
ROCOF	Rate of Change of Frequency
RSC	Rotor Side Converter
SFR	Stator Flux Reference
SG	Synchronous Generator
SRF-PLL	Synchronous Reference Frame PLL
SVR	Stator Voltage Reference
VT	Voltage Transformer
WP	Wind Park
WPC	Wind Park Controller
WT	Wind Turbine
WTG	Wind Turbine Generator

CHAPTER 1 INTRODUCTION

1.1 Motivation

With the rapid development of renewable energy, the integration of inverter-based resources (IBRs) into the grid at all voltage levels has increased significantly over the past few decades [1]. Among IBRs, wind parks (WPs) make up a significant portion, and their installation capacity has grown substantially worldwide [2].

IBRs, including solar plants and wind parks employing Type III (Doubly Fed Induction Generator, DFIG) and Type IV (Full-Scale Converter, FSC) wind turbine generators (WTGs), are connected to the grid via electronic converters [3]. These converters are necessary because many renewable sources, such as photovoltaic cells, generate DC power. Furthermore, some IBRs use synchronous generators (SGs) to produce power, but the output of SGs is typically unstable in terms of voltage and frequency. Electronic converters are therefore required to regulate the output, ensuring stability. With electronic converters, SGs can also operate over a wide range of speeds, improving the efficiency of IBRs [3].

Unlike traditional synchronous machines, IBRs exhibit varying behaviors under different scenarios. For example, while an SG may be represented as a voltage source behind an impedance in short-circuit studies, injecting significant positive sequence short-circuit current and providing a low-impedance path for negative sequence current, an IBR connected via electronic converters behaves differently depending on its controller design [4]. Consequently, accurately modeling IBRs is critical for conducting power system studies involving IBR integration.

Currently, in project-specific studies, many simulations—such as those for critical clearance time (CCT) and power swing—are conducted through trial-and-error, which is both time- and resource-intensive. Although electromagnetic transient (EMT) simulations have gained popularity in recent decades, root mean square (RMS) simulations remain the primary method for assessing transient stability in power systems. This is particularly true given the increasing complexity of large-scale networks and evolving [5-8]. In conventional power systems dominated by SGs, transient stability studies rely on theoretical calculations and numerical simulations [9]. With simplified SG models and algebraic networks, the essential dynamics of power systems in the positive-sequence domain can be simulated using RMS methods in mature software packages such as PSLF, PSSE, and

PowerFactory (PF). However, in modern power systems, IBRs like WPs are becoming critical power sources alongside SGs. Accurately representing IBRs in RMS and EMT simulations has become an important topic. RMS modeling of IBRs has been explored in numerous publications [10-13], and generic Type IV FSC WP models have been proposed under the leadership of organizations such as WECC, GE, and IEC [14-17].

In these generic FSC-based Type IV WP models, many control loops—including inner-loop control, phase-locked loop (PLL), and DC voltage control—are either simplified or removed, and WPs are represented as controlled current sources. Similarly, Type III WPs employing DFIGs with partially sized converters are often simplified as controlled current sources in parallel with fixed impedances, initializing these models remains a challenge because rotor variables must be calculated [18]. As the penetration rate of IBRs increases in modern power systems, IBR-driven instability is becoming a significant issue [19,20]. New phenomena and mechanisms related to IBR control have been explored in [21-23], introducing technical challenges for RMS simulations in transient studies. A large number of current sources in the network can cause numerical instability [24]. Furthermore, current source-based RMS models have been shown to produce significant errors in CCT assessments when compared with EMT results [25-26]. However, conducting EMT dynamic studies in routine work is inefficient because transient stability and power swing studies are performed case by case and through trial and error. Given the complexity of large-scale networks and the prevalence of IBRs in practical power systems, EMT simulations require significantly longer execution times than RMS simulations.

Some improvements to Type IV WTG RMS models have been proposed, such as using voltage source-based interfaces instead of controlled current sources [15,16]. Parameterization methods with modified controller designs have also been suggested to minimize differences between EMT and RMS models [20]. However, existing current source- and voltage source-based RMS models are built on the assumption of perfect voltage feedforward in inner-loop control. As a result, the current responses to reference variations and voltage dips are either removed or heavily simplified. This assumption is no longer valid for IBRs with imperfect voltage feedforward, as the resulting current response to voltage dips is significant. Additionally, because active current is inherently governed by DC voltage control, the dynamics of DC voltage and chopper protection are critical but often ignored in previous RMS models. In weak AC systems, these simplified dynamics can

significantly alter voltage profiles and affect the synchronization process [27,28]. Thus, using existing simplified RMS models for transient studies may lead to considerable errors.

1.2 Detailed EMT models

Reference [29] and [30] present detailed EMT models of Type III and Type IV WTGs. These models have formed the basis for various EMT studies. The structures of Type III and Type IV WTGs are shown in Fig. 1.1 and 1.2.

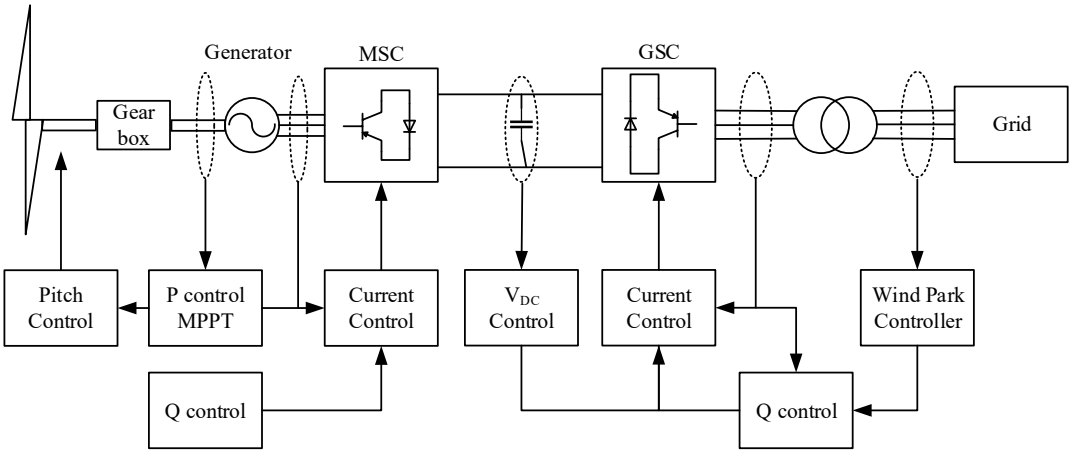

Fig. 1.1 Generic Type IV WP's EMT model

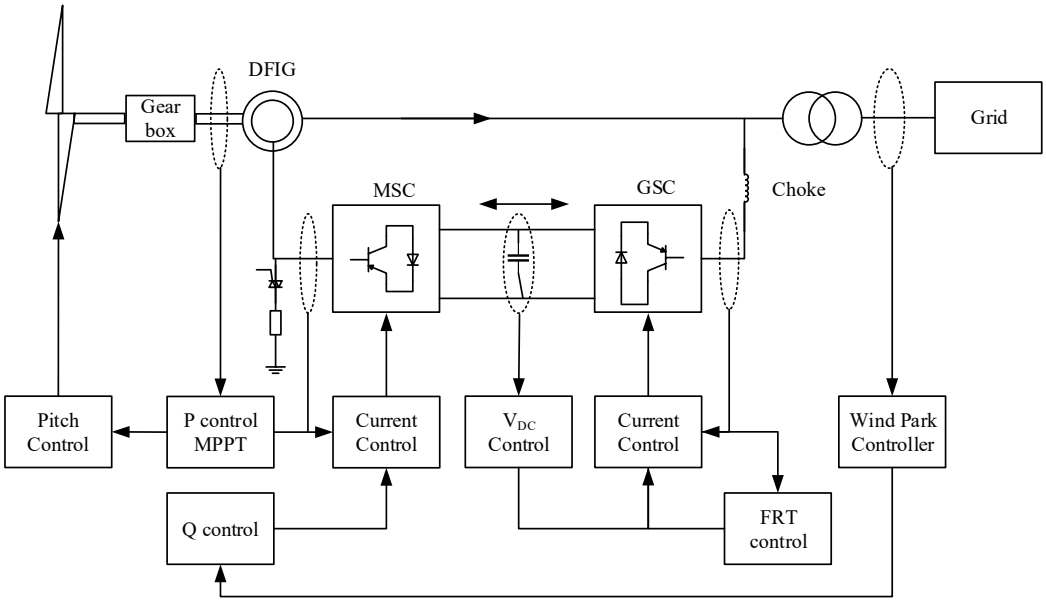

Fig. 1.2 Generic Type III WP's EMT model

As shown in Fig. 1.1 and Fig. 1.2, both models consist of mechanical wind turbine model, generators, back-to-back converters and DC bus. For Type IV WTG, machine side converter (MSC) is controlled by SG power output and Q setpoint at generator bus. Grid side converter (GSC) is controlled by DC bus voltage and Q setpoint at point of interconnection (POI). For Type III WTG, rotor side converter (RSC) is controlled by DFIG power output and Q setpoint at POI, and GSC is controlled by DC bus voltage and low voltage bus voltage. All converters are voltage source-based and their controllers employ outer voltage control loop and inner current control loop. These models have been widely used in wind park dynamic studies and have proven to be accurate.

1.3 Simplified EMT and RMS models

In PowerFactory (PF), the default library includes several wind park models, including Type III and Type IV models. However, these models are heavily simplified compared to the detailed EMT models described earlier.

Simplified Type IV WP Model

The simplified WECC Type IV WP model from PF is shown in Fig. 1.3. In this model:

- The SG, MSC, GSC, and DC bus are simplified into a controlled current source.
- The inner current control loop is removed, and the current reference signals generated by the outer control loop are fed directly into the controlled current source.

Simplified Type III WP Model

The simplified WECC Type III WP model from PF is shown in Fig. 1.4. In this model:

- The DFIG, RSC, GSC, and DC bus are also represented as a controlled current source.
- The inner current control loop is removed, and the model includes additional control loops to simulate the mechanical components of the wind park, such as the wind turbine and two-mass model linking the wind turbine to the DFIG rotor.

Limitations of Simplified Models

While these simplified models may provide reasonably accurate results for certain studies, they have significant limitations for transient studies where the dynamic behavior of the wind park heavily depends on the inner control loop. Key limitations include:

- Lack of Inner Control Dynamics:

The omission of the inner control loop leads to inaccurate modeling of current responses during voltage dips or reference variations.

- Oversimplification of Components:

Critical components, such as the SG, MSC, and GSC in Type IV models and the DFIG in Type III models, are replaced with controlled current sources, which fail to capture their true dynamic behavior.

- Potential Stability Issues:

Due to the current-source nature of these models, numerical stability issues may arise under certain conditions, as demonstrated in [25,26].

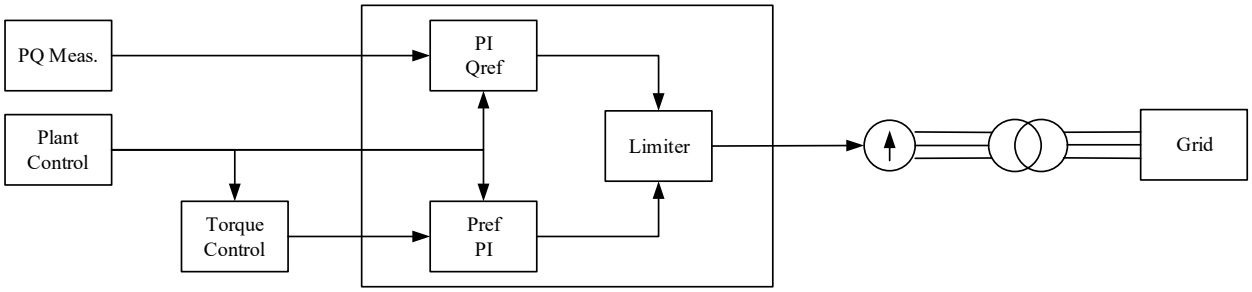

Fig. 1.3 Simplified current source-based model of Type IV WP

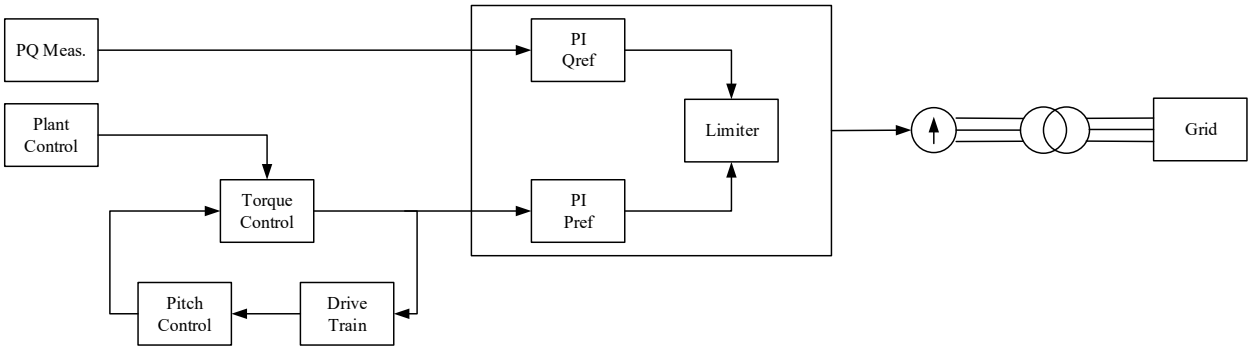

Fig. 1.4 Simplified current source-based model of Type III WP

This model is also heavily simplified. The DFIG, RSC, GSC and DC bus are all simplified into a controlled current source, and inner current control loop is removed. Compared with Type IV RMS model, this model includes extra control loops to simulate mechanical part of the wind park, including wind turbine and two mass model linking wind turbine to DFIG's rotor.

These simplified models might be able to provide accurate results for certain simulations. However, for transient studies where the transient behavior of wind park heavily depends on the inner control loop of the inner control loop [31-33], current source based will not provide accurate results compared with detailed EMT models. Furthermore, due to the current source nature of these models, under certain conditions it may even cause system stability issues, as demonstrated in [28].

Conclusion

The detailed EMT models provide the highest level of accuracy for studying the dynamic behavior of wind parks, making them indispensable for transient stability and fault ride-through studies. However, their computational intensity makes them less practical for large-scale networks or trial-and-error-based studies. Simplified EMT and RMS models, while computationally efficient, suffer from oversimplifications that reduce their accuracy in scenarios involving high IBR penetration.

1.4 Contributions

Detailed EMT Type III and Type IV Wind Park Models in PowerFactory

DIgSILENT PowerFactory (PF) is widely used in the power system industry; however, it lacks detailed EMT wind park (WP) models suitable for transient studies. The oversimplified default models in PF have some disadvantages and can lead to errors under certain scenarios. This research addresses these limitations by developing detailed EMT models of Type III and Type IV wind parks from scratch in PF.

The developed models include:

- A complete mechanical system comprising the wind turbine, two-mass model, and generator.
- Electrical components such as back-to-back converters, a DC bus, and a low-voltage grid.
- Detailed controller designs, including inner current control and outer voltage control loops.

Advanced protection features, such as DC bus chopper circuits and fault ride-through (FRT) capabilities, are also incorporated, as these features are mandated by many grid codes. These improvements make the developed EMT models more accurate and reliable for wind park dynamic studies. The model takes advantage of the advanced initialization algorithms of PF, which is typically burdensome in EMT tools.

Key Contribution:

The first major contribution of this research is the development of detailed and accurate EMT models of Type III and Type IV wind parks in PowerFactory.

Detailed RMS Type III and Type IV Wind Park Models in PowerFactory

EMT simulations are widely used for wind park studies due to their accuracy; however, they are computationally demanding. The small-time step required for EMT simulations makes them inefficient for long simulation periods, especially in trial-and-error-based studies. RMS simulations, on the other hand, are significantly faster due to their use of larger time steps and fundamental frequency simplification for the network side. However, existing RMS models of WPs in PF are oversimplified and inaccurate for certain studies, particularly transient stability assessments.

This research develops a new generation of Type III and Type IV RMS models that address these limitations:

- Type III RMS Model:

Unlike existing current source-based models, the proposed RMS model represents the power grid interface using an equivalent circuit. Voltage sources represent the internal voltages of the DFIG and GSC, in series with fixed impedances. This approach incorporates the dynamics of the DFIG and other control loops, significantly improving accuracy. Additionally, the proposed model eliminates the need for complicated rotor variable initialization, enabling easier setup and faster simulations.

- Type IV RMS Model:

The proposed RMS model for Type IV wind parks preserves the key components of the EMT model, including the SG, MSC, DC bus, and GSC. The MSC and GSC controllers are directly mapped from the EMT model, with modifications to accommodate RMS simulation signals. Although RMS solvers require different signal definitions compared to EMT solvers, the proposed design closely resembles the EMT counterpart, enhancing accuracy in capturing transient behaviors.

Key Contribution:

The second major contribution is the development of detailed RMS models for Type III and Type IV wind parks, which provide high accuracy and computational efficiency for transient studies.

Improvements on Voltage Source-Based Type IV Wind Park Models

Previous studies have proposed Type IV WTG RMS models utilizing voltage source-based interfaces instead of controlled current sources. While these models are an improvement over current source-based models, they still rely on the assumption of perfect voltage feedforward in the inner control loop such as the one shown Fig. 1.5 available in PF library. This assumption oversimplifies the response of current reference signals to voltage dips, often leading to significant errors in transient studies.

This research addresses these issues by:

- Reconstructing inner control loops to account for imperfect voltage feedforward, which better represents current response dynamics during voltage dips.
- Simulating DC bus dynamics and chopper protection to capture the full transient behavior of the wind park.
- Interfacing the RMS model with the power grid using an equivalent circuit consisting of a voltage source behind a fixed impedance, similar to the RMS model of a synchronous generator.

Key Contribution:

The third major contribution is the development of an improved voltage source-based RMS model for Type IV wind parks, which provides more accurate simulations of transient stability and power swing studies.

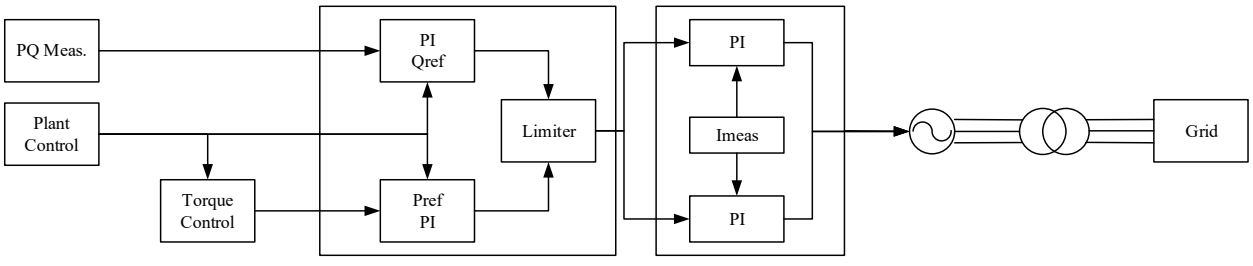

Fig. 1.5 Simplified voltage source based model of Type IV WP

Accurate EMT and RMS Wind Park Simulation Packages within a single software platform

Different software platforms often employ varying EMT/RMS engine designs and solver options (e.g., error margins, maximum iterations, and initialization methods). As a result, even identical EMT or RMS models may produce minor discrepancies when simulated on different platforms. This issue is further exacerbated when EMT and RMS models need to be compared, as errors can arise from differences in software design rather than the models themselves.

This research addresses these challenges by:

- Developing detailed EMT and RMS wind park models within the same software platform, PowerFactory.
- Ensuring consistent solver parameters for both EMT and RMS simulations, thereby eliminating potential errors caused by differences in software environments.

1.5 Methodology

To develop accurate wind park (WP) models from scratch, this research adopts a hierarchical approach encompassing mathematical modeling, model construction, verification, simulation, and analysis. The methodology is designed to address the limitations of existing Type III and Type IV wind park models, particularly in transient stability and power system studies. The following steps outline the research process:

1.5.1 Mathematical modeling of WPs

A generalized mathematical model for Type III and Type IV wind parks is developed as the foundation for constructing both EMT and RMS models. The mathematical model includes the following components:

- Mechanical Systems:

The wind turbine, two-mass model, and generator dynamics are fully represented.

- Electrical Systems:

Includes the synchronous generator (Type IV) or doubly fed induction generator (Type III), machine-side converter (MSC), rotor-side converter (RSC), grid-side converter (GSC), DC bus, and low-voltage grid.

- Control Systems:

Outer voltage control loops, inner current control loops, DC bus voltage control, and phase-locked loop (PLL) dynamics are modeled in detail.

This comprehensive mathematical model forms the basis for constructing detailed EMT and RMS models in PowerFactory.

1.5.2 Type III and Type IV EMT model

Using the mathematical models, detailed EMT models of Type III and Type IV wind parks are constructed in PowerFactory. These models include:

- Type IV EMT Model:

Includes a synchronous generator (SG) connected to the grid via back-to-back converters (MSC and GSC) and a DC bus. The MSC controls the SG's power output while maintaining the reactive power setpoint at the generator bus. The GSC regulates the DC bus voltage and the reactive power setpoint at the point of interconnection (POI). The control system is implemented with inner and outer control loops for maximum accuracy.

- Type III EMT Model:

Includes a doubly fed induction generator (DFIG) whose stator is directly connected to the grid and rotor is connected via the RSC and GSC. The RSC regulates the DFIG's power output and reactive power at the POI, while the GSC maintains the DC bus voltage and low-voltage bus voltage. The model also features advanced control mechanisms, such as fault ride-through (FRT) and DC bus chopper protection.

The constructed EMT models are simulated in benchmark systems and compared against existing EMT models in EMTP to ensure accuracy.

1.5.3 Type IV RMS model via direct mapping

Direct mapping method is used to obtain a detailed RMS model of Type IV WP. With this method, the exact same controller design is mapped from the EMT model, while minor changes are made to PLL, abc to dq and dq to abc transformation blocks to work with RMS signals. Detailed steps include:

- Component Mapping:

Each component of the EMT model, including the SG, MSC, GSC, and DC bus, is represented in the RMS model.

- Controller Adaptation:

The MSC and GSC controllers are mapped from the EMT model, with modifications to account for differences in signal definitions between EMT and RMS solvers (e.g., RMS solvers use phasors rather than instantaneous values).

- Adjustments for RMS Simulation:

Voltage and current measurements, PLLs, and abc-to-dq transformations are adapted for RMS simulations. Controller parameters are tuned to ensure stability and accuracy.

The RMS model is verified through simulations in benchmark systems and compared with EMT results. This method could also be applied to Type III WP and all other IBRs modelling in RMS simulation software.

1.5.4 Improved voltage source-based Type IV RMS model

To address the limitations of existing voltage source-based Type IV RMS models, this research develops an improved model that includes:

- DC Bus Dynamics:

Unlike existing models, the proposed RMS model calculates DC bus voltage dynamics analytically, capturing transient behavior during faults.

- Inner Control Loop Reconstruction:

The inner control loops of the MSC and GSC are reconstructed to account for imperfect voltage feedforward, which significantly improves the accuracy of current response to voltage dips.

- Equivalent Circuit Interface:

The grid interface is represented as a voltage source behind a fixed impedance, similar to the RMS model of a synchronous generator.

The improved RMS model is validated in power swing and transient stability studies, demonstrating its superior accuracy compared to existing simplified models.

1.5.5 Improved voltage source-based Type III RMS model

Since RMS simulation only runs in fundamental frequency, differential terms in the mathematical modelling equations could be omitted and a simplified model is obtained. By regrouping terms in the simplified equations, the Type III WTG model could be represented by two internal voltage source models. An improved RMS model for Type III wind parks is developed with the following features:

- DFIG Dynamics:

The dynamics of the DFIG, including rotor and stator interactions, are modeled using an internal voltage source approach.

- Control Systems:

The RSC and GSC controllers are adapted to RMS simulations, incorporating DC bus dynamics, PLL synchronization, and outer-loop controls for active and reactive power regulation.

- Simplified Initialization:

Unlike conventional models, the proposed RMS model eliminates the need for complex rotor variable initialization, simplifying the setup process.

The proposed model is simulated in benchmark systems and verified against EMT results. The same simplification and modelling method could also be applied to other types of IBRs to obtain accurate voltage source-based models.

1.5.6 Simulation and verification of developed models

Power swings are typically studied through trial-and-error simulations, where fault resistance and fault clearance times are iteratively adjusted to determine the system's stability limits. This research uses the developed EMT and RMS models to conduct power swing studies in the PRSC D6 benchmark system, which includes:

- Power Swing Blocking (PSB) Protection:

The performance of PSB relays is analyzed using the developed models, revealing potential errors caused by existing current source-based RMS models under high wind penetration levels.

- Out-of-Step (OOS) Protection:

The accuracy of OOS protection settings is assessed under different scenarios (e.g., 25% and 50% wind generation).

CCT studies are another trial-and-error-based analysis where fault durations are iteratively adjusted to determine the system's transient stability limits. This research integrates the proposed EMT and RMS models into the EPRI benchmark system to conduct CCT studies under various scenarios:

- Transient Stability Assessment:

The CCT of the system is evaluated under different wind penetration levels, with comparisons made between EMT and RMS simulation results.

- Validation of Proposed Models:

The accuracy of the proposed RMS models is validated by comparing their CCT results with those from detailed EMT simulations. The advantages of RMS simulations (e.g., faster execution times) over EMT simulations are also demonstrated, highlighting the proposed RMS models' computational efficiency and accuracy.

1.5.7 Applicability of RMS modelling method

The RMS modelling method mentioned above could also be applied to other IBR types, such as Type IV WPs, photovoltaic (PV) plants and battery storage systems due to their converter-based nature. By simplifying differential terms in dynamic equations of their mathematical model, all IBRs could be simplified and represented by internal voltage sources, which will significantly improve RMS simulation’s accuracy over existing current source-based models.

1.6 Limits

This research project focuses coupled sequence controller (CSC). In this control method, negative sequence components are not decoupled for control, double frequency oscillation on the DC bus may be observed under unbalanced grid conditions. Decoupled sequence controller (DSC) has been proposed to control negative sequence components under such scenarios and can also be used to inject negative sequence currents into the system under unbalanced conditions. The DSC scheme for Type IV EMT WP model has been implemented in PF but due to time constraints, it is not tested extensively.

Due to limits posed by RMS solver which only simulates the system in fundamental frequency, negative sequence components injection and decoupling needs further research. Further improvements on the developed model, such as tuning of the controller parameters under different grid strengths, are also possible and will further improve the models' stability.

CHAPTER 2 MATHEMATICAL MODELLING OF WP

2.1 Type IV WP model

Type IV wind turbine generator is connected to the grid through full-scale converters. Typical type 4 wind turbine consists of wind turbine, synchronous generator and PWM converter.

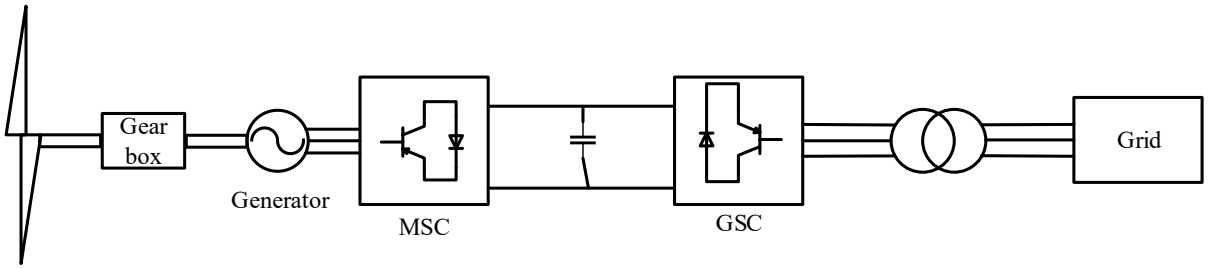

Fig. 2.1 Generic Type IV WP model

Fig. 2.1 shows the construction of a typical type 4 wind turbine generator. Both synchronous generators, including permanent magnet synchronous generator (PMSG) and electrical excited synchronous generator, and induction motors can be used in wind turbine. In practice, type 4 WTGs based on PMSG is widely used and studied, therefore it will be the focus of this paper.

The gearbox in Fig. 2.1 can be omitted and the PMSG will be driven directly by the wind turbine, improving system efficiency and stability. However, high-powered multipolar PMSGs are difficult to design, manufacture and maintain, therefore a low gear ratio gearbox is usually preferred to reduce the size and manufacturing cost of PMSGs.

Power is generated by the synchronous generator, rectified to DC by the machine side converter, filtered by DC bus capacitor, then fed into AC side via grid side converter. Because type 4 wind turbine is connected to the grid via PWM converter, different control schemes could be applied to the converter to achieve flexibility. For instance, reactive current contribution from WTG during a fault can be controlled directly by the controller, enhancing the stability of WTG during different grid disturbance situations.

2.1.1 Components of Type IV WTG

2.1.1.1 Two-mass model

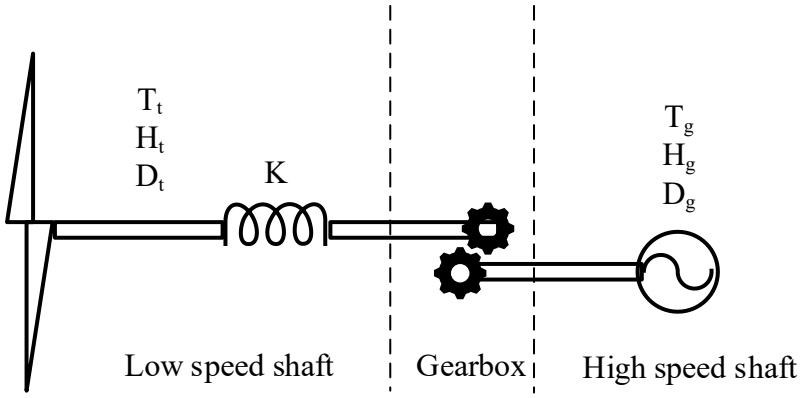

Fig. 2.2 Two-mass model of wind turbine

The mechanical part of the WTG can be modelled with two mass model. As shown in Fig. 2.2, the two-mass model consists of low-speed shaft connected to wind turbine, gearbox and high-speed shaft which is connected to the generator. It can be expressed as:

$$\begin{aligned} 2H_t \frac{\mathrm{d}\omega_T}{\mathrm{d}t} &= T_t - K\theta_s - D_t\omega_t \\ 2H_g \frac{\mathrm{d}\omega_g}{\mathrm{d}t} &= K\theta_s - T_g - D_g\omega_g \\ \frac{\mathrm{d}\theta_s}{\mathrm{d}t} &= \omega_0(\omega_t - \omega_g) \end{aligned} \tag{2.1}$$

Where H_t and H_g are inertial time constants of wind turbine and generator, K is the shaft's rigidity coefficient, D_t and D_g are damping coefficients of wind turbine shaft and generator rotor. T_t and T_g are mechanical torque on the wind turbine and generator shaft, respectively. ω_t and ω_g are the rotational speed of wind turbine shaft and generator rotor. θ_s is angular displacement between the two masses.

2.1.1.2 Wind turbine model

Wind power is extracted by the wind turbine as kinetic energy, which is calculated by:

$$P_t = \frac{1}{2}\rho A\upsilon^3 C_p(\lambda,\beta) \tag{2.2}$$

Where ρ is density of air, A is sweep area of the wind turbine, υ is wind speed and C_p is wind power coefficient. C_p is a property of the wind turbine, and is usually determined by a set of curves, which is a function of tip-to-speed ratio λ and blade pitch angle β. Tip-to-speed ratio is calculated as:

$$\lambda = \frac{(\omega_t R)}{\upsilon} \tag{2.3}$$

Where R is blade radius and ω_t is wind turbine's rotational speed. Given a specific pitch angle, there exists a λ value that maximizes C_p. Therefore, the C_{pmax} curve can be obtained as shown in Fig. 2.3.

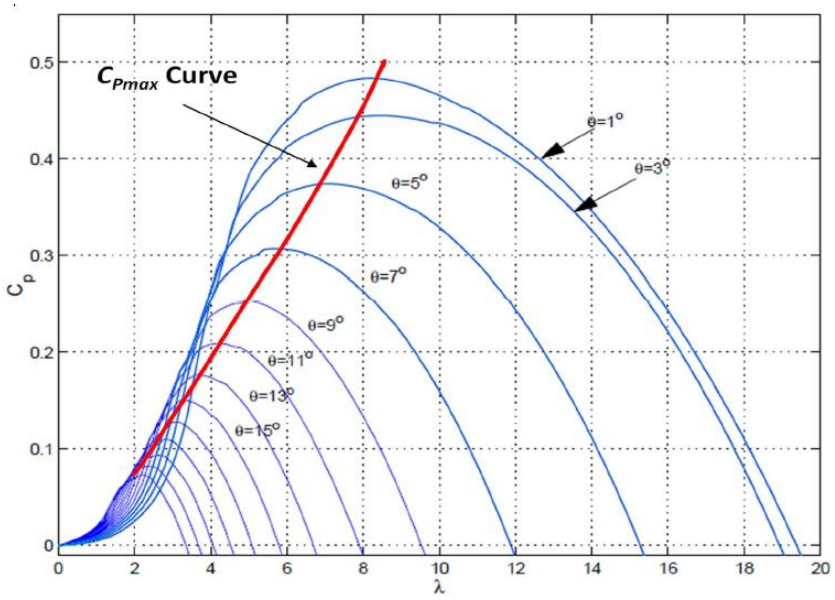

Fig. 2.3 C_{pmax} curve plot

2.1.1.3 PMSG model

Unlike externally excited synchronous motors, PMSG is excited by permanent magnets embedded on its rotor. To obtain PMSG's mathematical model in dq reference frame, following assumptions are made:

Iron core saturation effect is ignored;

Hysteresis loss and eddy current loss are ignored;

Permanent magnets generate perfect sinusoidal magnetic flux distribution in stator winding

Stator voltage in dq reference frame can be expressed as:

$$u_{sd} = r_s i_{sd} + \frac{\mathrm{d}\psi_{sd}}{\mathrm{d}t} - \omega_e \psi_{sq}$$
$$u_{sq} = r_s i_{sq} + \frac{\mathrm{d}\psi_{sq}}{\mathrm{d}t} + \omega_e \psi_{sd} \tag{2.4}$$

Where u_{sd}, u_{sq} are stator voltages, i_{sd}, i_{sq} are stator currents, r_s is stator resistance, ψ_{sd}, ψ_{sq} are flux linkages on d and q axes, respectively. ω_e is electrical angular frequency of the generator, which is calculated as:

$$\omega_e = n\omega_r \tag{2.5}$$

Where n is the number of pole-pairs and ω_r is angular frequency of the generator rotor. Flux linkage is obtained as:

$$\psi_{sd} = L_d i_{sd} + \psi_{PM}$$
$$\psi_{sq} = L_q i_{sq} \tag{2.6}$$

ψ_{PM} denotes flux linkage from permanent magnet. Substituting (2.6) into (2.4):

$$\frac{\mathrm{d}i_{sd}}{\mathrm{d}t} = \frac{1}{L_d}(u_{sd} - r_s i_{sd} + \omega_e L_q i_{sq})$$
$$\frac{\mathrm{d}i_{sq}}{\mathrm{d}t} = \frac{1}{L_q}(u_{sq} - r_s i_{sq} - \omega_e (L_d i_{sd} + \psi_{PM})) \tag{2.7}$$

Due to the symmetrical structure of a PMSG rotor, it can be assumed that d axis and q axis inductance are the same, therefore:

$$\frac{\mathrm{d}i_{sd}}{\mathrm{d}t} = \frac{1}{L}u_{sd} - \frac{1}{L}r_s i_{sd} + \omega_e i_{sq}$$
$$\frac{\mathrm{d}i_{sq}}{\mathrm{d}t} = \frac{1}{L}u_{sq} - \frac{1}{L}r_s i_{sq} - \omega_e i_{sd} - \frac{1}{L}\omega_e \psi_{PM} \tag{2.8}$$

The real and reactive power of PMSG can be calculated as:

$$P = \frac{3}{2}(u_{sd} i_{sd} + u_{sq} i_{sq})$$
$$Q = \frac{3}{2}(u_{sq} i_{sd} - u_{sd} i_{sq}) \tag{2.9}$$

The electromagnetic torque of PMSG is:

$$\begin{aligned} T_e &= \frac{3}{2} n(\psi_{sd} i_{sq} - \psi_{sq} i_{sd}) \\ &= \frac{3}{2} n((L_d - L_q) i_{sd} i_{sq} + \psi_{PM} i_{sq}) \\ &= \frac{3}{2} n \psi_{PM} i_{sq} \end{aligned} \tag{2.10}$$

Where ψ_{PM} is flux linkage of permanent magnet rotor, n is number of pole pairs. Simplification is based on previous assumption, i.e. L_d=L_q=L.

2.1.1.4 PWM Converter

Type 4 WTG uses full scale three-phase PWM rectifier and inverter to construct the back-to-back FSC. Due to PWM converter's operating characteristics, relatively small time-step is required for accurate simulation. Therefore, average value model (AVM) can be used to represent PWM converters without sacrificing accuracy for fundamental frequency studies. AVM model of FSC converters is shown in Fig. 2.4.

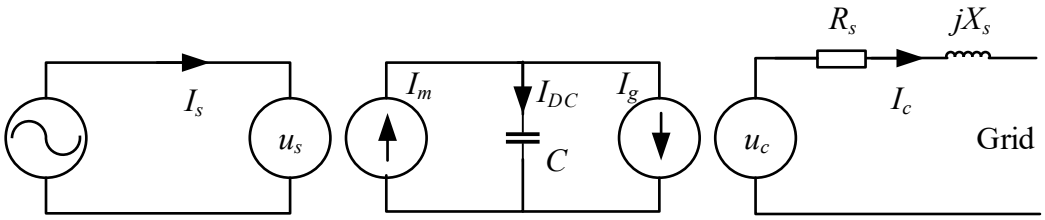

Fig. 2.4 AVM model of FSC

The dynamics of DC bus capacitor can be written as:

$$I_m - I_g = C \frac{\mathrm{d}U_{dc}}{\mathrm{d}t} \tag{2.11}$$

Where I_m is the DC current injected by the machine side converter, and I_g is the DC current drawn by the grid side converter. The active and reactive current of the GSC can be written as:

$$\begin{aligned} P &= \frac{3}{2}(u_{cd} i_{cd} + u_{cq} i_{cq}) \\ Q &= \frac{3}{2}(u_{cq} i_{cd} - u_{cd} i_{cq}) \end{aligned} \tag{2.12}$$

In steady state, machine side converter current I_m equals to grid side converter current I_g, therefore no current flows through the capacitor, and DC bus voltage U_{DC} is constant. During transients, $I_m \neq I_g$ and $I_{DC}=I_m-I_g$ flows through the capacitor, and DC bus voltage will fluctuate.

In above AVM model, all losses are ignored, including switching loss of PWM converters. If losses are to be included in the model, they will be represented by resistors placed on DC bus. Therefore, the following power equation can be obtained:

$$U_{dc} I_g + \sqrt{3}\,\mathrm{Re}(\mathbf{u}_c \mathbf{i}_c) = 0 \tag{2.13}$$

Where $\boldsymbol{u}_c$ and $\boldsymbol{i}_c$ are GSC AC side voltage and currents. Re () is the real part of a complex number, Im () is the imaginary part of a complex number, bold letters represent phasor quantities in this and all following equations.

2.1.1.5 Choke filter

Choke filter is used to filter out high frequency harmonics generated by the PWM converter. It is placed in series with GSC and connects it to LV grid.

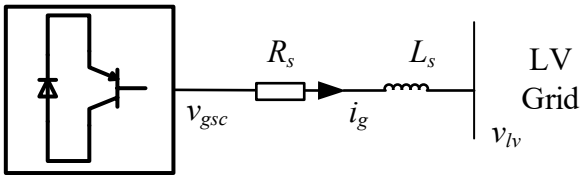

Fig. 2.5 Choke filter circuit

The voltage equation of series reactor is given by:

$$\mathbf{v}_{lv} = R\mathbf{i}_g + L\frac{\mathrm{d}\,\mathbf{i}_g}{\mathrm{d}\,t} + \mathbf{v}_{gsc} \tag{2.14}$$

Where $\boldsymbol{v}_{lv}$ is voltage on LV bus, $\boldsymbol{v}_{gsc}$ is voltage of GSC, $\boldsymbol{i}_g$ is current output of GSC, R_s and L_s are resistance and inductance of the choke filter, respectively.

2.1.1.6 Harmonics filter

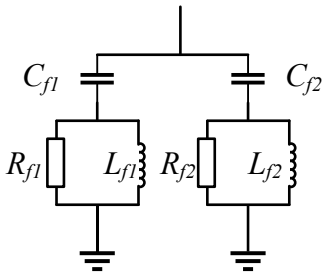

Fig. 2.6 Harmonics filter circuit

Harmonics filter is placed on low voltage bus to filter out high frequency harmonics. Two filters of identical reactive power Q_{filter} are used, one with cut-off frequency tuned at switching frequency of PWM converter, another one with cut-off frequency set at two times the switching frequency. Filter's resistance, capacitance and inductance are calculated as:

$$\begin{aligned} C_f &= \frac{Q_{filter}}{\omega_s V_{lv}^2} \\ L_f &= \frac{1}{C_f (2\pi f_c)^2} \\ R_f &= 2\pi f_c L_f Q_f \end{aligned} \tag{2.15}$$

Where f_c is cut-off frequency, V_{lv} is low voltage bus voltage, ω_s is angular frequency of grid voltage and Q_f is quality factor of the filter.

2.1.1.7 Collector grid and transformers

The PWM converter is connected to the external grid via wind turbine transformer, collector grid and wind park transformer. Collector grid is modeled as a PI circuit, and simple two-winding transformer model is used for transformers. It is worth noting that MVA rating of transformers are combined rating from all wind turbines as this model is an aggregated model.

2.1.2 Control system for Type IV WTG

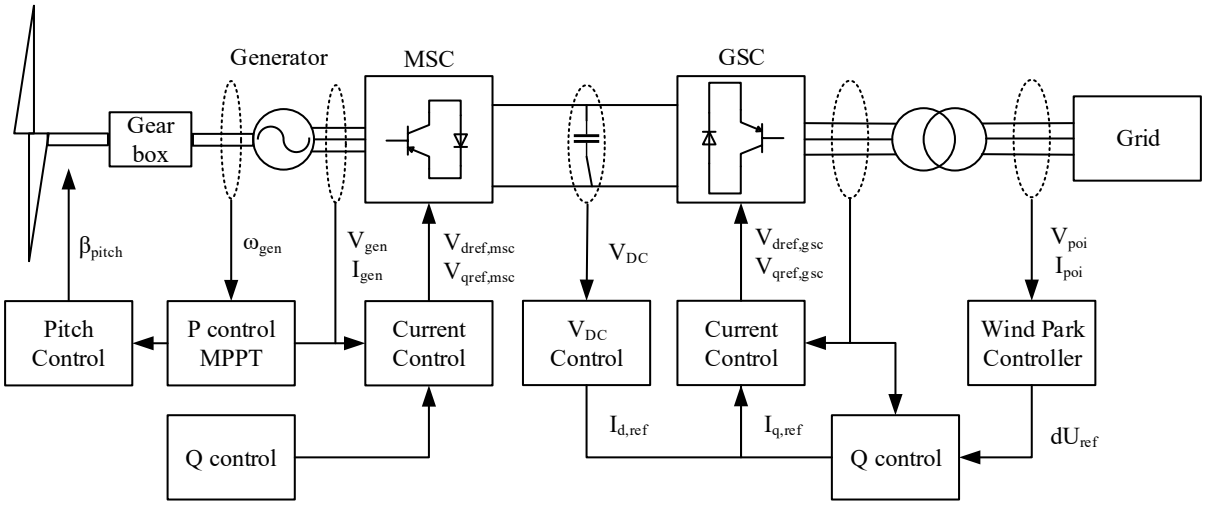

Fig. 2.7 Type IV WP controller model

The basic block diagram of a coupled Type IV FSC WTG controller design is given in Fig. 2.7. Due to the nature of FSC WTG, the synchronous machine and the grid are completely decoupled. Therefore, the dynamics of the WTG is determined completely by the controller. The FSC controller consists of two fully decoupled parts, MSC controller and GSC controller. GSC works as an inverter that draws power from DC bus and injects into grid side. The goals of GSC controller are:

- Control DC bus voltage;
- Control reactive power injection at POI.

The MSC works as a rectifier and converts AC power generated by PMSG into DC. In this model a three-phase PWM converter is used for optimal generator control. For simplification, a three-phase full bridge rectifier based on diodes could also be used to connect the generator to DC bus. The goals of MSC controller are:

- Maximize power extraction at given generator speed;
- Control generator voltage.

A pitch controller is also included to prevent overspeed by controlling wind turbine's pitch angle.

2.1.2.1 Measurement filters

All measured signals are passed through a low pass filter to filter out high frequency harmonics caused by the switching of PWM converter. In this model, a second order Butterworth filter is used to filter out high frequency harmonics. The transfer function of the filter is given by:

$$H_f(s) = \frac{1}{1 + \frac{\sqrt{2}s}{\omega_c} + \frac{s^2}{\omega_c}} \tag{2.16}$$

Where ω_c is the cut-off frequency of the measurement filter. Although in average value mode PWM converters are simply replaced with voltage sources, these measurement filters are kept due to the introduced delay and phase shift in control system.

2.1.2.2 abc to dq conversion

The goal of abc to dq axis conversion is to convert rotating AC signals into DC signals which is easier for control system design. Moreover, by applying abc to dq conversion with specific d axis alignments, real and reactive power can be completely decoupled, therefore controlled independently with different control loops.

The dq transformation is defined as:

$$\begin{bmatrix} v_d \\ v_q \\ v_0 \end{bmatrix} = T_{dq} \begin{bmatrix} v_a \\ v_b \\ v_c \end{bmatrix} \tag{2.17}$$

Where v_a, v_b, v_c, are instantaneous phase voltage, and v_d, v_q, v_0, are transformed voltage signals in dq axis. T_{dq} is the transformation matrix and is defined as:

$$T_{dq} = \frac{2}{3} \begin{bmatrix} \cos\theta & \cos(\theta - \frac{2\pi}{3}) & \cos(\theta + \frac{2\pi}{3}) \\ -\sin\theta & -\sin(\theta - \frac{2\pi}{3}) & -\sin(\theta + \frac{2\pi}{3}) \\ \frac{1}{2} & \frac{1}{2} & \frac{1}{2} \end{bmatrix} \tag{2.18}$$

Where θ is phase angle and is measured by PLL. In GSC, the phase angle is controlled by a PI controller that aligns d axis to stator voltage, i.e., v_q=0. In MSC, different orientations can be used, which aligns d axis to rotor flux or stator voltage.

The controller output is then transformed into abc axis and feeds into PWM converters:

$$\begin{bmatrix} v_a \\ v_b \\ v_c \end{bmatrix} = T'_{dq} \begin{bmatrix} v_d \\ v_q \\ v_0 \end{bmatrix} \tag{2.19}$$

Where T'_{dq} is the inverse transformation matrix and is defined as:

$$T'_{dq} = \begin{bmatrix} \cos\theta & -\sin\theta & 1 \\ \cos(\theta - \frac{2\pi}{3}) & -\sin(\theta - \frac{2\pi}{3}) & 1 \\ \cos(\theta + \frac{2\pi}{3}) & -\sin(\theta + \frac{2\pi}{3}) & 1 \end{bmatrix} \tag{2.20}$$

2.1.2.3 PLL

A conventional synchronous reference frame PLL (SRF-PLL) design is shown in Fig. 2.8.

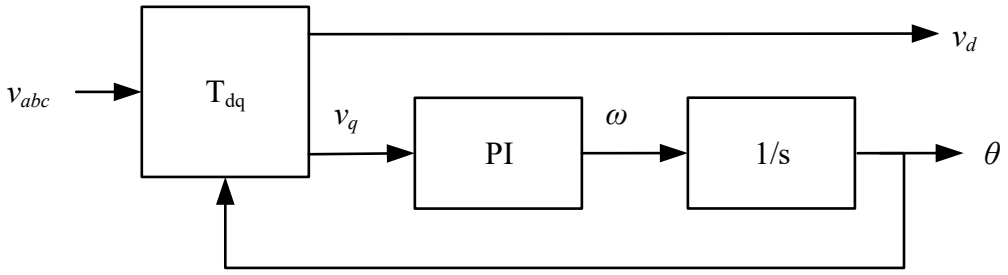

Fig. 2.8 SRF-PLL diagram

Three phase signal v_{abc} is converted to dq reference frame using the park transformation matrix T_{dq}. PI controller is used to control the phase angle so that q axis voltage output is 0. Therefore, in steady state, the voltage amplitude output equals its d axis component.

Under balanced conditions, SRF-PLL has good reliability and accuracy. However, under the presence of high frequency harmonics and unbalanced voltages, PLL's dynamic behavior becomes very unstable and its performance deteriorates. Therefore, double synchronous reference frame PLL (DSRF-PLL) is used for wind park models.

A three-phase unbalanced voltage signal can be expressed as:

$$\begin{bmatrix} v_a \\ v_b \\ v_c \end{bmatrix} = \begin{bmatrix} V_a^p \cos(\omega t) \\ V_b^p \cos(\omega t - \frac{2\pi}{3}) \\ V_c^p \cos(\omega t + \frac{2\pi}{3}) \end{bmatrix} + \begin{bmatrix} V_a^n \cos(\omega t + \phi^n) \\ V_b^n \cos(\omega t + \frac{2\pi}{3} + \phi^n) \\ V_c^n \cos(\omega t - \frac{2\pi}{3} + \phi^n) \end{bmatrix} + \begin{bmatrix} V_a^0 \cos(\omega t + \phi^0) \\ V_b^0 \cos(\omega t + \phi^0) \\ V_c^0 \cos(\omega t + \phi^0) \end{bmatrix} \quad (2.21)$$

Where V^p, V^n, V^o are magnitudes of positive, negative and zero sequence voltage magnitudes. ϕ^n and ϕ^o are negative and zero sequence angles. Subscript a, b and c denotes phase A, B and C components respectively. Clark transformation is defined as:

$$\begin{bmatrix} v_\alpha \\ v_\beta \\ v_0 \end{bmatrix} = T_{\alpha\beta} \begin{bmatrix} v_a \\ v_b \\ v_c \end{bmatrix} \quad (2.22)$$

Where $T_{\alpha\beta}$ is the Clark transformation matrix:

$$T_{\alpha\beta} = \frac{2}{3} \begin{bmatrix} 1 & -\frac{1}{2} & -\frac{1}{2} \\ 0 & \frac{\sqrt{3}}{2} & -\frac{\sqrt{3}}{2} \\ \frac{1}{2} & \frac{1}{2} & \frac{1}{2} \end{bmatrix} \quad (2.23)$$

Apply Clark transformation to this unbalanced voltage signal, ignore zero sequence component:

$$\begin{bmatrix} v_\alpha \\ v_\beta \end{bmatrix} = \begin{bmatrix} V_\alpha^p \cos \omega t \\ V_\beta^p \sin \omega t \end{bmatrix} + \begin{bmatrix} V_\alpha^n \cos(-\omega t + \phi^n) \\ V_\beta^n \sin(-\omega t + \phi^n) \end{bmatrix} \quad (2.24)$$

Which shows the signal consists of two rotating vectors, a positive sequence $\begin{bmatrix} V_\alpha^p \cos \omega t \\ V_\beta^p \sin \omega t \end{bmatrix}$ rotating at frequency ω, and a negative sequence component $\begin{bmatrix} V_\alpha^n \cos(-\omega t + \phi^n) \\ V_\beta^n \sin(-\omega t + \phi^n) \end{bmatrix}$ rotating at frequency $-\omega$.

The above signal in alpha-beta reference frame can be expressed as:

$$\begin{bmatrix} v_\alpha \\ v_\beta \end{bmatrix} = \mathbf{v}_{\alpha\beta}^n + \mathbf{v}_{\alpha\beta}^m = V^n \begin{bmatrix} \cos(n\omega t + \phi^n) \\ \sin(n\omega t + \phi^n) \end{bmatrix} + V^m \begin{bmatrix} \cos(m\omega t + \phi^m) \\ \sin(m\omega t + \phi^m) \end{bmatrix} \quad (2.25)$$

Where n and m can be either positive or negative. By applying dq transformation to this signal, two sets of signals in dq reference frame can be obtained, depending on polarity of n and m:

$$\begin{bmatrix} v_d^n \\ v_q^n \end{bmatrix} = V^n \begin{bmatrix} \cos\phi^n \\ \sin\phi^n \end{bmatrix} + V^m \cos\phi^m \begin{bmatrix} \cos((n-m)\omega t) \\ -\sin((n-m)\omega t) \end{bmatrix} + V^m \sin\phi^m \begin{bmatrix} \sin((n-m)\omega t) \\ \cos((n-m)\omega t) \end{bmatrix} \quad (2.26)$$

$$\begin{bmatrix} v_d^m \\ v_q^m \end{bmatrix} = V^m \begin{bmatrix} \cos\phi^m \\ \sin\phi^m \end{bmatrix} + V^n \cos\phi^n \begin{bmatrix} \cos((n-m)\omega t) \\ \sin((n-m)\omega t) \end{bmatrix} + V^n \sin\phi^n \begin{bmatrix} -\sin((n-m)\omega t) \\ \cos((n-m)\omega t) \end{bmatrix} \quad (2.27)$$

The following diagram shows the decoupling function which is used to remove double frequency components from positive and negative sequence components:

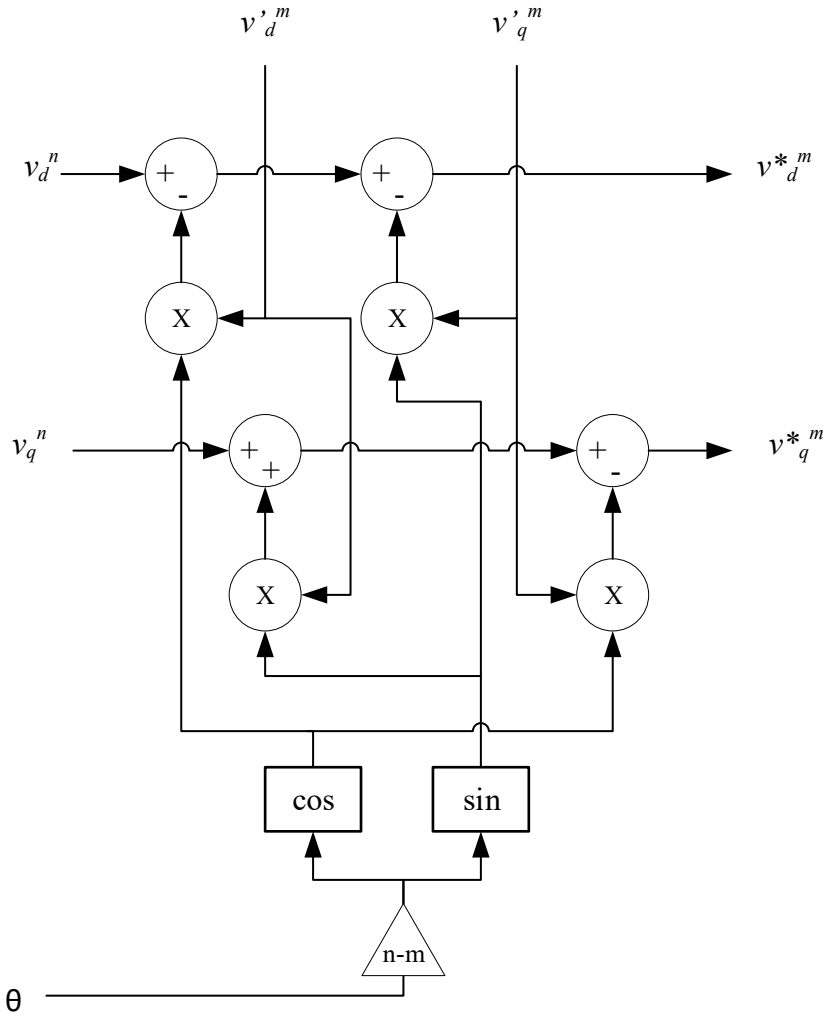

Fig. 2.9 Decoupling function diagram

With this decoupling function, the DSRF-PLL can be designed as shown in Fig. 2.10:

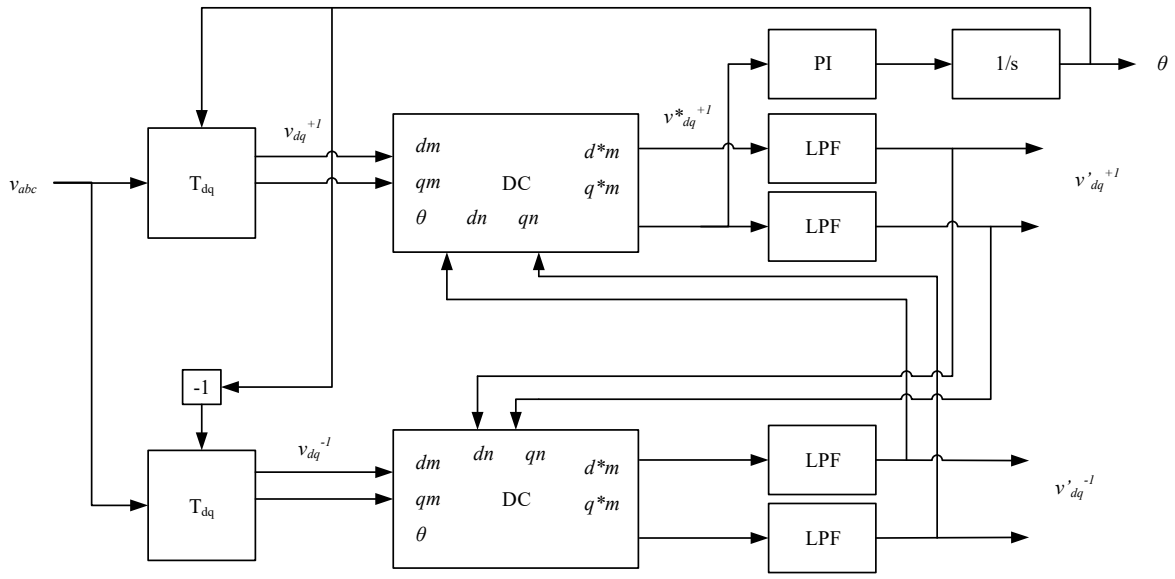

Fig. 2.10 DSRF PLL diagram

With the decoupling function, all double frequency oscillation terms are removed from the output positive sequence and negative sequence dq signals v'^{+1}_{dq} and v'^{-1}_{dq}. The performance of this DSRF-PLL design has already been verified in many studies, especially in unbalanced conditions.

2.1.2.4 MSC controller

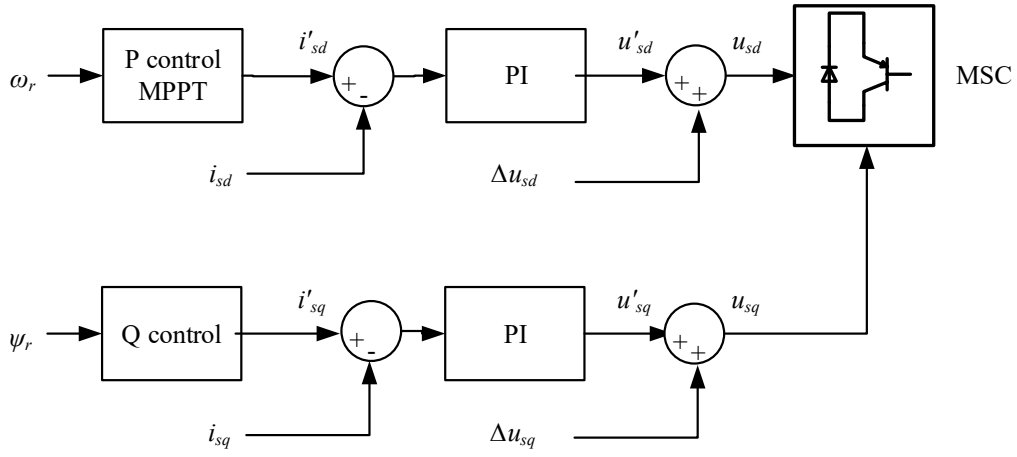

Fig. 2.11 MSC controller diagram

The MSC part of the controller is shown in Fig. 2.11. In some models, MSC controller uses rotor flux orientation, i.e. the d-axis of the rotating reference frame is controlled to align with rotor flux

direction. The q-axis component of rotor flux is zero, i.e. ψ_{rq}=0, therefore ψ_{rd}=|ψ_r|. In this rotor flux orientation, stator voltage is given by:

$$\begin{aligned} u_{sd} &= R_s i_{sd} + \sigma L_s \frac{\mathrm{d}i_{sd}}{\mathrm{d}t} + \frac{L_m}{L_r}\frac{\mathrm{d}\psi_{rd}}{\mathrm{d}t} - \omega_0 \sigma L_s i_{sq} \\ u_{sq} &= R_s i_{sq} + \sigma L_s \frac{\mathrm{d}i_{sq}}{\mathrm{d}t} + \omega_0(\sigma L_s i_{sd} + \psi_{rd}\frac{L_m}{L_r}) \end{aligned} \tag{2.28}$$

Where u_{sd}, u_{sq} are stator voltage in d and q axis, L_s, L_m, L_r are stator, mutual and rotor inductance respectively. ψ_{rd} is d axis rotor flux, i_{sd}, i_{sq} are stator current in d and q axis. σ is leakage coefficient and is defined as:

$$\sigma = 1 - \frac{L_m^2}{L_s L_r} \tag{2.29}$$

The rotor flux is calculated by:

$$\psi_{rd} = \frac{L_m}{1+\tau_r p} i_{sd} \tag{2.30}$$

Since q axis flux is 0, the electromagnetic torque is calculated as:

$$T_e = n_p \frac{L_m}{L_r} \psi_{sd} i_{sq} \tag{2.31}$$

Therefore, in rotor flux orientation, the electromagnetic torque is only related to q axis stator current i_{sq}, and rotor flux is only related to d axis stator current i_{sd}. By controlling i_{sd} and i_{sq} independently, decoupled control of generator's active and reactive power can be achieved.

In the developed model, stator voltage orientation is used to avoid confusion and simplify signal conversion between different orientations. By aligning d axis to the stator voltage vector direction, u_{sd}=u_s, u_{sq}=0. For PMSGs, rotor is usually assumed symmetrical, therefore L_d=L_q=L. The voltage of a PMSG is calculated as:

$$\begin{aligned} u_{sd} &= r_s i_{sd} + \frac{\mathrm{d}\psi_d}{\mathrm{d}t} - \omega_e \psi_q = u_s \\ u_{sq} &= r_s i_{sd} + \frac{\mathrm{d}\psi_q}{\mathrm{d}t} + \omega_e \psi_d = 0 \end{aligned} \tag{2.32}$$

Where ψ_d and ψ_q are d and q axis flux, and are calculated as:

$$\begin{aligned} \psi_{sd} &= Li_{sd} + \psi_{pm} \\ \psi_{sq} &= Li_{sq} \end{aligned} \tag{2.33}$$

Substituting (2.33) into (2.32),

$$\begin{aligned} u_{sd} &= r_s i_{sd} + L\frac{\mathrm{d}i_{sd}}{\mathrm{d}t} - \omega_e L i_{sq} \\ u_{sq} &= r_s i_{sd} + L\frac{\mathrm{d}i_{sq}}{\mathrm{d}t} + \omega_e (L i_{sd} + \psi_{pm}) \end{aligned} \tag{2.34}$$

The real and reactive power output of PMSG is:

$$\begin{aligned} P &= \frac{3}{2} u_s i_{sd} \\ Q &= \frac{3}{2} u_s i_{sq} \end{aligned} \tag{2.35}$$

Which also shows that real and reactive power are completely decoupled in stator flux orientation. By controlling corresponding voltage and current vectors, real and reactive power output of the generator can be controlled independently.

- Maximum power point tracking (MPPT) control

To achieve maximum power extraction, an MPPT controller is used to calculate desired reference power using rotor's rotation speed. The desired power output is calculated as:

$$P_{ref} = \omega_r^2 K_{optimal} \tag{2.36}$$

Where P_{ref} is calculated reference power output, ω_r is rotor speed and $K_{optimal}$ is a scaling factor. The calculated reference power is then passed to inner current control loop.

- Q control

Different control strategies can be used to control the q axis current of MSC. For simplicity, unity power factor control is used in this model. With this control strategy, reactive power output of generator is controlled to be 0, which reduced the required rating of MSC. Since q axis current is always set to 0, generator output voltage will change with rotor speed, therefore overvoltage and overspeed may occur. Since in Type-IV WTG generator is completely decoupled from the grid, using this control strategy has no impact on GSC dynamics.

- Inner control loop

Inner control loop controls MSC voltage based on reference current calculated by outer control loops using PI controllers. Take equation (2.34) and define its output as reference voltage signals for PWM converter:

$$\begin{aligned} u_{sd}^{'} &= r_s i_{sd} + L\frac{\mathrm{d}\, i_{sd}}{dt} - \omega_e L i_{sq} \\ u_{sq}^{'} &= r_s i_{sd} + L\frac{\mathrm{d}\, i_{sq}}{dt} + \omega_e (L i_{sd} + \psi_{pm}) \end{aligned} \tag{2.37}$$

Replace derivative terms with PI controllers, the inner control loop can be represented with equation:

$$\begin{aligned} u_{sd}^{'} &= r_s i_{sd} + K_{p,inner}\left(i_{sd}^{'} - i_{sd}\right) + K_{i,inner}\int\left(i_{sd}^{'} - i_{sd}\right)\mathrm{d}\, t - \omega_e L i_{sq} \\ u_{sq}^{'} &= r_s i_{sd} + K_{p,inner}\left(i_{sq}^{'} - i_{sq}\right) + K_{i,inner}\int\left(i_{sq}^{'} - i_{sq}\right)\mathrm{d}\, t + \omega_e (L i_{sd} + \psi_{pm}) \end{aligned} \tag{2.38}$$

Where $K_{p,inner}$ and $K_{i,inner}$ are inner control loop PI controller's parameters. $-\omega_e L i_{sq}$ and $\omega_e (L i_{sd} + \psi_{pm})$ are feedforward terms and are calculated and added back to PI controller output.

2.1.2.5 GSC controller

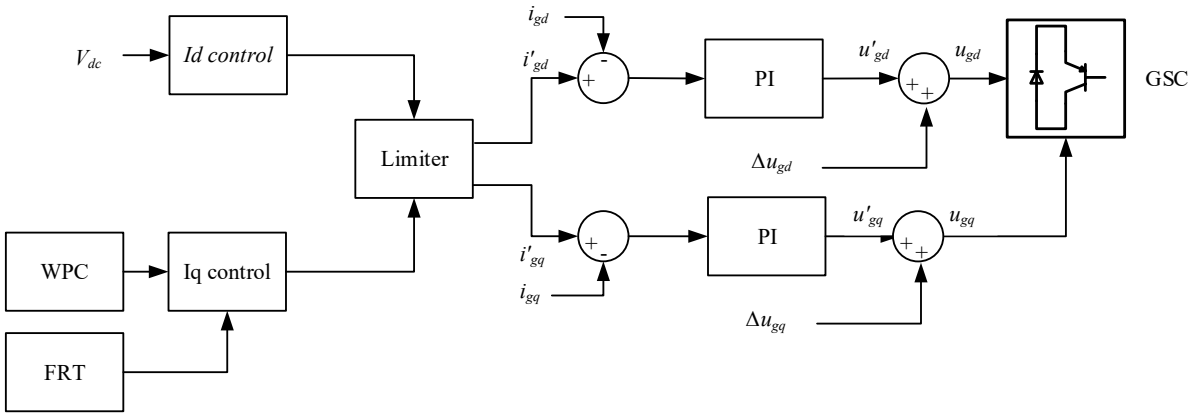

Fig. 2.12 GSC controller diagram

The GSC part of the controller is shown in Fig. 2.12. Consider the choke equation given in (2.14):

$$\mathbf{v}_{lv} = R\mathbf{i}_g + L\frac{\mathrm{d}\,\mathbf{i}_g}{\mathrm{d}\, t} + \mathbf{v}_{gsc} \tag{2.39}$$

Apply dq transformation:

$$\begin{aligned} v_{lv,d} &= Ri_{gd} + L\frac{\mathrm{d}i_{gd}}{\mathrm{d}t} - \omega_0 Li_{gq} + v_{gsc,d} \\ v_{lv,q} &= Ri_{gq} + L\frac{\mathrm{d}i_{gq}}{\mathrm{d}t} + \omega_0 Li_{gd} + v_{gsc,q} \end{aligned} \tag{2.40}$$

Where subscript d and q denotes components in dq axis. In GSC, grid voltage orientation is used, i.e. d axis is aligned with grid voltage and q axis component is controlled to be 0 by PLL. With this orientation, power equations in (2.35) can be simplified into:

$$\begin{aligned} P &= \frac{3}{2}u_{gd}i_{gd} \\ Q &= -\frac{3}{2}u_{gd}i_{gq} \end{aligned} \tag{2.41}$$

Apparently, real power output of GSC can be controlled with d axis current i_{gd} and reactive power output of GSC can be controlled with q axis current i_{gq}.

- DC voltage control

As shown in equation (2.12), power transferred by GSC is:

$$P_{gsc} = \sqrt{3}u_{gd}i_{gd} = U_{dc}I_g \tag{2.42}$$

Where u_{gd} and i_{gd} are d axis voltage and current of GSC controller on AC side. The DC bus voltage is given as:

$$C\frac{\mathrm{d}U_{dc}}{\mathrm{d}t} = \frac{3}{2\sqrt{2}}p_{md}i_{gd} - I_v \tag{2.43}$$

Where C is DC capacitor voltage, I_v is DC current flowing into GSC, and p_{md} is d axis modulation factor, which is calculated by:

$$\begin{aligned} p_{md} &= \frac{2\sqrt{2}}{\sqrt{3}}\frac{u_{gd}}{U_{dc}} \\ p_{mq} &= \frac{2\sqrt{2}}{\sqrt{3}}\frac{u_{gq}}{U_{dc}} \end{aligned} \tag{2.44}$$

Applying laplace transform to (2.43):

$$U_{dc}(s) = \frac{3p_{md}}{2\sqrt{2}Cs}i_{gd}(s) \tag{2.45}$$

Which shows that DC bus voltage is controlled by the d axis current output of GSC. A PI controller is used to control DC bus voltage at 1 pu by regulating d axis current reference:

$$i_{gd}^{*} = K_p\left(U_{DC}^{'} - U_{DC}\right) + K_i\int\left(U_{DC}^{'} - U_{DC}\right)\mathrm{d}t \tag{2.46}$$

Where K_p and K_i are PI controller parameters, $U_{DC}^{'}$ is reference DC voltage and U_{DC} is measured DC bus voltage.

- Wind park controller (WPC)

In an actual wind park consisting of many individual WTGs, all WTGs are connected to the collector grid and then connected to the external grid via wind park transformer.

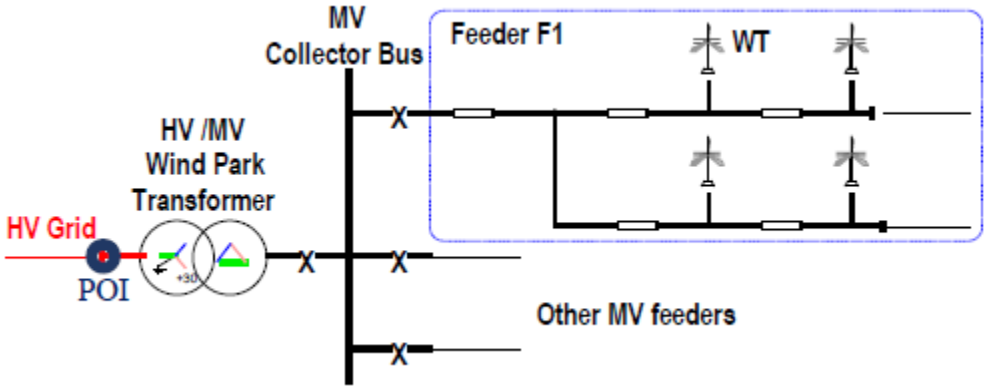

Fig. 2.13 POI configuration

The point of connection (POI) is defined as the HV side of the wind park transformer. All individual WTGs have their own real power output control, but according to grid code requirements, a central reactive power control is required at POI. WPC can operate in different modes to control different parameters, such as voltage magnitude at POI (V control), reactive power injection at POI (Q control) and power factor of the whole wind park (pf control). The diagram of WPC is shown in Fig. 2.14:

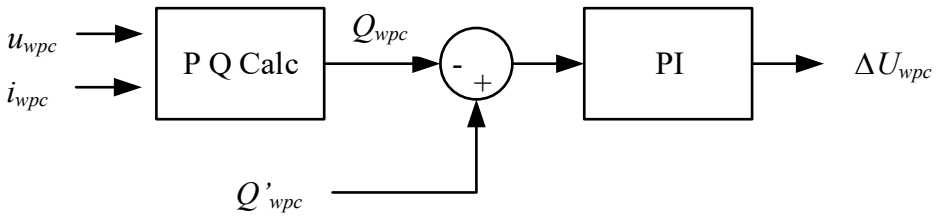

Fig. 2.14 WPC controller

In this model, Q control is used and reactive power output of WPC is set to 0. ΔU_{wpc} is the output signal of WPC and will be added to the q axis current reference.

- Q axis current control

The output of WPC is fed into q axis current controller and added to the reference current directly. In addition, the controller also monitors LV bus voltage magnitude v_{lv} and adds it to reference. The sum is then controlled by a proportional gain $K_{pq,gsc}$. The equation for reference q axis current is:

$$i^*_{gq} = K_{pq,gsc}(1 + \Delta U_{wpc} - v_{lv}) \tag{2.47}$$

- Fault ride through (FRT)

With the increasing capacity of wind parks, many grid codes require wind parks to stay connected during faults and must inject dynamic reactive power to supply grid voltage. Low voltage ride through (LVRT) requires wind park to maintain operating uninterrupted during a voltage dip. Similarly, high voltage ride through (HVRT) requires wind park to maintain operating in case of an overvoltage that might occur after fault clearance. Type IV WTGs have already been studied and shown to have good FRT performance.

FRT signal is raised when LV bus voltage deviation from 1 pu is greater than 0.125 pu. FRT signal will be reset after a minimum time delay and when LV bus voltage deviation recovers below 0.1 pu. During FRT operation, WPC's control signal ΔU_{wpc} is ignored and q axis current is controlled to bring LV bus voltage v_{lv} to 1 p:

$$i^*_{gq} = K_{pq,FRT}(1 - v_{lv}) \tag{2.48}$$

Where $K_{pq,gsc}$ is a proportional gain used during FRT. The relationship between reference current i^*_{gq} and LV bus voltage v_{lv} is shown in Fig. 2.15.

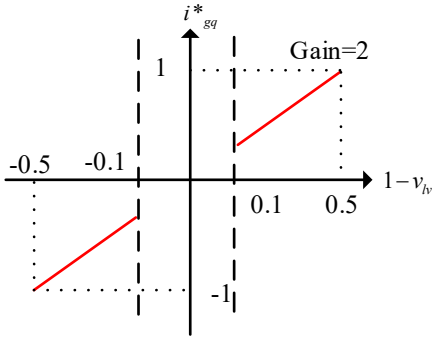

Fig. 2.15 Current output during FRT

- Current limiter

During transients, reference current signals calculated by DC voltage control and Q axis current control can cause overcurrent of GSC, therefore current signals need to be limited. During normal operation, priority is given to d axis current and it is limited by the maximum d axis current limit I_{gd}^{lim}:

$$i'_{gd} = \min(i^*_{gd}, I_{gd}^{\lim}) \tag{2.49}$$

The q axis current limit is then set to remaining capacity of GSC or maximum q axis current limit, whichever is smaller:

$$i_{gq}^{\max} = \min\left(\sqrt{\left(I_{gsc}^{\lim}\right)^2 - \left(i'_{gd}\right)^2}, I_{gq}^{\lim}\right) \tag{2.50}$$

Finally, q axis current is limited by the calculated maximum limit:

$$i'_{gq} = \min\left(\left|i^*_{gq}\right|, i_{gq}^{\max}\right)\operatorname{sign}\left(i^*_{gq}\right) \tag{2.51}$$

Since q axis reference current i^*_{gq} can be either positive or negative, a sign function is used to return either +1 or -1 to set direction to the limited current.

During FRT, priority is given to q axis current and it is limited by maximum q axis current limit first:

$$i'_{gq} = \min(i^*_{gq}, I_{gq}^{\lim}) \tag{2.52}$$

The d axis current limit is then set to remaining capacity of GSC or maximum d axis current limit, whichever is smaller:

$$i_{gd}^{\max} = \min\left(\sqrt{\left(I_{gsc}^{\lim}\right)^2 - \left(i'_{gq}\right)^2}, I_{gd}^{\lim}\right) \tag{2.53}$$

Finally, d axis current is limited by the calculated maximum limit:

$$i'_{gd} = \min\left(\left|i^*_{gd}\right|, i_{gd}^{\max}\right)\operatorname{sign}\left(i^*_{gd}\right) \tag{2.54}$$

The relationship between an unlimited input current i and the output of the limiter i'_Q and i'_P when operating in FRT and normal mode can be plotted in Fig. 2.16:

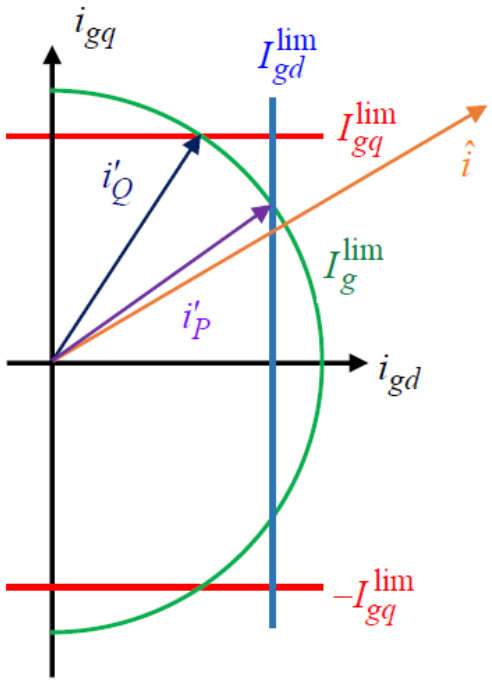

Fig. 2.16 Current limiter output vs input

- Inner control loop

Inner control loop of GSC is used to calculate GSC voltages with reference current signals. Consider the choke filter's voltage equation given in (2.14):

$$v_{lv} = Ri_g + L\frac{\mathrm{d}i_g}{\mathrm{d}t} + v_{gsc} \tag{2.55}$$

Apply dq transformation to it:

$$
\begin{aligned}
v_{cd} &= -Ri_{gd} - L\frac{\mathrm{d}i_{gd}}{\mathrm{d}t} + \omega_s L i_{gq} + v_{gd} \\
v_{cq} &= -Ri_{gq} - L\frac{\mathrm{d}i_{gq}}{\mathrm{d}t} - \omega_s L i_{gd} + v_{gq}
\end{aligned}
\tag{2.56}
$$

Where v_{cd} and v_{cq} are converter voltage in d and q axis, ω_s is grid frequency, v_{gd} and v_{gq} are LV bus voltage in d and q axis.

Replacing derivative terms with PI controllers:

$$
\begin{aligned}
v'_{cd} &= -Ri_{gd} - \left[K_p\left(i'_{gd} - i_{gd}\right) + K_i\int\left(i'_{gd} - i_{gd}\right)\mathrm{d}t\right] + \omega_s L i_{gq} + v_{gd} \\
v'_{cq} &= -Ri_{gq} - \left[K_p\left(i'_{gq} - i_{gq}\right) + K_i\int\left(i'_{gq} - i_{gq}\right)\mathrm{d}t\right] - \omega_s L i_{gd} + v_{gq}
\end{aligned}
\tag{2.57}
$$

Where K_p and K_i are PI controller parameters. Since choke resistance is usually very small and can be neglected, above equations can be further simplified into:

$$
\begin{aligned}
v'_{cd} &= -\left[K_p\left(i'_{gd} - i_{gd}\right) + K_i\int\left(i'_{gd} - i_{gd}\right)\mathrm{d}t\right] + \omega_s L i_{gq} + v_{gd} \\
v'_{cq} &= -\left[K_p\left(i'_{gq} - i_{gq}\right) + K_i\int\left(i'_{gq} - i_{gq}\right)\mathrm{d}t\right] - \omega_s L i_{gd} + v_{gq}
\end{aligned}
\tag{2.58}
$$

Feedforward terms $\omega_s L i_{gq} + v_{gd}$ and $-\omega_s L i_{gd} + v_{gq}$ are added to d and q axis respectively to make PI controller's output close to 0 in steady state. Output voltage signals are limited to 1 pu. to prevent overvoltage of GSC controller, then passed to the PWM converter.

2.2 Type III doubly fed induction generator (DFIG) WP model

Type III WP uses DFIG to generate power. Doubly fed means that the stator is directly connected to the grid, while rotor winding is also connected to the grid through PWM converters. Therefore, power flows on both stator and rotor windings. Since the stator winding is connected to the grid directly, operation speed of the generator is limited but still variable, since PWM converters can compensate for the speed difference between rotor's mechanical speed and stator's electrical speed by controlling rotor winding current's frequency. During normal operation, only 30% of rated power is transferred through PWM converters, therefore the required PWM converter capacity for Type III WTG is lower than a Type IV WTG of same capacity. Typical Type III WTG consists of wind turbine, DFIG and PWM converters. As shown in Fig. 2.17, the stator winding is connected directly to the grid, while rotor winding is connected to grid through two PWM converters, rotor side converter (RSC) and GSC.

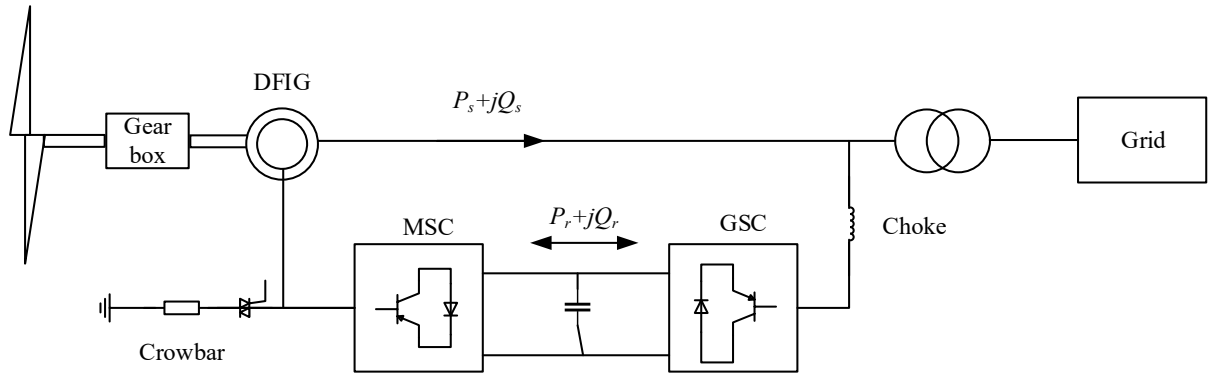

Fig. 2.17 Type III WP diagram

2.2.1 Components of Type III WTG

The mechanical model and wind turbine model are the same as type IV WTG, therefore omitted here.

2.2.1.1 Choke filter

The same choke filter is used for DFIG as in Type IV WTG. Similar to Type IV WTG model, following equation can be obtained:

$$\mathbf{v}_{lv} = R\mathbf{i}_g + L\frac{\mathrm{d}\,\mathbf{i}_g}{\mathrm{d}\,t} + \mathbf{v}_{gsc} \tag{2.59}$$

Applying dq transformation with grid voltage orientation:

$$\begin{aligned} v_{lv,d} &= Ri_{gd} + L\frac{\mathrm{d}i_{gd}}{\mathrm{d}t} - \omega_0 Li_{gq} + v_{gsc,d} \\ v_{lv,q} &= Ri_{gq} + L\frac{\mathrm{d}i_{gq}}{\mathrm{d}t} + \omega_0 Li_{gd} + v_{gsc,q} \end{aligned} \tag{2.60}$$

The power equations can be obtained as:

$$\begin{aligned} P &= \frac{3}{2}u_{gd}i_{gd} \\ Q &= -\frac{3}{2}u_{gd}i_{gq} \end{aligned} \tag{2.61}$$

Similar to Type IV WTG, active power and reactive power can be controlled separately using d and q axis currents.

2.2.1.2 DFIG model

The equivalent circuit of a DFIG is shown in Fig. 2.18.

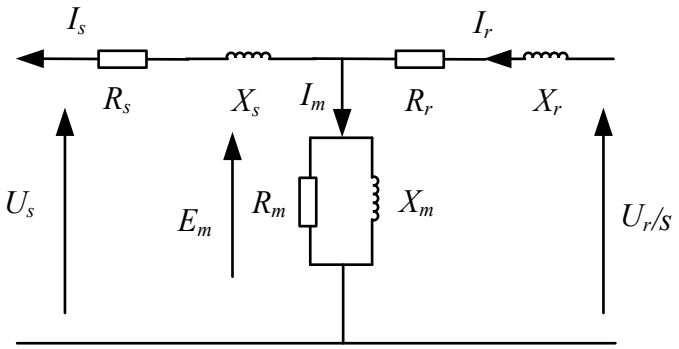

Fig. 2.18 DFIG Equivalent Circuit

Where U_s, U_r and E_m are stator, rotor and magnetizing voltages, I_s, I_r and I_m are stator, rotor and magnetizing currents. X_s, X_r, X_m, R_s, R_r and R_m are stator, rotor and magnetizing reactance and resistance, respectively.

Slip s is defined as:

$$s = \frac{\omega_s - n\omega_m}{\omega_s} = \frac{\omega_r}{\omega_s} \tag{2.62}$$

Where ω_s is the angular speed of stator flux, n is pole pair number and ω_m is mechanical speed of rotor. ω_r is the angular speed of rotor flux.

The voltage equation of a DFIG can be written as:

$$\begin{aligned} \mathbf{U}_s &= \mathbf{E}_m - R_s\mathbf{I}_s - X_s\mathbf{I}_s \\ \frac{\mathbf{U}_r}{s} &= \mathbf{E}_m + R_r\mathbf{I}_r - X_r\mathbf{I}_r \end{aligned} \tag{2.63}$$

Ignoring magnetizing losses, the electromagnetic power received by the stator is:

$$P_{em} = \mathrm{Re}(\mathbf{E}_m\mathbf{I}_m^*) = \mathrm{Re}(\mathbf{X}_m\mathbf{I}_m\mathbf{I}_s^*) \tag{2.64}$$

Stator's output power is:

$$P_s = \mathrm{Re}(\mathbf{U}_s\mathbf{I}_s^*) = \mathrm{Re}(\mathbf{E}_m\mathbf{I}_s^*) - R_sI_s^2 = P_{em} - P_{cus} \tag{2.65}$$

Where P_{cus} is defined as the copper loss on stator winding.

Similarly, rotor's input power is defined as:

$$P_r = \mathrm{Re}(\mathbf{U}_r\mathbf{I}_r^*) = \mathrm{Re}(s\mathbf{E}_m\mathbf{I}_r^*) + R_rI_r^2 = P_{cur} + sP_{em} \tag{2.66}$$

Mechanical power input is defined as:

$$P_m = (1-s)P_{em} \tag{2.67}$$

Where P_{cur} is defined as the copper loss on rotor winding.

The power flow of a DFIG can be expressed with the following diagram:

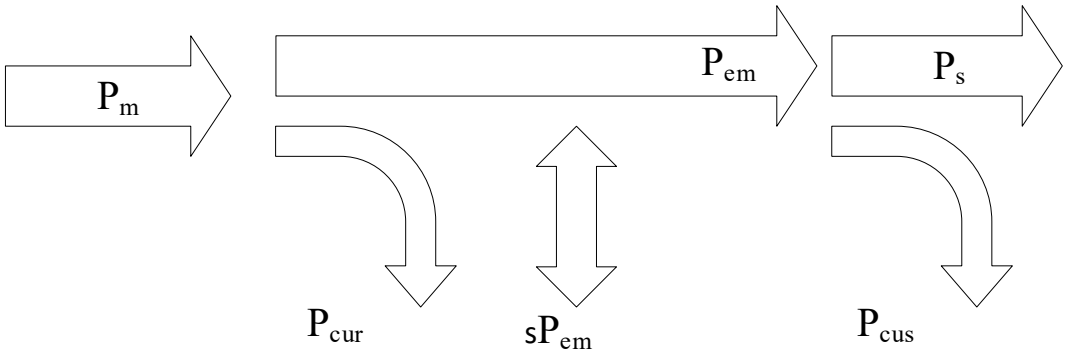

Fig. 2.19 DFIG power flow

As illustrated in the diagram, power flow on rotor winding is bi-directional. When DFIG is operating in sub-synchronous mode, i.e. s>0, power is fed into the rotor winding through PWM

converters. When DFIG is operating in super-synchronous mode, i.e. s<0, power is extracted from rotor winding and fed into the grid through PWM converters.

Neglecting all losses, the power flow of a DFIG can be simplified into:

$$P_s \approx \frac{P_m}{1-s}$$
$$P_r \approx \frac{-sP_m}{1-s} = -sP_s \tag{2.68}$$

Which shows that the power flow through the converter, i.e. P_s, is related to the slip and is much smaller than the power flow of stator winding of DFIG.

Similar to PMSG, a controller can be designed to decouple and control DFIG's active and reactive power output. Unlike Type IV WTG, the converter rating required is only a fraction of the DFIG's rating, and is only related to the slip of DFIG, a.k.a. operating speed range, therefore reducing the cost of construction.

2.2.2 Control system for DFIG

The control system for Type IV WTG is shown in the following diagram:

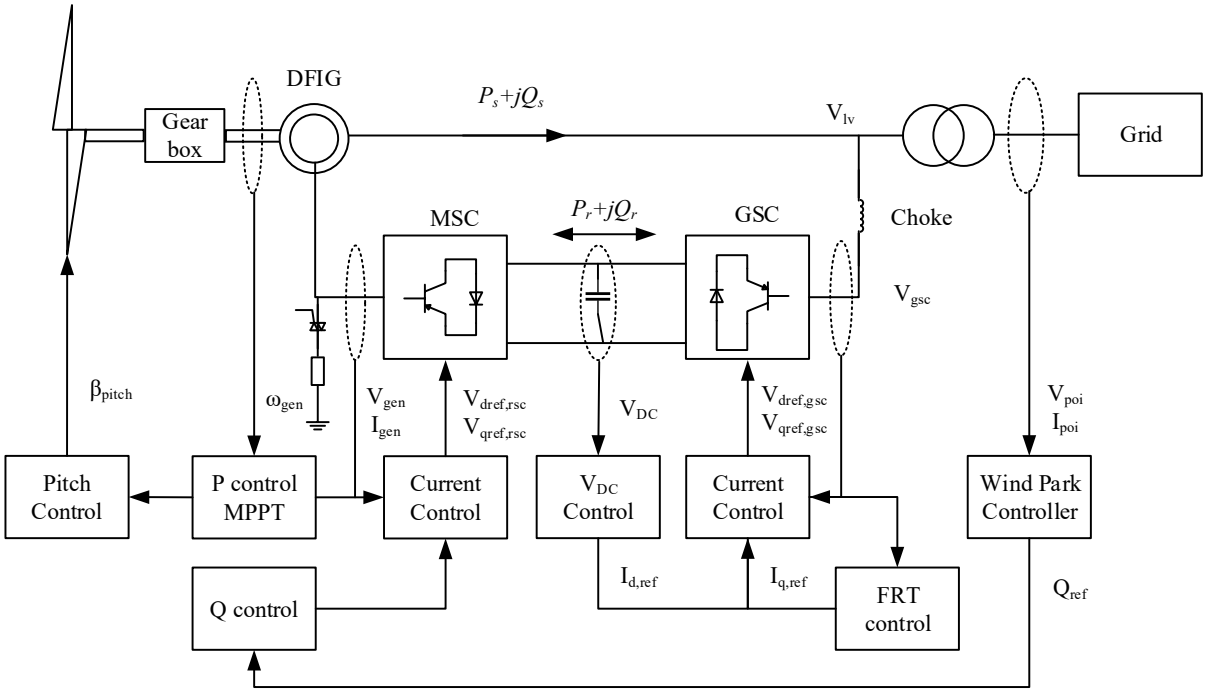

Fig. 2.20 DFIG controller

Since DFIG is used in Type IV WTG, the behavior of DFIG is determined by both the GSC and RSC. Different from Type III WTG, power flow on DC bus is bi-directional, and the direction of power flow is determined by rotor speed. The goals of GSC controller are:

- Control DC bus voltage;
- Control reactive power injection during FRT.

The MSC is connected to rotor winding through slip rings. The goals of MSC controller are:

- Maximize power extraction at given generator speed;
- Control reactive power generation.

A pitch controller is also included to prevent overspeed by controlling wind turbine's pitch angle.

2.2.2.1 abc to dq transformation

Similar to Type IV WTG, Clark transformation is used to transform measured AC signals into DC signals which are easier to calculate and control. Moreover, decoupled d and q axis components allow controlling of active and reactive power and current separately. The same dq transformation as Type IV WTG is used, therefore omitted here. However, the orientation can be different based on the controller design, which will be discussed in following parts.

2.2.2.2 RSC Controller

The block diagram of RSC controller is shown in Fig. 2.21:

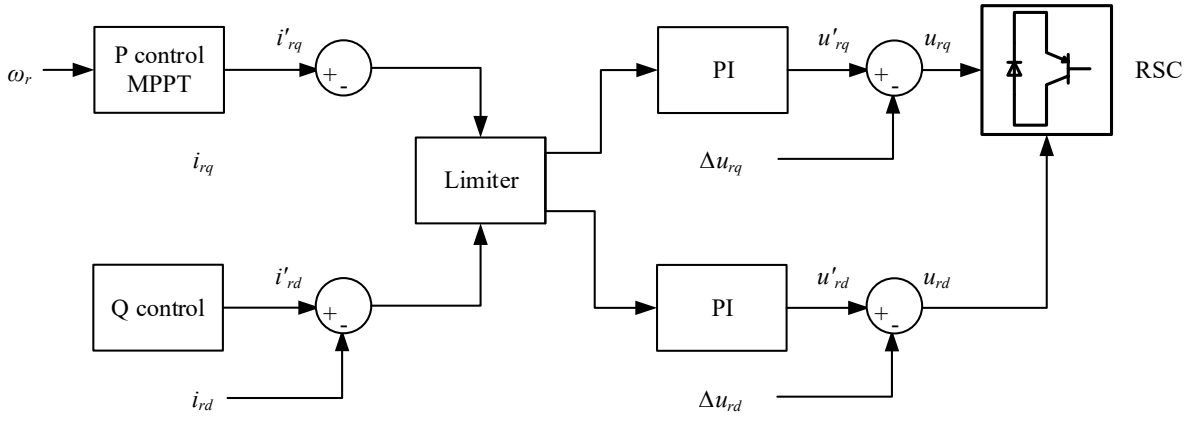

Fig. 2.21 RSC controller

To simplify calculation, following assumptions are used on the DFIG:

- Rotor is assumed to be in perfect symmetrical shape, and magnetic potential distribution in airgap is in sinusoidal shape;
- Magnetizing loss and saturation effect of the core are ignored.

Similar to PMSG, apply dq transformation to voltage and flux equations for DFIG, voltage in dq axis can be expressed as:

$$\begin{aligned} u_{sd} &= -R_s i_{sd} + \frac{\mathrm{d}\psi_{sd}}{\mathrm{d}t} - \psi_{sq}\omega_s \\ u_{sq} &= -R_s i_{sq} + \frac{\mathrm{d}\psi_{sq}}{\mathrm{d}t} + \psi_{sd}\omega_s \\ u_{rd} &= R_r i_{rd} + \frac{\mathrm{d}\psi_{rd}}{\mathrm{d}t} - \psi_{rq}\omega_r \\ u_{rq} &= R_r i_{rq} + \frac{\mathrm{d}\psi_{rq}}{\mathrm{d}t} + \psi_{rd}\omega_r \end{aligned} \tag{2.69}$$

Flux can be represented as:

$$\begin{aligned} \psi_{sd} &= -L_s i_{sd} + L_m i_{rd} \\ \psi_{sq} &= -L_s i_{sq} + L_m i_{rq} \\ \psi_{rd} &= L_r i_{rd} + L_m i_{rd} \\ \psi_{rq} &= L_r i_{rq} + L_m i_{rq} \end{aligned} \tag{2.70}$$

Where *u, i, ψ, ω, L* and *R* represents voltage, current, flux, angular speed of flux, inductance and resistance. Subscript s, r and d, q represents stator and rotor, d and q axis components, respectively.

For RSC, the stator flux reference frame (SFR) is used, which means the d axis is aligned with stator flux. The same transformation matrix T_{dq} as Type IV WTG is used for Clark transformation:

$$T_{dq} = \frac{2}{3}\begin{bmatrix} \cos\theta & \cos(\theta - \frac{2\pi}{3}) & \cos(\theta + \frac{2\pi}{3}) \\ -\sin\theta & -\sin(\theta - \frac{2\pi}{3}) & -\sin(\theta + \frac{2\pi}{3}) \\ \frac{1}{2} & \frac{1}{2} & \frac{1}{2} \end{bmatrix} \tag{2.71}$$

Instead of using stator's voltage phase angle θ, a new angle (θ- θ_r) is used instead, where θ_r is defined as:

$$\theta_r = \int \frac{\omega_s \omega_{r,m}}{\omega^0_{r,m}} \mathrm{d}t \tag{2.72}$$

Where ω_s is grid's nominal frequency, $\omega_{r,m}$ is rotor's instantaneous mechanical angular speed and $\omega^0_{r,m}$ is rotor's synchronous mechanical angular speed. Both rotor and stator currents are transformed into dq axis with above transformation, then the flux angle is calculated as:

$$\varphi_{flux} = \tan^{-1}\left(\frac{(I_{rq} + I_{sq})L_m}{(I_{rd} + I_{sd})L_m}\right) = \tan^{-1}\left(\frac{I_{rq} + I_{sq}}{I_{rd} + I_{sd}}\right) \tag{2.73}$$

Where L_m is magnetizing inductance of the DFIG. Leakage inductance L_{ls} is ignored and it is assumed that $L_m + L_{ls} = L_m$.

Previously transformed current signals are then rotated by φ_{flux} in the complex plan:

$$\mathbf{I}^{SFR}_{dq} = \mathbf{I}_{dq} e^{j\varphi_{flux}} \tag{2.74}$$

This will align current signals to SFR, and the angle used for dq transformation is essentially ($\theta - \theta_r + \varphi_{flux}$), which means the sum of rotor speed and rotor flux speed equals to the synchronous speed of the grid under SFR. This angle is also used for transforming reference voltage signals in dq axis back to rotating signals.

In SVR, d axis is aligned with voltage and therefore d axis current corresponds to real power and q axis current corresponds reactive power. However, for SFR, d axis is aligned with stator flux, therefore d axis current corresponds to reactive power and q axis current corresponds to real power.

- RSC outer control loop

Consider the DFIG equivalent circuit shown in Fig. 2.18, ignore resistance and leakage inductance, following diagram can be drawn to illustrate the relationship between stator voltage, stator current and rotor current.

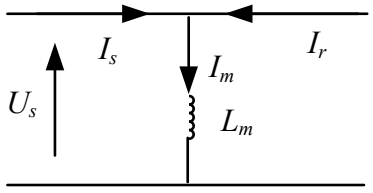

Fig. 2.22 Simplified DFIG equivalent circuit

Note the direction of stator current is reversed to reflect the reference direction used in the Type III WTG. The stator voltage can be written as:

$$\mathbf{u}_s = L_m \frac{\mathrm{d}(\mathbf{i}_s + \mathbf{i}_r)}{\mathrm{d}t} \tag{2.75}$$

Where bold letters represent 3 phase voltage vectors. Applying dq transformation:

$$\begin{aligned} i_{sd} &= -\frac{i_{rd}}{\gamma} + \frac{v_{sq}}{\omega_s L_{ss}} \\ i_{sq} &= -\frac{i_{rq}}{\gamma} - \frac{v_{sd}}{\omega_s L_{ss}} \end{aligned} \tag{2.76}$$

γ is defined as:

$$\gamma = \frac{L_{ls} + L_m}{L_m} = \frac{L_{ss}}{L_m} \tag{2.77}$$

Where L_{ls}, L_{lr} are stator and rotor's leakage inductance. In SFR, stator's voltage is aligned with q axis, therefore $v_{sd} = 0$ and (2.76) can be simplified into:

$$\begin{aligned} i_{sd} &= -\frac{i_{rd}}{\gamma} + \frac{|V_s|}{\omega_s L_{ss}} \\ i_{sq} &= -\frac{i_{rq}}{\gamma} \end{aligned} \tag{2.78}$$

Where $|V_s|$ is the magnitude of DFIG's stator voltage. Equation (2.78) shows that stator current's direction is from grid into the stator, same as shown in Fig. 2.18. Rotor's current flow direction is from RSC into the rotor. SFR can be converted into SVR by rotating the reference frame 90 degrees.

Similar to Type IV WTG, the same MPPT algorithm is used to calculate power extraction from DFIG at given rotor speed. The calculated desired q axis current signal is then fed through the current limiter into inner control loop.

As for d axis current, first consider the q axis current control for stator in SVR. It is calculated based on the stator voltage deviation from nominal value with a proportional gain, plus the voltage control signal from WPC. Like Type IV WTG, the equation for reference q axis stator current is:

$$i^*_{sq} = -K_{pd,rsc}(1 + \Delta U_{wpc} - v_{lv}) \tag{2.79}$$

Where $K_{pd,rsc}$ is the proportional gain, and ΔU_{wpc} is the voltage control signal generated by WPC based on reactive power, voltage or power factor measured at POI. The goal of q axis stator current

control is to maintain stator voltage v_{lv} at 1 pu. Note the reference current signal is inverted (-1) due to different reference current direction in DFIG as discussed above.

Same as Type IV WTG, FRT function is implemented to satisfy grid codes' requirement on voltage support. When FRT is activated, reference q axis current is calculated as:

$$i*_{sq} = -K_{pd,FRT}(1-v_{lv}) \tag{2.80}$$

Where $K_{pd,FRT}$ is the proportional gain used during FRT.

As shown in (2.78), the relationship between d axis rotor current and q axis stator current is:

$$i_{sq}^{SVR} = -\frac{i_{rd}^{SFR}}{\gamma} + \frac{v_{lv}}{\omega_s L_{ss}} \tag{2.81}$$

Rotate the reference frame by 90 degrees into SFR, following equations can be obtained:

$$\begin{aligned} i_{rd}^{*,SFR} &= \gamma K_{pd,rsc}(1+\Delta U_{wpc}-v_{lv}) + \gamma\frac{v_{lv}}{\omega_s L_{ss}} \\ &\approx K_{pd,rsc}(1+\Delta U_{wpc}-v_{lv}) + \frac{v_{lv}}{\omega_s L_m} \end{aligned} \tag{2.82}$$

And during FRT:

$$\begin{aligned} i_{rd,FRT}^{*,SFR} &= \gamma K_{pd,FRT}(1-v_{lv}) + \gamma\frac{v_{lv}}{\omega_s L_{ss}} \\ &\approx K_{pd,FRT}(1-v_{lv}) + \frac{v_{lv}}{\omega_s L_m} \end{aligned} \tag{2.83}$$

Where leakage inductance is ignored and γ=1. Feedforward terms are added to the reference signal after the PI controller.

- Current limiter

Similar to Type IV WTG, current limiter is needed to prevent overcurrent of PWM converter. D axis and q axis currents are first passed through two limiters and limited to their maximum values I_{rd}^{lim} and I_{rq}^{lim} separately. However, the combined total current can still be too large for the converter, therefore a maximum current limit I_r^{lim} is applied to the total converter current. I_r^{lim} is usually larger than I_{rd}^{lim} and I_{rq}^{lim} and is usually determined by the thermal constraints of the PWM converter. Depending on operation modes, priority is given to active or reactive currents. During

normal operation, priority is given to q axis current and it is limited by the maximum q axis current limit I_{rq}^{lim}:

$$i'_{rq} = \min(i^*_{rq}, I_{rq}^{\lim}) \tag{2.84}$$

The d axis current limit is then set to remaining capacity of RSC or maximum q axis current limit, whichever is smaller:

$$i_{rd}^{\max} = \min\left(\sqrt{\left(I_{rsc}^{\lim}\right)^2 - \left(i'_{rq}\right)^2}, I_{rd}^{\lim}\right) \tag{2.85}$$

Finally, d axis current is limited by the calculated maximum limit:

$$i'_{rd} = \min\left(\left|i^*_{rd}\right|, i_{rd}^{\max}\right)\text{sign}\left(i^*_{rd}\right) \tag{2.86}$$

Since d axis reference current i^*_{rd} can be either positive or negative, a sign function is used to return either +1 or -1 to set direction to the limited current.

During FRT, priority is given to d axis current and it is limited by maximum d axis current limit first:

$$i'_{rd} = \min(i^*_{rd}, I_{rd}^{\lim}) \tag{2.87}$$

The q axis current limit is then set to remaining capacity of RSC or maximum q axis current limit, whichever is smaller:

$$i_{rq}^{\max} = \min\left(\sqrt{\left(I_{rsc}^{\lim}\right)^2 - \left(i'_{rd}\right)^2}, I_{rq}^{\lim}\right) \tag{2.88}$$

Finally, q axis current is limited by the calculated maximum limit:

$$i'_{rq} = \min\left(\left|i^*_{rq}\right|, i_{rq}^{\max}\right)\text{sign}\left(i^*_{rq}\right) \tag{2.89}$$

Note that due to SFR orientation is used for RSC, d and q axis are swapped compared to Type IV WTG.

- Inner control loop

The inner control loop of RSC calculates reference voltage signals based on reference current signals given by outer control loop. Consider the DFIG equations given in (2.69) and apply dq transformation in SFR, stator and rotor voltage can be written as:

$$
\begin{aligned}
v_{rd} &= R_r i_{rd} - s\omega_s \lambda_{rq} + \frac{\mathrm{d}\lambda_{rd}}{\mathrm{d}t} \\
v_{rq} &= R_r i_{rq} + s\omega_s \lambda_{rd} + \frac{\mathrm{d}\lambda_{rq}}{\mathrm{d}t} \\
v_{sd} &= R_s i_{sd} - \omega_s \lambda_{sq} + \frac{\mathrm{d}\lambda_{sd}}{\mathrm{d}t} \\
v_{sq} &= R_s i_{sq} + \omega_s \lambda_{sd} + \frac{\mathrm{d}\lambda_{sq}}{\mathrm{d}t}
\end{aligned}
\tag{2.90}
$$

Where s is slip and ω_s is angular frequency of stator. λ is defined as:

$$
\begin{aligned}
\lambda_{rd} &= L_{rr} i_{rd} + L_m i_{sd} \\
\lambda_{rq} &= L_{rr} i_{rq} + L_m i_{sq} \\
\lambda_{sd} &= L_{ss} i_{sd} + L_m i_{rd} \\
\lambda_{sq} &= L_{ss} i_{sq} + L_m i_{rq}
\end{aligned}
\tag{2.91}
$$

Since SFR is used, flux is aligned with d axis, therefore λ_{sq} is zero:

$$
\begin{aligned}
\lambda_{sq} &= L_{ss} i_{sq} + L_m i_{rq} = 0 \\
i_{sq} &= -\frac{L_m i_{rq}}{L_{ss}}
\end{aligned}
\tag{2.92}
$$

Also set derivative terms in (2.90) to zero:

$$
\begin{aligned}
\frac{\mathrm{d}\lambda_{sd}}{\mathrm{d}t} &= L_{ss} \frac{\mathrm{d}i_{sd}}{\mathrm{d}t} + L_m \frac{\mathrm{d}i_{rd}}{\mathrm{d}t} = 0 \\
\frac{\mathrm{d}\lambda_{sq}}{\mathrm{d}t} &= L_{ss} \frac{\mathrm{d}i_{sq}}{\mathrm{d}t} + L_m \frac{\mathrm{d}i_{rq}}{\mathrm{d}t} = 0
\end{aligned}
\tag{2.93}
$$

Substitute (2.92) and (2.93) into (2.90):

$$
\begin{aligned}
v_{rd} &= R_r i_{rd} - s\omega_s L_x i_{rq} + L_x \frac{\mathrm{d}i_{rd}}{\mathrm{d}t} \\
v_{rq} &= R_r i_{rq} + s\omega_s (L_{rr} i_{rd} + L_m i_{sd}) + L_x \frac{\mathrm{d}i_{rq}}{\mathrm{d}t}
\end{aligned}
\tag{2.94}
$$

Where L_x is defined as:

$$
L_x = L_{rr} - \frac{L_m^2}{L_{ss}} = L_{lr} + L_m - \frac{L_m^2}{L_{ss}} = L_{lr} + \frac{L_{ls} L_m}{L_{ls} + L_m} = L_{lr} + \frac{L_{ls}}{\gamma}
\tag{2.95}
$$

Equation (2.95) is used for the PI controller design for inner control loop. Ignore rotor winding resistance ($R_r=0$) and replace derivative terms with PI controllers:

$$\begin{aligned} v_{rd}^{'} &= K_{p,rsc}\left(i_{rd}^{'}-i_{rd}\right)+K_{i,rsc}\int\left(i_{rd}^{'}-i_{rd}\right)\mathrm{d}t-\omega_r L_\sigma i_{rq} \\ v_{rq}^{'} &= K_{p,rsc}\left(i_{rq}^{'}-i_{rq}\right)+K_{i,rsc}\int\left(i_{rq}^{'}-i_{rq}\right)\mathrm{d}t+\omega_r\left[(L_M+L_\sigma)i_{rd}+L_M i_{sd}\right] \end{aligned} \tag{2.96}$$

Where $\omega_r = s\omega_s$ is electric angular frequency of rotor, K_p and K_i are proportional and integral gains of the PI controller. L_M and L_σ are defined as:

$$L_M = \gamma L_m, L_\sigma = \gamma^2 L_x \tag{2.97}$$

Anti-windup is usually equipped with the PI controller for inner control loop, therefore the integral part of the PI controller will be limited when the output of PI controller is limited. The output of the PI controller is usually limited to 0.2γ pu to prevent over correction. Divide equations (2.96) by γ^2 on both sides, it can be transformed into:

$$\begin{aligned} v_{rd}^{'} &= \frac{K_{p,rsc}}{\gamma^2}\left(i_{rd}^{'}-i_{rd}\right)+\frac{K_{i,rsc}}{\gamma^2}\int\left(i_{rd}^{'}-i_{rd}\right)\mathrm{d}t-\omega_r L_x i_{rq} \\ v_{rq}^{'} &= \frac{K_{p,rsc}}{\gamma^2}\left(i_{rq}^{'}-i_{rq}\right)+\frac{K_{i,rsc}}{\gamma^2}\int\left(i_{rq}^{'}-i_{rq}\right)\mathrm{d}t+\omega_r\left[L_{rr}i_{rd}+L_m i_{sd}\right] \end{aligned} \tag{2.98}$$

Where $\omega_r\left[L_{rr}i_{rd}+L_m i_{sd}\right]$ and $-\omega_r L_x i_{rq}$ are feed forward terms that will be added into the PI controller outputs to fix PI output to zero in steady state. The calculated reference voltage signals are then transformed into abc frame with inverse clark transformation, finally normalized and fed into the PWM converter.

2.2.2.3 GSC Controller

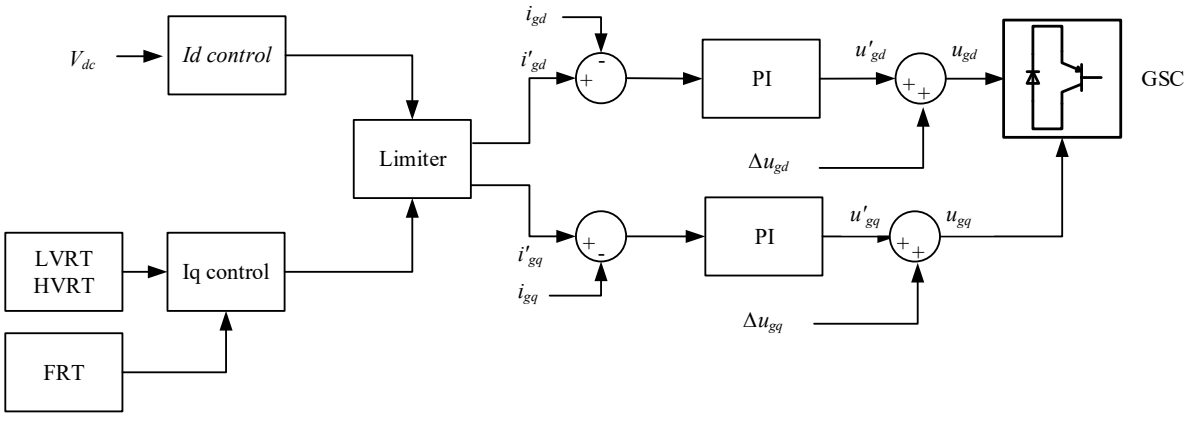

Fig. 2.23 GSC controller

The GSC part of the controller is shown in Fig. 2.23. Unlike RSC, GSC operates in SVR, therefore d axis current corresponds to real power and q axis current corresponds to reactive power. GSC controls DC bus voltage and reactive power injection to the grid during FRT.

- Outer control loop

Similar to Type IV WTG, d axis reference current is obtained by a PI controller based on the deviation of DC bus voltage from 1 pu:

$$i_{gd}^{*} = K_p\left(U_{DC}^{'} - U_{DC}\right) + K_i\int\left(U_{DC}^{'} - U_{DC}\right)\mathrm{d}t \tag{2.99}$$

Where K_p and K_i are PI controller parameters, $U^{'}_{DC}$ is reference DC voltage which is 1 pu and U_{DC} is measured DC bus voltage. However, unlike Type IV WTG where i^{*}_{sd} is always positive, i^{*}_{sd} for DFIG can be either positive or negative, as the power flow on DC bus is bidirectional. The direction of power flow depends on the rotor speed of DFIG.

Q axis current of GSC is usually zero in steady state, which means the GSC will not inject reactive power into the grid. When FRT is activated, GSC will inject additional reactive power to support grid voltage in case reactive power provided by the stator winding is not enough. When FRT is activated, the q axis reference current is calculated as:

$$i_{gq}^{*} = \min\left(i_{rd}^{'} - i_{rd}, 0\right) = \min\left(I_{rd}^{\lim} - \left[\frac{v_{lv}}{\omega_s L_m} + K_{FRT}\left(1 - v_{lv}\right)\right], 0\right) \tag{2.100}$$

Similar to RSC, calculated d and q axis current signals are passed through a current limiter to prevent overcurrent. Unlike RSC, the priority of current limiter is always given to q axis current:

$$i_{gq}^{'} = \max\left(i_{gq}^{*}, -I_{gq}^{\lim}\right) \tag{2.101}$$

Note the reactive power output of GSC will always be negative hence the negative sign. d axis current will be limited to the remaining capacity of the converter output:

$$\begin{aligned} i_{gd}^{\max} &= \min\left(\sqrt{\left(I_{gsc}^{\lim}\right)^2 - \left(i_{gq}^{'}\right)^2}, I_{gd}^{\lim}\right) \\ i_{gd}^{'} &= \min\left(\left|i_{gd}^{*}\right|, i_{gd}^{\max}\right)\mathrm{sign}\left(i_{gd}^{*}\right) \end{aligned} \tag{2.102}$$

Since the capacity of PWM converters are much smaller than Type IV WTG, the current limit will also be smaller.

- Inner control loop

Inner control loop of GSC is used to calculate GSC voltages with reference current signals. Consider the choke filter's voltage equation given in (2.14):

$$\mathbf{v}_{lv} = R\mathbf{i}_g + L\frac{\mathrm{d}\,\mathbf{i}_g}{\mathrm{d}\,t} + \mathbf{v}_{gsc} \tag{2.103}$$

Apply dq transformation to it:

$$\begin{aligned} v_{cd} &= -Ri_{gd} - L\frac{\mathrm{d}\,i_{gd}}{\mathrm{d}\,t} + \omega_s L i_{gq} + v_{gd} \\ v_{cq} &= -Ri_{gq} - L\frac{\mathrm{d}\,i_{gq}}{\mathrm{d}\,t} - \omega_s L i_{gd} + v_{gq} \end{aligned} \tag{2.104}$$

Where v_{cd} and v_{cq} are converter voltage in d and q axis, ω_s is grid frequency, v_{gd} and v_{gq} are LV bus voltage in d and q axis. Replacing derivative terms with PI controllers:

$$\begin{aligned} v'_{cd} &= -Ri_{gd} - \left[K_p\left(i'_{gd} - i_{gd}\right) + K_i\int\left(i'_{gd} - i_{gd}\right)\mathrm{d}\,t\right] + \omega_s L i_{gq} + v_{gd} \\ v'_{cq} &= -Ri_{gq} - \left[K_p\left(i'_{gq} - i_{gq}\right) + K_i\int\left(i'_{gq} - i_{gq}\right)\mathrm{d}\,t\right] - \omega_s L i_{gd} + v_{gq} \end{aligned} \tag{2.105}$$

Where K_p and K_i are PI controller parameters. Since choke resistance is usually very small and can be neglected, above equations can be further simplified into:

$$\begin{aligned} v'_{cd} &= -\left[K_p\left(i'_{gd} - i_{gd}\right) + K_i\int\left(i'_{gd} - i_{gd}\right)\mathrm{d}\,t\right] + \omega_s L i_{gq} + v_{gd} \\ v'_{cq} &= -\left[K_p\left(i'_{gq} - i_{gq}\right) + K_i\int\left(i'_{gq} - i_{gq}\right)\mathrm{d}\,t\right] - \omega_s L i_{gd} + v_{gq} \end{aligned} \tag{2.106}$$

Feedforward terms $\omega_s L i_{gq} + v_{gd}$ and $-\omega_s L i_{gd} + v_{gq}$ are added to d and q axis respectively to make PI controller's output close to 0 in steady state. Output voltage signals are limited to 1 pu. to prevent overvoltage of GSC controller, then passed to the PWM converter.

CHAPTER 3 EMT MODELING IN PF

DIgSILENT PowerFactory (PF) is a power system simulation and analysis software widely used in the industry. Compared with other simulation software like EMT-type or Matlab Simulink, it offers some advantages. PF is implemented as a single package while supporting many different calculation functions. There is no need to reload modules and update or transfer data and results between different programs. As an example, the Load Flow, Short-Circuit, and Harmonic Load Flow analysis tools can be executed sequentially without resetting the program, enabling additional software modules and engines, or reading and converting external data files. Therefore, the comparison between RMS and EMT simulation results can be done within the same software environment.

3.1 EMT Type IV WP modelling in PF

For EMT Type IV WP, the exact same electrical model as existing EMT model is constructed in PF, as shown below:

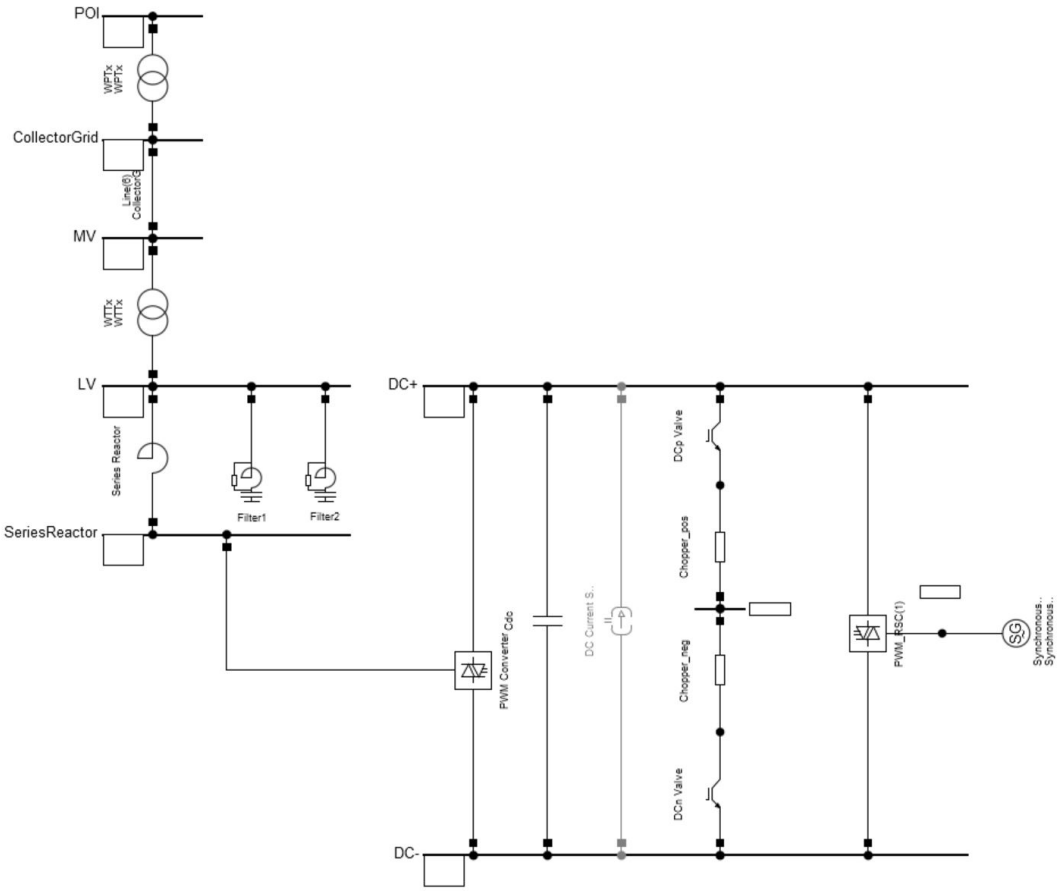

Fig. 3.1 Electrical components of Type IV WP

Synchronous generator is driven by a wind turbine and generates electrical power. The output of the generator is connected to the MSC, which is also connected to the DC bus. DC bus capacitor is used for filtering and chopper protection circuit is used to prevent overvoltage on DC bus. GSC is connected to the other side of DC bus and links DC bus to low voltage bus through a series reactor. Low voltage bus is connected to POI through WT transformer, collector grid and WP transformer.

3.1.1 Wind turbine and two mass model

The complete mechanical model of the generator and wind turbine are built from scratch, including the wind turbine model and two mass model linking the wind turbine to the synchronous generator.

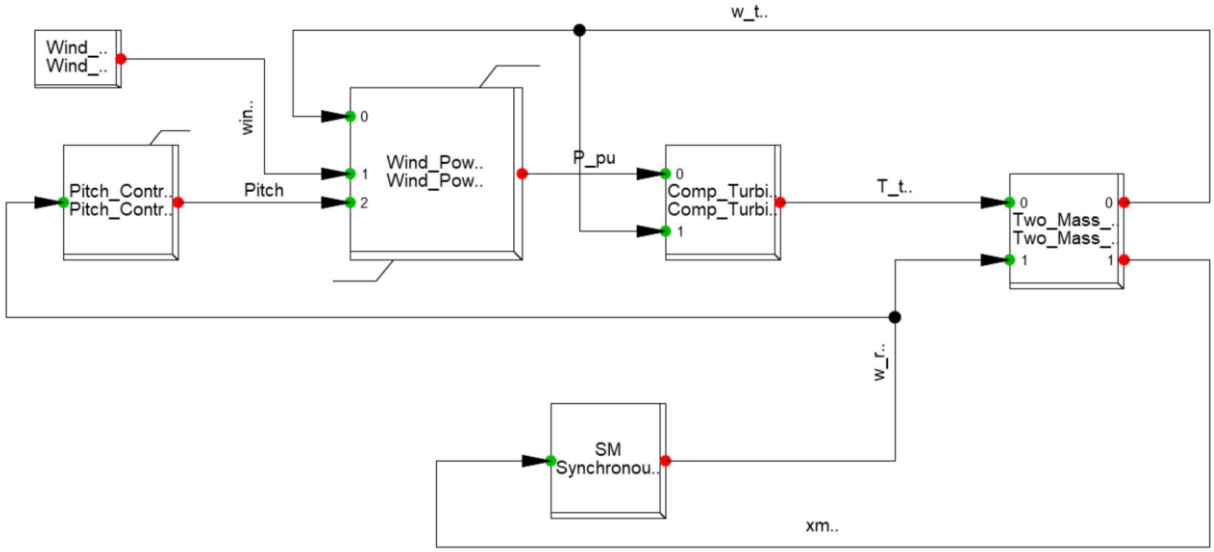

Fig. 3.2 Mechanical model of Type IV WP

As shown in Chapter 2, wind power harvested by the wind turbine at given wind speed and pitch angle is calculated with function (2.2). The block diagram is constructed as shown in Fig. 3.3.

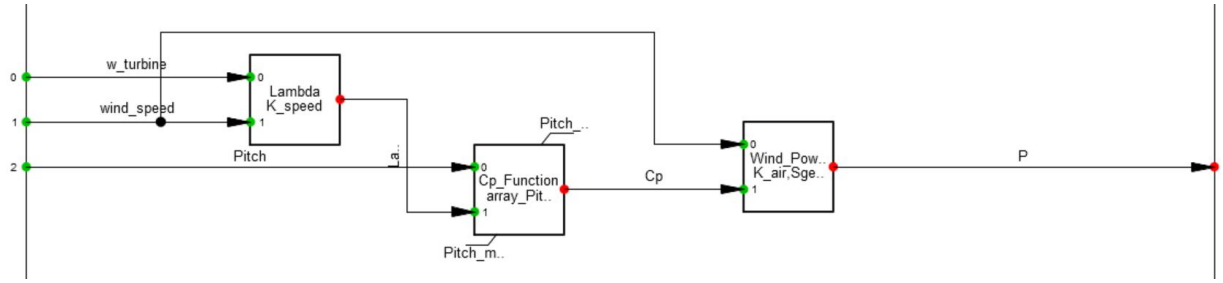

Fig. 3.3 Wind power calculation of wind turbine

To prevent overspeed of wind turbine, an additional pitch angle controller is added which would increase the pitch angle when generator speed exceeds maximum value. The pitch angle is controlled by a PID controller:

$$\beta_{pitch} = \text{round}\left(K_{p,pitch}\left(\omega_{rm} - \omega_{rm,\max}\right) + K_{i,pitch}\int\left(\omega_{rm} - \omega_{rm,\max}\right)\mathrm{d}t + K_{d,pitch}\frac{\mathrm{d}\left(\omega_{rm} - \omega_{rm,\max}\right)}{\mathrm{d}t}\right) \tag{3.1}$$

Where $K_{pid,pitch}$ are PID controller parameters. The pitch angle is also rounded and rate limited, and diagram of the pitch angle controller is shown in Fig. 3.4:

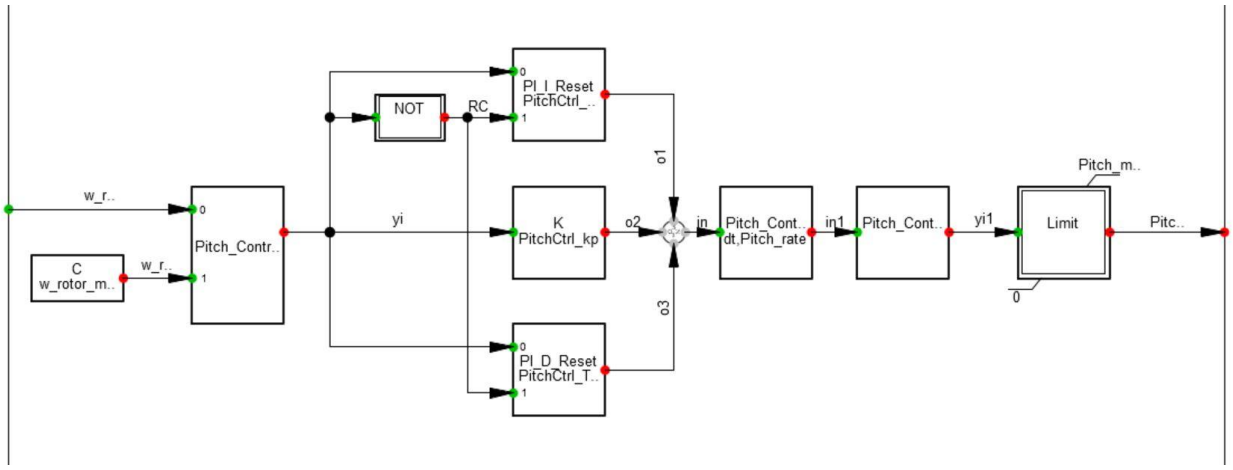

Fig. 3.4 Pitch angle control of WT

The calculated wind power output is then passed down to the two-mass model. The same two-mass model as described in equation (2.1) is built in PF and the calculated speed signal drives the synchronous generator.

3.1.2 MSC controller

As described in section 2.1.2, the same MSC controller is constructed as the mathematical model. SVR reference frame is used for consistency. MSC consists of outer control loop and inner control loop, the full structure of MSC is shown in Fig. 3.5:

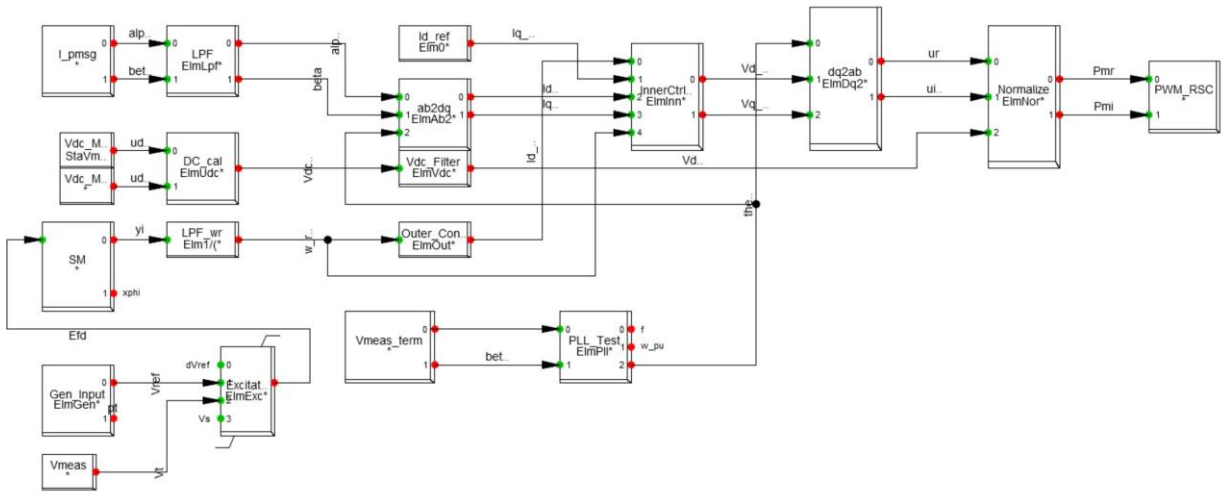

Fig. 3.5 MSC controller diagram for Type IV WP

An excitation control model is added to inject excitation current into the synchronous generator's rotor winding. Since PF does not offer a PMSG model, a constant excitation current is injected to simulate a PMSG. Same as EMTP model, current and voltage measurement units take measurement from the electrical part of the model, and pass measured current and voltage signals in alpha-beta reference frame through low pass filters, finally converted into dq reference frame. Since the model is built with AVM model and PWM converters work as controlled voltage sources, input filters aren't necessary. However, since they introduce additional delay into the control system, they are kept and same values are used to maintain consistency with the EMTP model.

For better performance in unbalanced conditions, the DSRF PLL described in section 2.1.2.3 is used. The PLL is constructed as shown in Fig. 3.6:

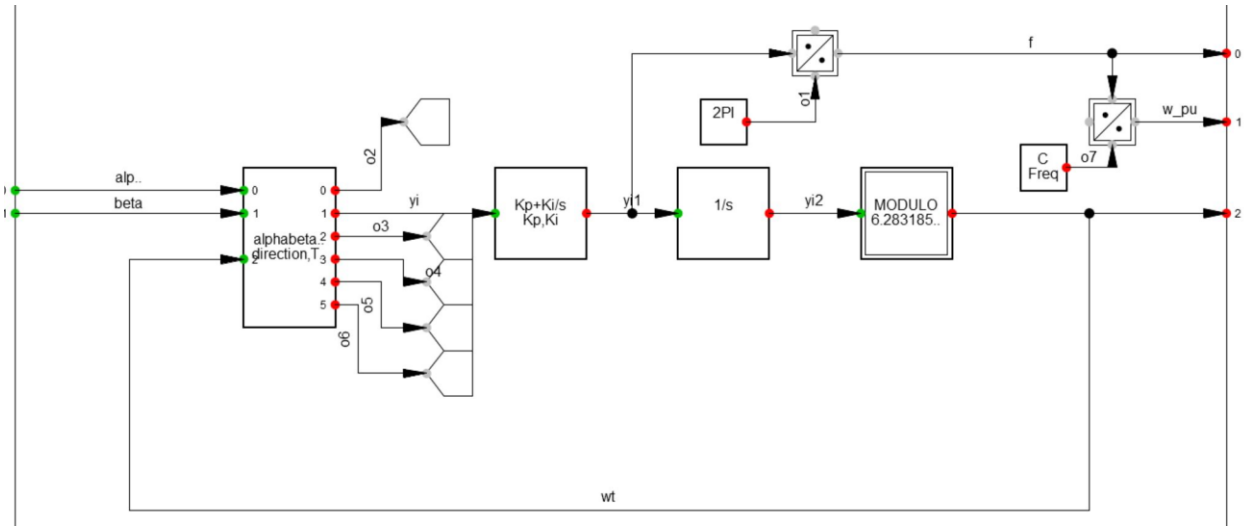

Fig. 3.6 DSRF-PLL model in Type IV WP

Since SVR reference frame is used, positive sequence d axis is aligned with positive sequence voltage, therefore positive sequence q axis component is controlled to be zero by adjusting the angle used for dq transformation. The decoupling between positive sequence and negative sequence is achieved by equation (2.26).

The same decoupling network is constructed in PF. Additional low pass filters are added to the output to filter out high frequency harmonics:

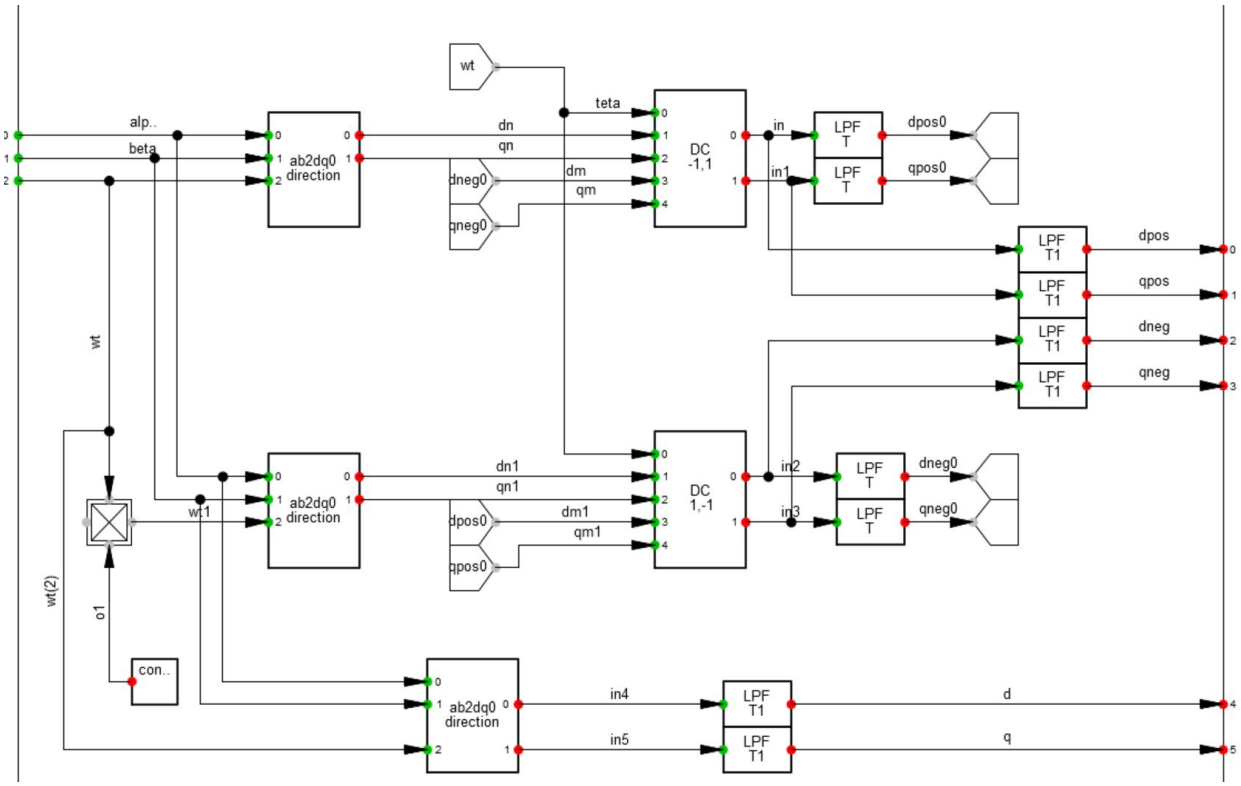

Fig. 3.7 Decoupling Network in DSRF PLL

Measured signals are filtered by the second order Butterworth filter with transfer function:

$$H_f(s) = \frac{1}{1 + \frac{\sqrt{2}s}{\omega_c} + \frac{s^2}{\omega_c}} \tag{3.2}$$

Where ω_c is the cut-off frequency of the measurement filter.

The same outer control loop as described in Chapter 2 is used to generate reference current signals for d and q axis. Since SVR is used, d axis current corresponds to real power and q axis current corresponds to reactive power. The d axis current reference is calculated with MPPT algorithm:

$$i_{rd}^{'} = \omega_{rm}{}^2 K_{optimal\_pu} \tag{3.3}$$

where ω_{rm} is rotor speed in pu, $K_{optimal\_pu}$ is MPPT factor. For this model, Q is controlled to be zero, therefore q axis current is controlled to be zero, which gives:

$$i_{rq}^{'} = 0 \tag{3.4}$$

Since q axis current is always zero and d axis current is calculated based on rotor's mechanical speed, current limiter is omitted here. Calculated reference current signals are passed to inner control loop, where reference voltage signals are calculated with PI controllers. Output of the inner control loop can be written as:

$$\begin{aligned} u_{sd}^{'} &= r_s i_{sd} + K_{p,inner}\left(i_{sd}^{'} - i_{sd}\right) + K_{i,inner}\int\left(i_{sd}^{'} - i_{sd}\right)\mathrm{d}t - \omega_e L i_{sq} \\ u_{sq}^{'} &= r_s i_{sd} + K_{p,inner}\left(i_{sq}^{'} - i_{sq}\right) + K_{i,inner}\int\left(i_{sq}^{'} - i_{sq}\right)\mathrm{d}t + \omega_e (L i_{sd} + \psi_{pm}) \end{aligned} \tag{3.5}$$

$-\omega_e L i_{sq}$ and $\omega_e (L i_{sd} + \psi_{pm})$ are feedforward terms and are calculated and added back to PI controller output to make its steady state output to zero. The inner control loop diagram for d and q axis is shown in Fig. 3.8.

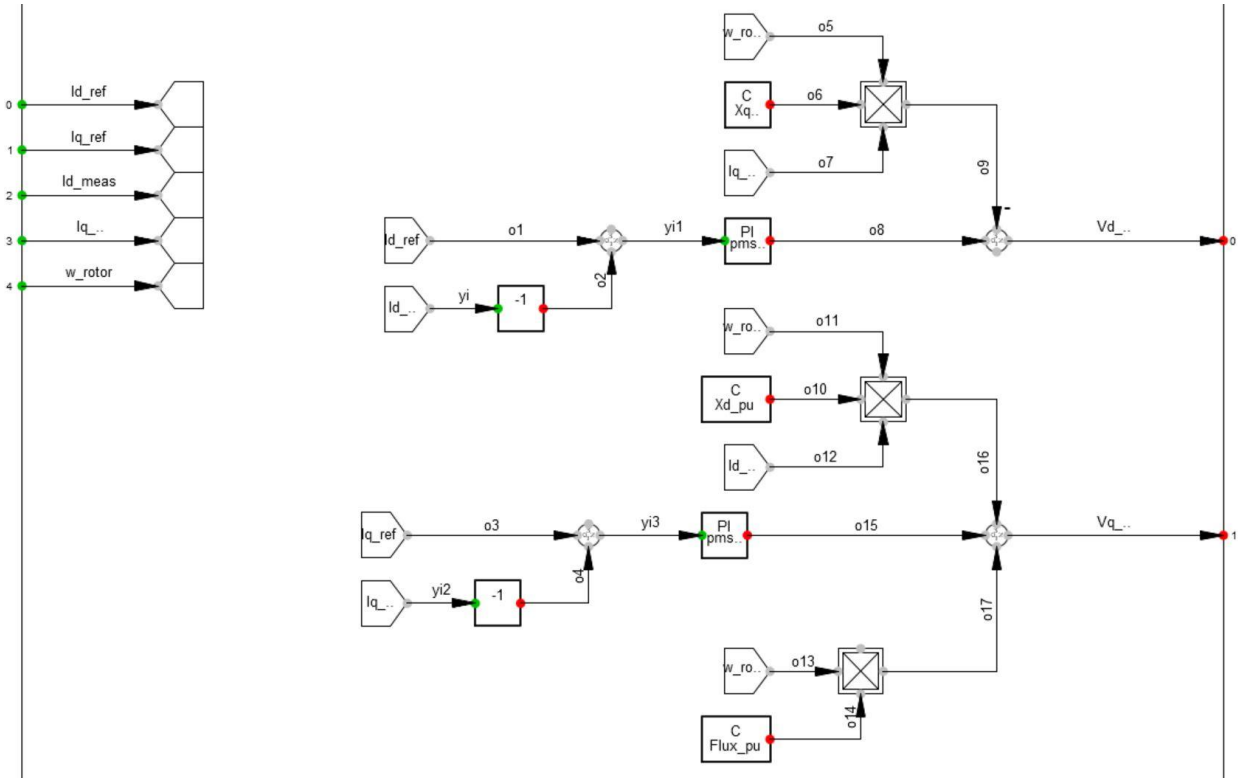

Fig. 3.8 MSC inner control loop

Finally, calculated reference voltage signals are converted back to abc reference frame with inverse clark transformation, normalized and fed into the PWM converter.

3.1.3 GSC controller

The GSC controller described in Chapter 2 is constructed from scratch. It consists of filters, PLL, WPC, outer control loop and inner control loop. Same as MSC, SVR reference frame is used, therefore d axis current corresponds to real power output of GSC, and q axis current corresponds to reactive power output. The structure of GSC controller is shown in Fig. 3.9:

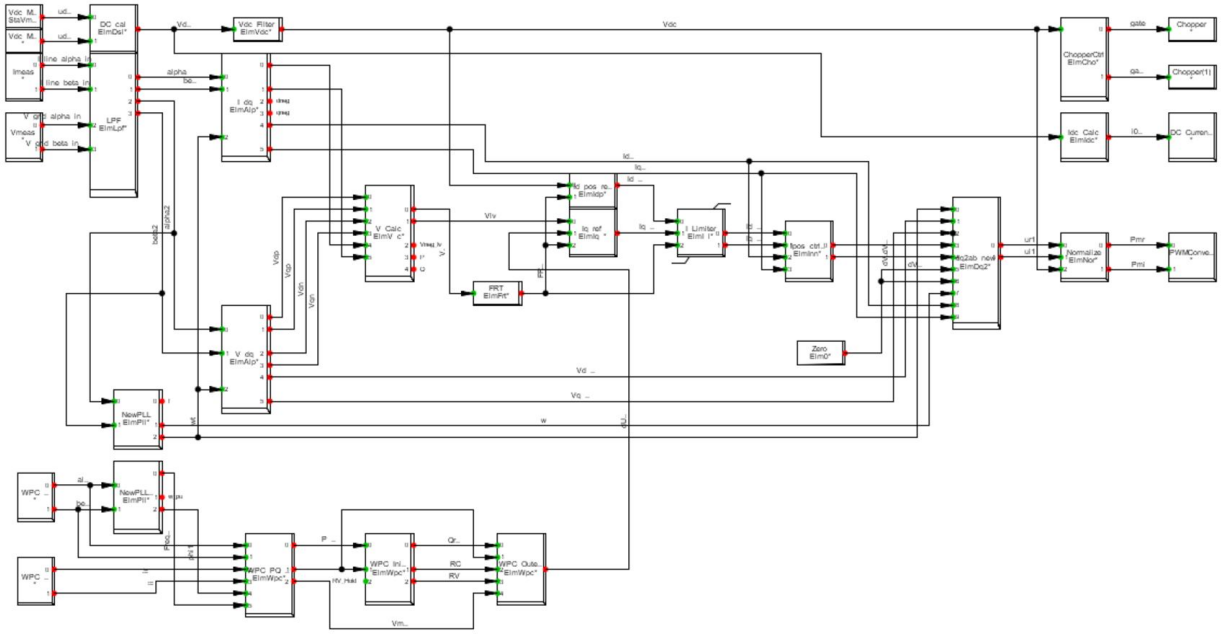

Fig. 3.9 GSC controller in Type IV WP

Same as MSC, measured current and voltage signals are filtered and transformed into dq axis. PLL is used to calculate the voltage angle, and since SVR is used, d axis voltage is aligned with stator voltage and q axis voltage is zero. The same PLL and filter structure is used in GSC controller as MSC so omitted here.

D axis outer control loop of GSC calculates reference current signals based on DC bus voltage using PI controller. The construction is shown in Fig. 3.10.

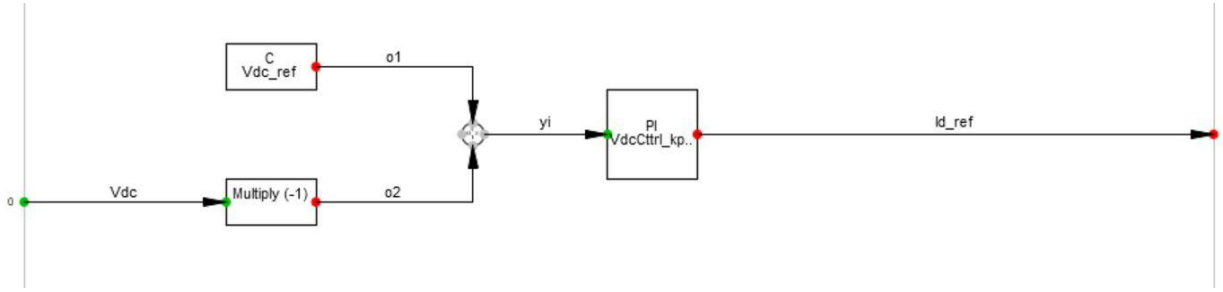

Fig. 3.10 DC voltage control

Output reference signal can be written as:

$$i_{gd}^{*} = K_p\left(U_{DC}^{'} - U_{DC}\right) + K_i\int\left(U_{DC}^{'} - U_{DC}\right)\mathrm{d}t \tag{3.6}$$

Where K_p and K_i are PI controller parameters, $U_{DC}^{'}$ is reference DC voltage which is set at 1 pu and U_{DC} is measured DC bus voltage.

Q axis outer control loop generates q axis current reference based on low voltage bus voltage deviation from 1 pu, as well as WPC's output. WPC uses its own PLL since the voltage angle at WPC is different from the one on DC bus, but the PLL structure as well as the Clark transformation are the same as low voltage controller. After transforming voltage and current signals into dq axis, real and reactive power output of the WP at POI is calculated, the equation used for calculation is given by:

$$\begin{aligned} P_{POI} &= \frac{3}{2}(u_d i_d + u_q i_q) \\ Q_{POI} &= \frac{3}{2}(u_q i_d - u_d i_q) \end{aligned} \tag{3.7}$$

Different control method of WPC can be applied, such as Q control, V control and power factor control. In this model, Q control is used and reactive power output of the WP is controlled at zero. A PI controller is used and the equation of the control loop is given by:

$$dU_{ref} = K_{p,WPC}\left(Q_{POI}^{'} - Q_{POI}\right) + K_{i,WPC}\int\left(Q_{POI}^{'} - Q_{POI}\right)\mathrm{d}t \tag{3.8}$$

To prevent overcorrection due to accumulated error during the initialization period of the model, a timer is used to reset the PI controller after the model reaches steady state, and output of WPC is set to zero during model's initialization.

Output of WPC is fed into the outer control loop of q axis. The output of the outer control loop is written as:

$$i^*_{gq} = K_{pq,gsc}(1 + \Delta U_{wpc} - v_{lv}) \tag{3.9}$$

$K_{pq,gsc}$ is a proportional gain, and is usually set to 2. As discussed before, FRT function is required by some grid codes so that the WP can supply reactive current during faults to support grid voltage. The FRT function is built with S-R flip flops and a timer to prevent frequent activation of FRT function during a transient. When FRT is activated, WPC's control signal is ignored and the output of q axis outer control loop is calculated as:

$$i^*_{gq} = K_{pq,FRT}(1 - v_{lv}) \tag{3.10}$$

Where $K_{pq,gsc}$ is a proportional gain used during FRT. To prevent overcurrent, the current limiter is used to limit reference current signals. The structure of the current limiter is shown in Fig. 3.11:

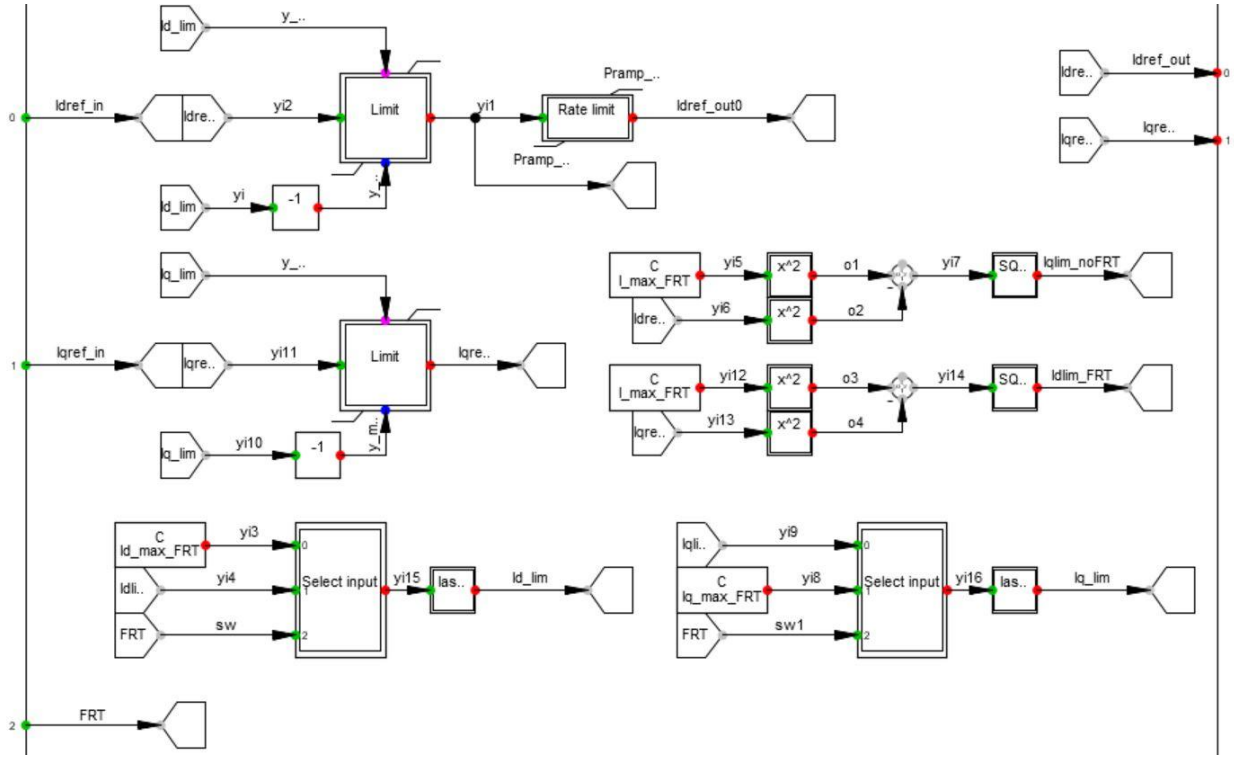

Fig. 3.11 Current limiter of GSC

Depending on whether FRT is activated, priority is given to either q axis or d axis current signals. Output current signals are fed into the inner control loop. According to section 2.1.2.5, the inner control loop can be written as:

$$
\begin{aligned}
v'_{cd} &= -\left[K_p\left(i'_{gd}-i_{gd}\right)+K_i\int\left(i'_{gd}-i_{gd}\right)\mathrm{d}t\right]+\omega_s L i_{gq}+v_{gd} \\
v'_{cq} &= -\left[K_p\left(i'_{gq}-i_{gq}\right)+K_i\int\left(i'_{gq}-i_{gq}\right)\mathrm{d}t\right]-\omega_s L i_{gd}+v_{gq}
\end{aligned}
\tag{3.11}
$$

Therefore, two PI controllers are used to build the inner control loop, as shown in Fig. 3.12:

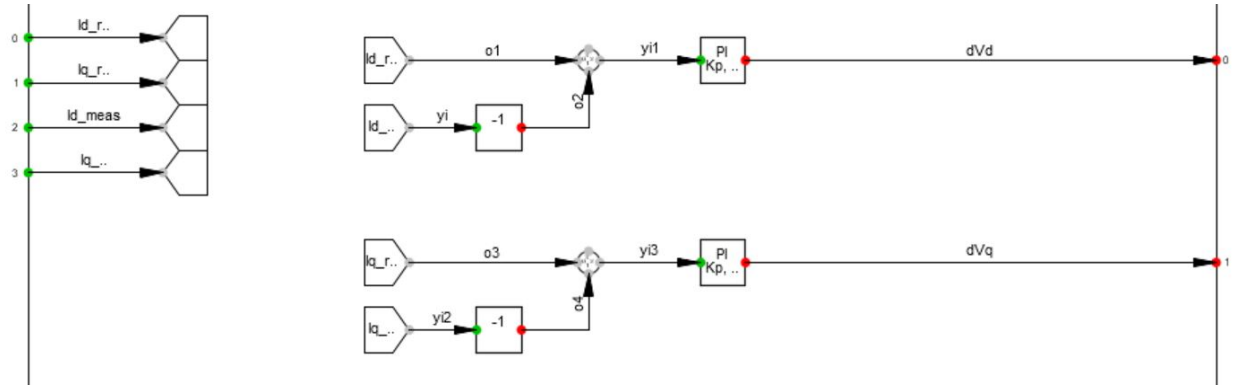

Fig. 3.12 Inner control loop of GSC

Note feed forward terms $\omega_s L i_{gq}+v_{gd}$ and $-\omega_s L i_{gd}+v_{gq}$ are moved inside the dq to abc transformation block and added back to reference voltage signals:

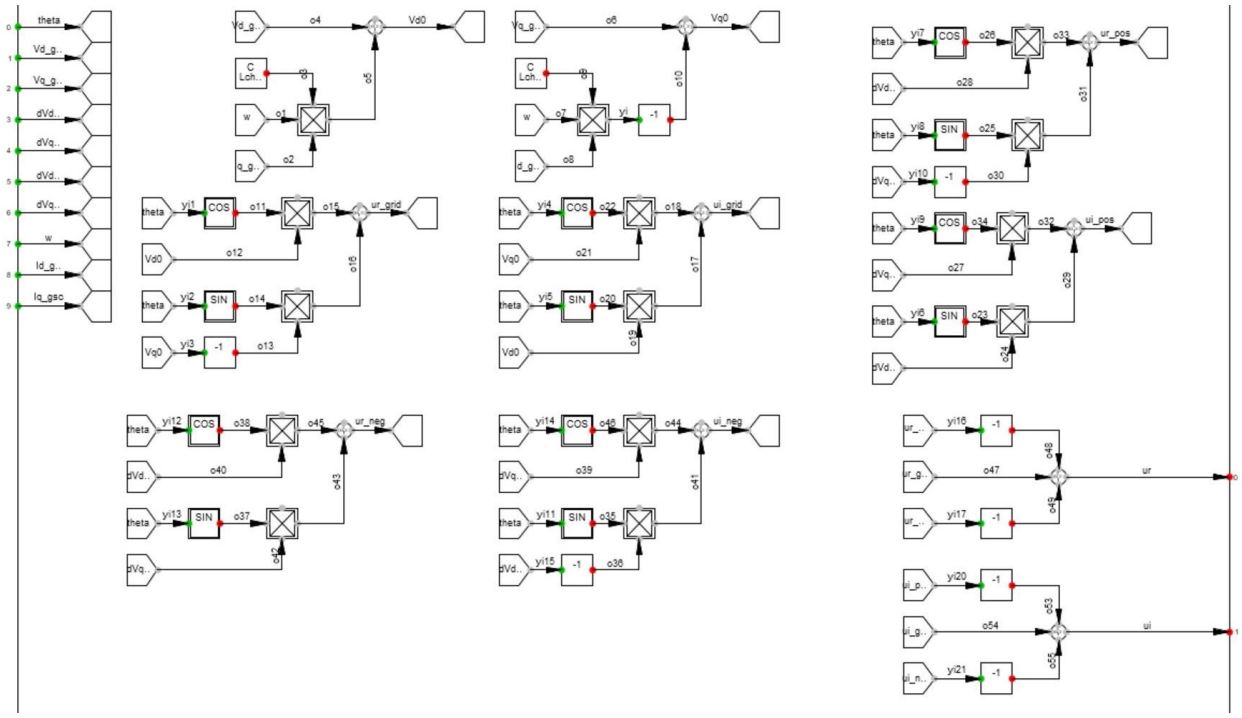

Fig. 3.13 dq to alpha-beta conversion with feedforward signals injection

Finally, reference voltage signals for GSC are transformed back into abc reference frame with inverse transformation matrix defined in Chapter 2, equalized and fed into the PWM converter.

3.2 EMT Type III WP modelling in PF

Similar to Type IV WP, the same electrical network is built. Instead of synchronous generator, DFIG is used in this model, with its stator winding connected to the low voltage bus directly. Rotor winding is connected to RSC, which is then connected to the DC bus, GSC, series reactor and finally low voltage bus.

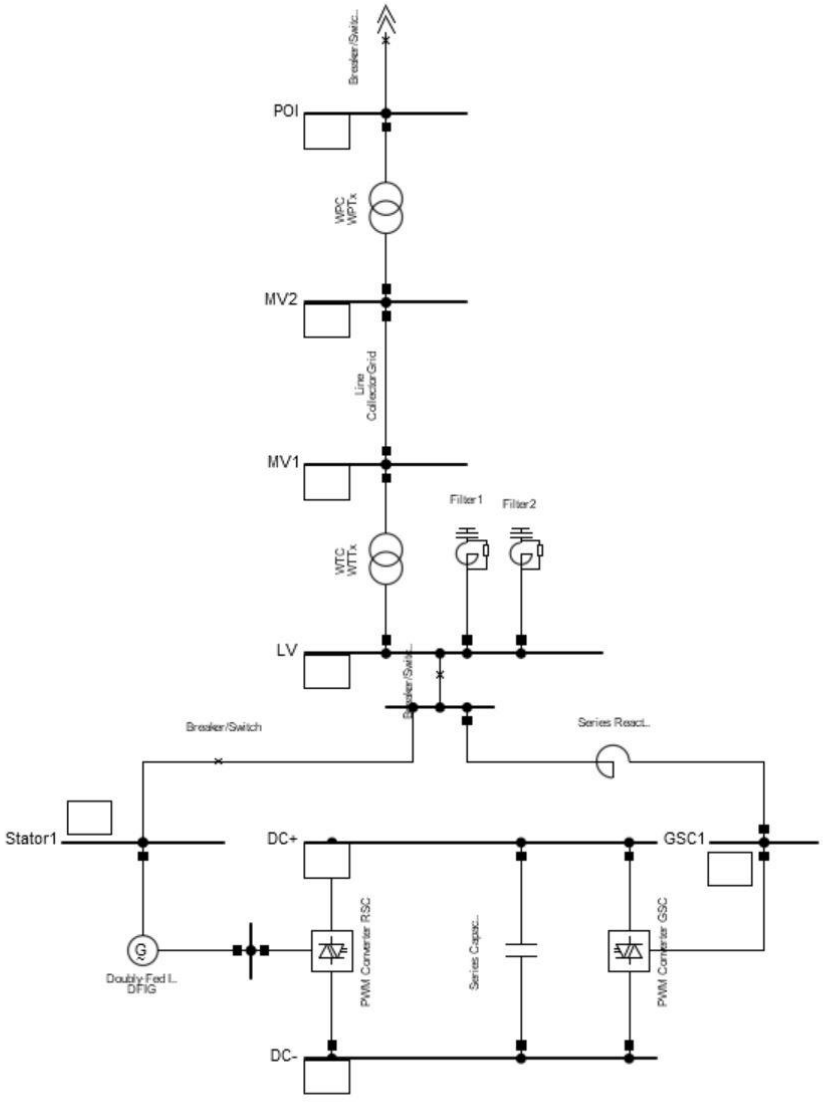

Fig. 3.14 Electrical components of Type III WP

The mechanical model of the wind turbine, as well as two mass model are exactly the same as Type IV WP, therefore omitted here.

3.2.1 RSC controller design

In original EMTP model, SFR is used and d axis current is aligned with stator flux. It has been proven in many researches that SFR and SVR are very close in steady state. However, during transients, sudden change of stator voltage and phase shift between the flux and voltage are not the same as in steady state. Therefore, in SFR, the flux magnitude and rotor's mechanical speed may vary during a voltage dip. Moreover, the difference caused by the sudden change of stator flux and voltage during transients may also cause controller instability, depending on the d axis component of the current. Under same scenarios, controller designed with SVR are always stable. The main cause of this issue is the flux calculation process, as discussed in Chapter 2.

During transient, the flux angle calculation method using stator and rotor currents will cause error due to the nonlinearity between current and DFIG inductances. Therefore, the stability of the controller will be negatively impacted. Another method for flux angle calculation is based on integration, however due to the integrator used not being ideal, first order transfer function is used to remove static error. As a result, integral type flux observer also introduces unexpected error for the orientation during transient. Therefore, in the PF model, SVR will be employed to develop Type III WP mode.

The RSC controller is shown in Fig. 3.15:

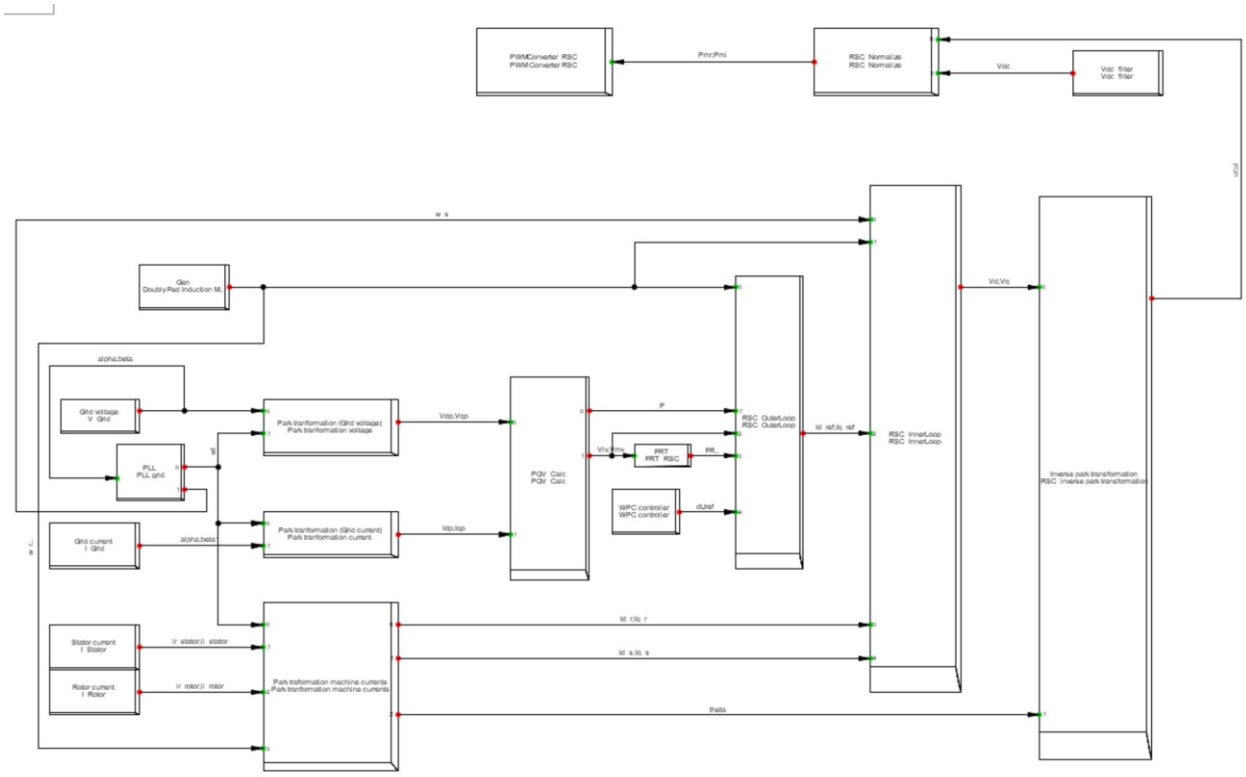

Fig. 3.15 RSC controller diagram in Type IV WP

Unlike the EMTP model discussed before, voltage angle used for dq transformation is generated by PLL. Moreover, d and q axis are swapped in the proposed model, since the reference frame rotates by 90 degrees. The relationship between SVR and SFR reference frames is shown in Fig. 3.16:

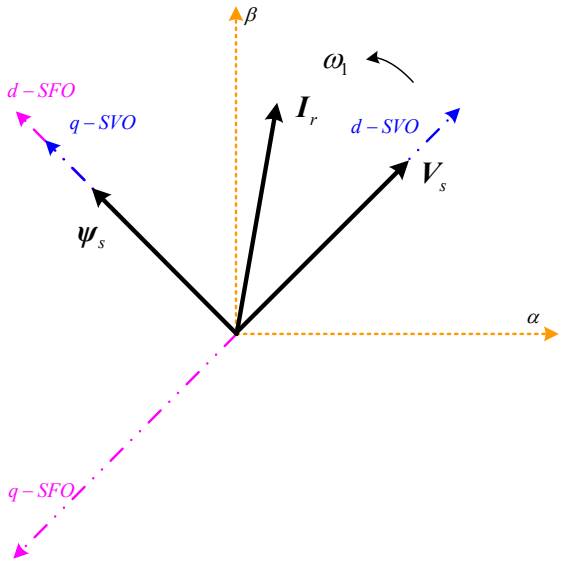

Fig. 3.16 SVR vs SFR Relationship

The conversion can also be written as:

$$I_{rd}^{SVR} = -I_{rq}^{SFR}$$
$$I_{rq}^{SVR} = I_{rd}^{SFR} \tag{3.12}$$

The dq conversion in SVR is shown in Fig. 3.17:

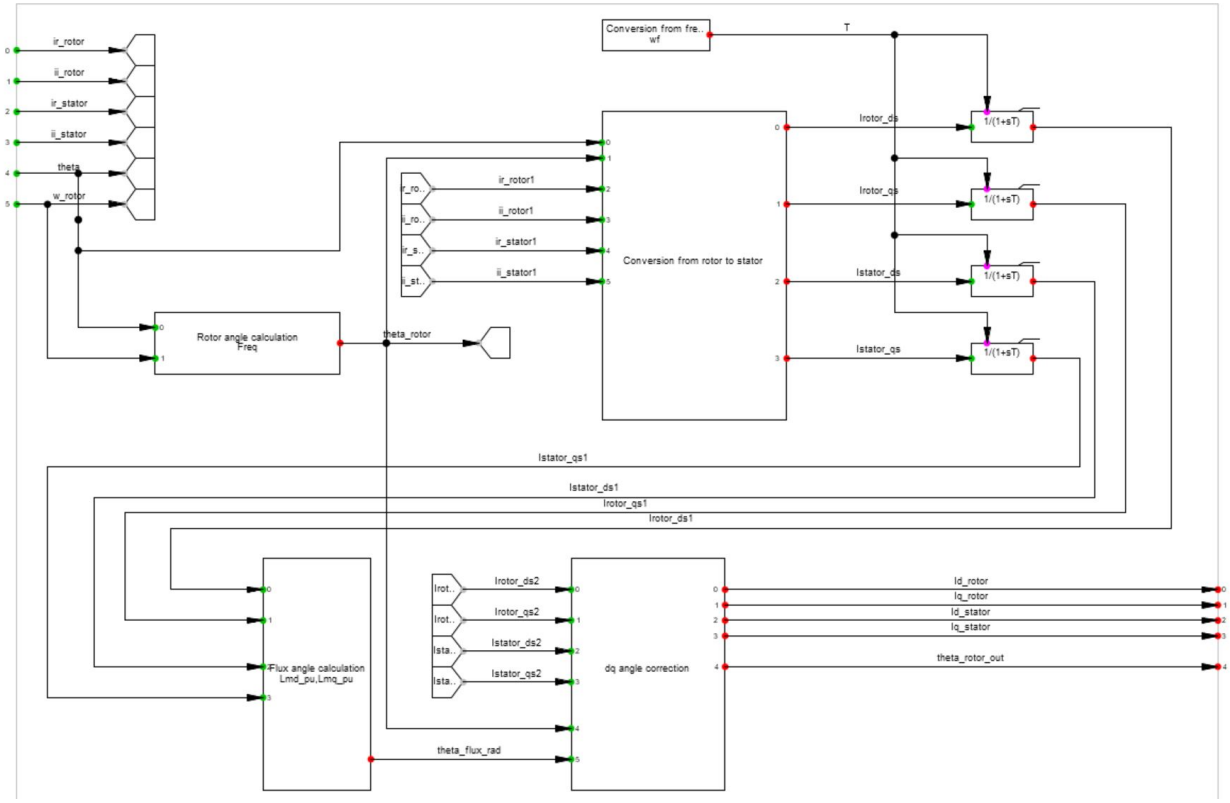

Fig. 3.17 alpha-beta to dq conversion

Note that the angle used for rotor current dq transformation is generated by PLL and rotor's mechanical speed directly, no flux angle calculation is needed.

The outer control loop is shown in Fig. 3.18:

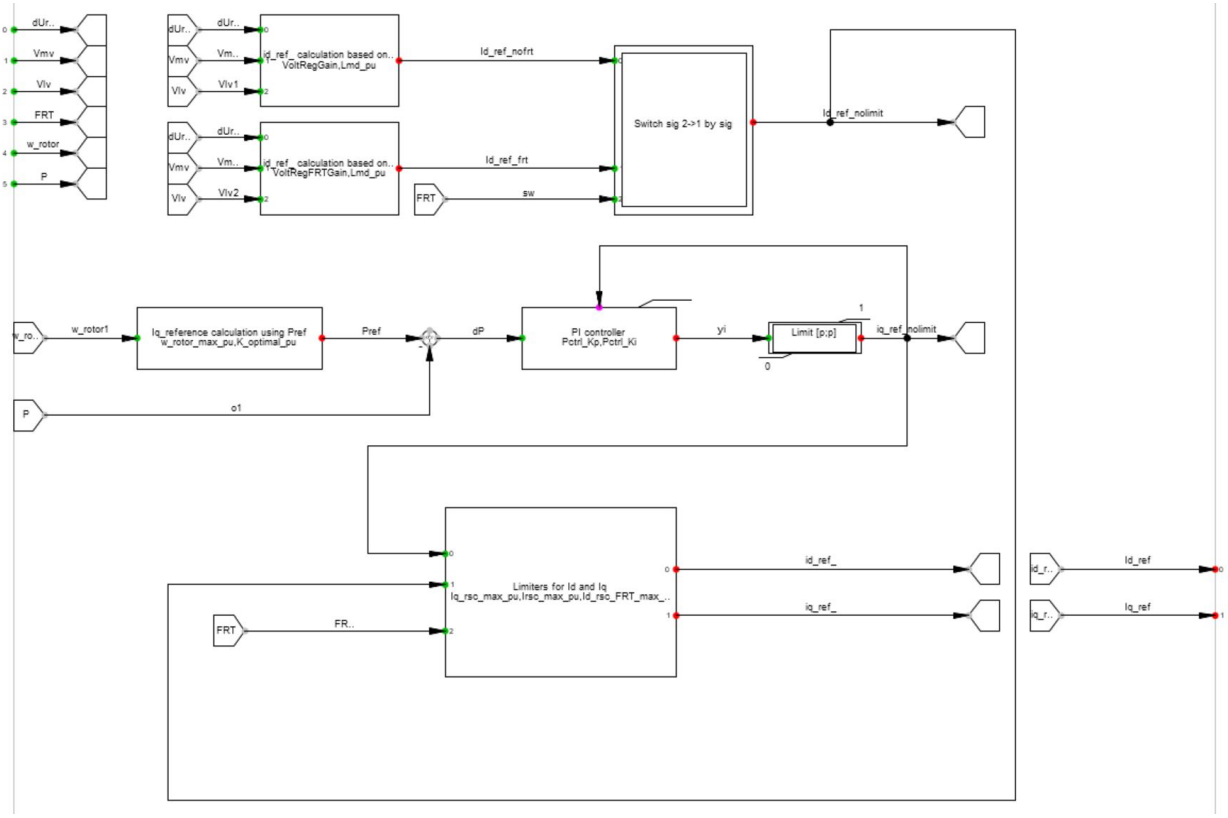

Fig. 3.18 Outer control loop in Type III WP

As discussed before, the d and q axis are swapped to accommodate the conversion from SFR to SVR. The d axis reference is now used to control power output of DFIG:

$$i_{rd}^{*} = \omega_{rm}{}^{2} K_{optimal\_pu} \tag{3.13}$$

Similarly, q axis reference is generated by FRT function and WPC's control output:

$$i^{*}_{rq} = K_{pd,rsc}(1 + \Delta U_{wpc} - v_{lv}) \tag{3.14}$$

$$i^{*}_{rq,FRT} = K_{pd,FRT}(1 - v_{lv}) \tag{3.15}$$

Reference current signals are limited by the same current limiter, which is controlled by FRT to switch current limit priority. The same inner control loop based on PI controller is constructed based on Chapter 2:

$$\begin{aligned} v_{rd}^{'} &= \frac{K_{p,rsc}}{\gamma^2}\left(i_{rd}^{'} - i_{rd}\right) + \frac{K_{i,rsc}}{\gamma^2}\int\left(i_{rd}^{'} - i_{rd}\right)\mathrm{d}t - \omega_r L_x i_{rq} \\ v_{rq}^{'} &= \frac{K_{p,rsc}}{\gamma^2}\left(i_{rq}^{'} - i_{rq}\right) + \frac{K_{i,rsc}}{\gamma^2}\int\left(i_{rq}^{'} - i_{rq}\right)\mathrm{d}t + \omega_r\left[L_{rr} i_{rd} + L_m i_{sd}\right] \end{aligned} \tag{3.16}$$

Calculated reference voltage signals are feed into PWM converter. Note that feed forward signals are moved inside the dq to abc conversion block and are not missing. The inner control loop design is shown in Fig. 3.19

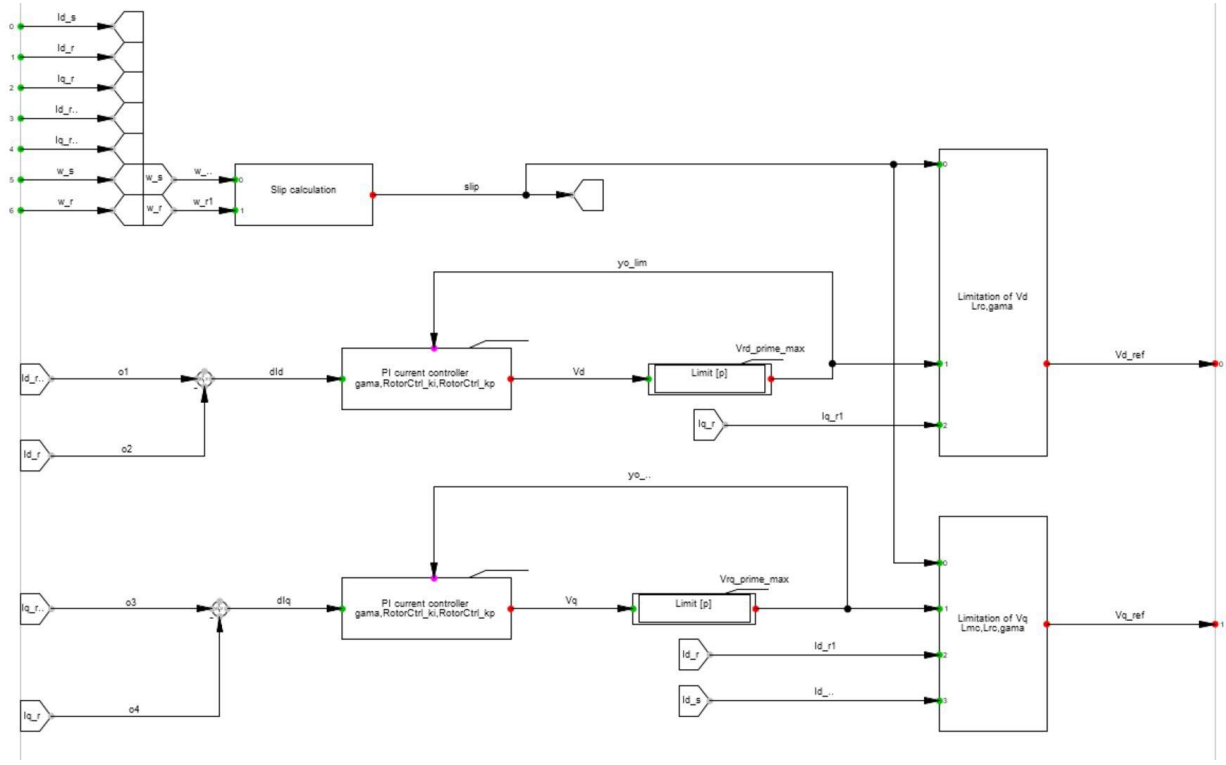

Fig. 3.19 Inner control loop of Type III WP

3.2.2 GSC controller design

The GSC controller described in Chapter 2 is constructed from scratch. It consists of filters, PLL, WPC, outer control loop and inner control loop. Same as the EMTP model, SVR reference frame is used, therefore d axis current corresponds to real power output of GSC, and q axis current corresponds to reactive power output. The structure of GSC controller is shown in Fig. 3.20:

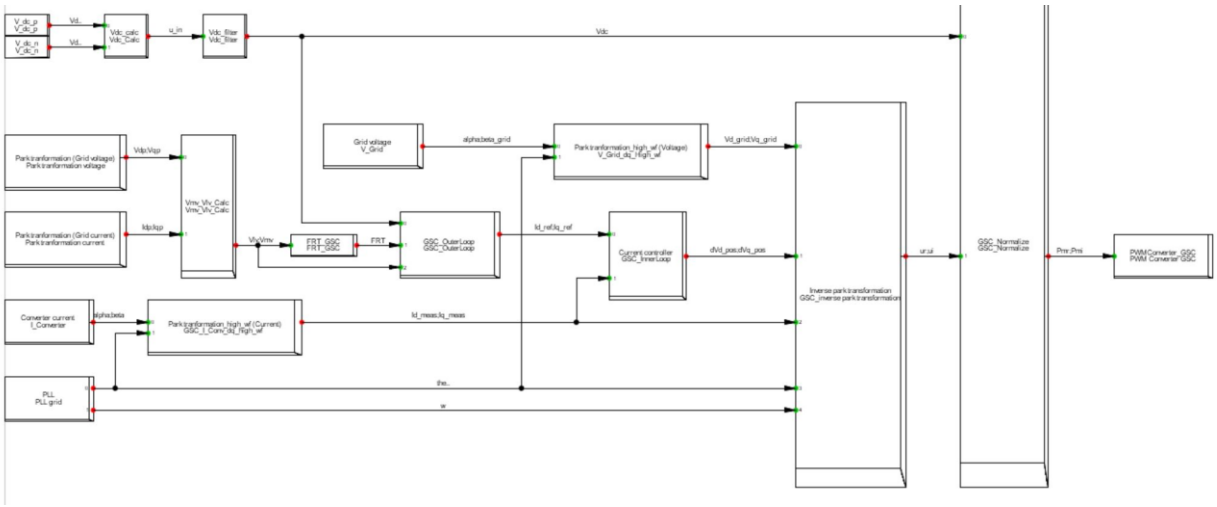

Fig. 3.20 GSC controller diagram of Type III WP

Measurement filters, PLL and dq conversion are the same as EMTP model, therefore omitted here.

The d axis outer control loop is used to control DC bus voltage:

$$i_{gd}^{*} = K_p\left(U_{DC}^{'} - U_{DC}\right) + K_i\int\left(U_{DC}^{'} - U_{DC}\right)\mathrm{d}t \tag{3.17}$$

The q axis outer control loop is used to compensate reactive current injection during FRT. The reference current is given by:

$$i_{gq}^{*} = \min\left(i_{rd}^{'} - i_{rd}, 0\right) = \min\left(I_{rd}^{\lim} - \left[\frac{v_{lv}}{\omega_s L_m} + K_{FRT}\left(1 - v_{lv}\right)\right], 0\right) \tag{3.18}$$

The outer control loop is shown in Fig. 3.21 GSC outer control loop :

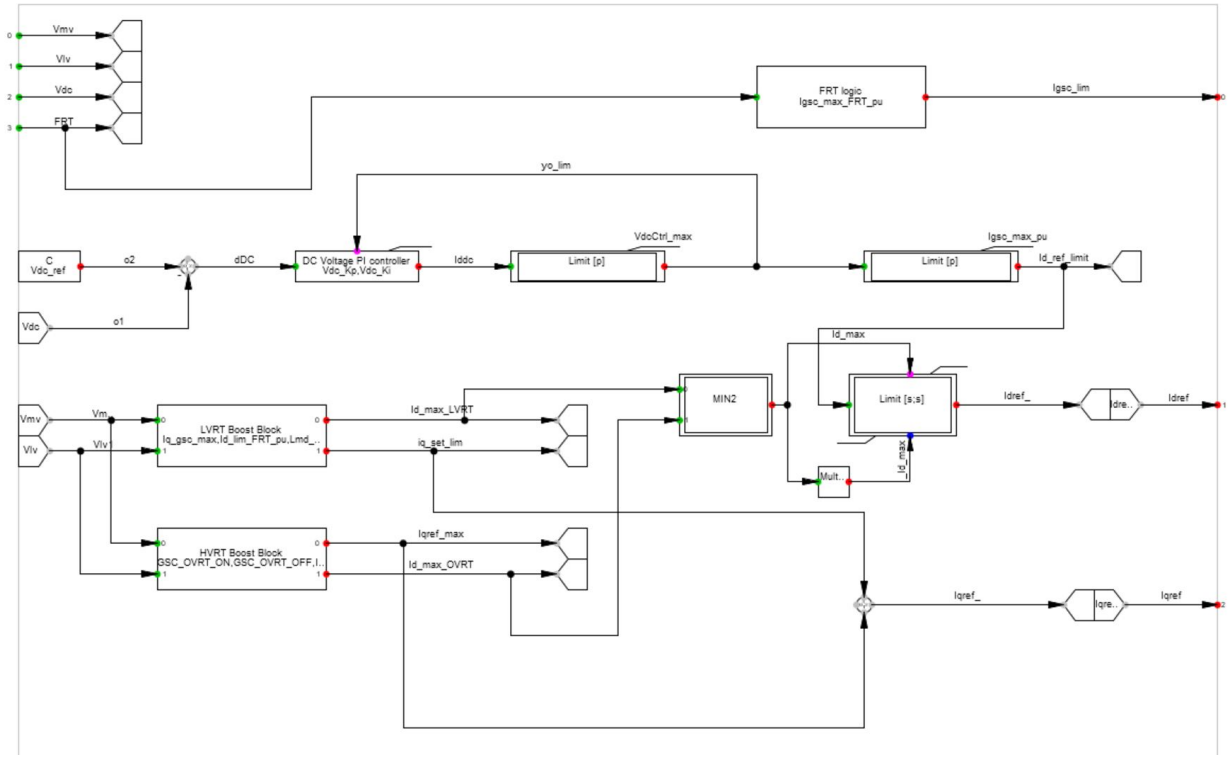

Fig. 3.21 GSC outer control loop diagram

Calculated reference currents are then passed to the inner control loop to generate reference voltage signals, equation of the inner control loop is given as:

$$\begin{aligned} v'_{cd} &= -\left[K_p\left(i'_{gd}-i_{gd}\right)+K_i\int\left(i'_{gd}-i_{gd}\right)\mathrm{d}t\right]+\omega_s L i_{gq}+v_{gd} \\ v'_{cq} &= -\left[K_p\left(i'_{gq}-i_{gq}\right)+K_i\int\left(i'_{gq}-i_{gq}\right)\mathrm{d}t\right]-\omega_s L i_{gd}+v_{gq} \end{aligned} \tag{3.19}$$

The inner control loop design is shown in Fig. 3.22:

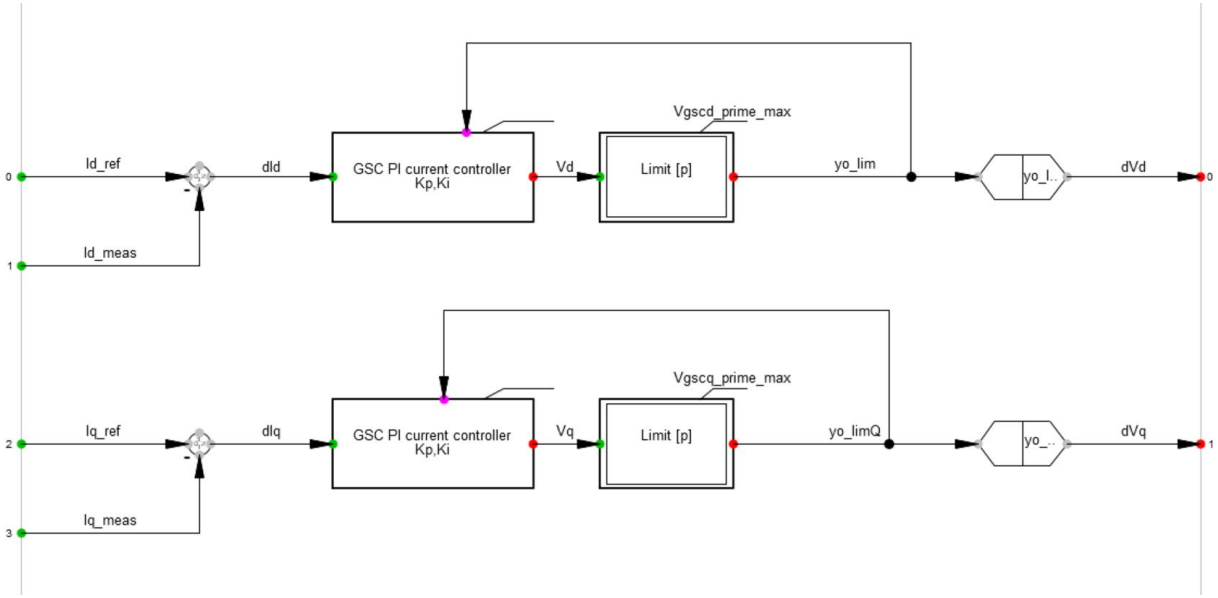

Fig. 3.22 GSC inner control loop diagram

Finally, generated reference voltage signals are normalized and passed to the PWM converter.

CHAPTER 4 RMS MODELING IN PF

As discussed before, RMS simulation has certain advantages over EMT simulation, especially when it comes to large scale power systems with IBR integration. However, due to limits of existing IBR models, especially the over simplified models based on controlled current source, error in simulation results and even system instability may occur.

4.1 RMS modeling of Type IV WP by direct mapping

The full Type IV WP model is constructed with a direct mapping method, where the controller blocks are copied from the detailed EMT model one-by-one. In this model, wind turbine model, synchronous generator, rotor side converter are all preserved and built based on the EMT model. However, due to the difference between EMT and RMS solvers, several modifications are necessary. First, measured voltage and current signals are given in RMS values instead of instantaneous values, i.e. phasors. Therefore, the dq conversion needs to be adapter to accept and transform RMS signals. The transformation is defined as:

$$\begin{bmatrix} v_d \\ v_q \end{bmatrix} = T_{dq} \begin{bmatrix} v_\alpha \\ v_\beta \end{bmatrix} \tag{4.1}$$

Where the transformation matrix T_{dq} is defined as:

$$T_{dq} = \begin{bmatrix} \cos\theta & \sin\theta \\ -\sin\theta & \cos\theta \end{bmatrix} \tag{4.2}$$

And the inverse transformation is defined as:

$$\begin{bmatrix} v_\alpha \\ v_\beta \end{bmatrix} = T_{dq}^{-1} \begin{bmatrix} v_d \\ v_q \end{bmatrix} \tag{4.3}$$

PLL is also modified to work with the RMS signals. Since measured voltage and current signals are DC RMS signals, the dq transformation essentially rotates the reference frame so that d axis aligns to positive sequence stator voltage and q axis component equals to zero.

Moreover, since RMS simulation can work with much larger time step, controller dynamics change a lot and therefore PI controller parameters, especially inner loop parameters require some tuning to achieve stable operation.

4.2 Improvement on existing voltage source-based Type IV RMS WP model

In PF, the built-in wind park model operates in controlled current source mode by default, and the injected current in controlled directly by the configured real and reactive power settings:

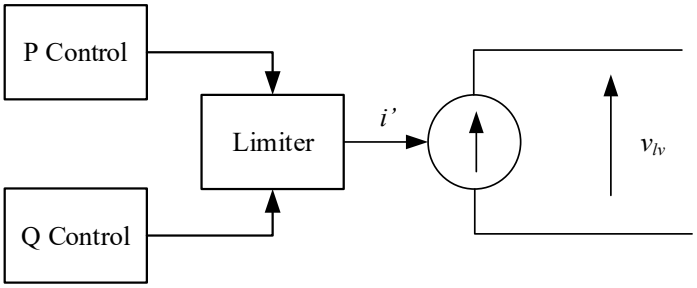

Fig. 4.1 Current source-based WP model

Apparently, the DC bus dynamics as well as inner loop controller are missing and their impacts on WP model's dynamics is not represented. The simplification in inner-loop control is made by assuming that the output current perfectly tracks the reference value and is immune to voltage disturbance. The dynamics of the current control loop, consisting of choke circuit (control plant) and inner-loop controller, in original design is given by:

$$\begin{aligned} u_{sd}^{'} &= r_s i_{sd} + K_{p,inner}\left(i_{sd}^{'} - i_{sd}\right) + K_{i,inner}\int\left(i_{sd}^{'} - i_{sd}\right)\mathrm{d}t - \omega_e L i_{sq} \\ u_{sq}^{'} &= r_s i_{sd} + K_{p,inner}\left(i_{sq}^{'} - i_{sq}\right) + K_{i,inner}\int\left(i_{sq}^{'} - i_{sq}\right)\mathrm{d}t + \omega_e (L i_{sd} + \psi_{pm}) \end{aligned} \tag{4.4}$$

The original inner control loop with the choke circuit can be represented as:

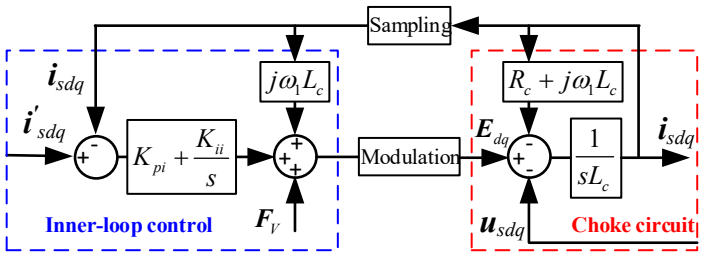

Fig. 4.2 Inner control loop and choke filter

Where *Fv* are feed forward terms for d and q axis. Neglecting delays introduced by sampling filters and PWM modulation, the output current dynamics can be depicted as a function of reference current and voltage disturbance in Laplace domain:

$$\mathbf{i}_{sdq} = \frac{1}{sL_c + R_c}[(K_{pi} + \frac{K_{ii}}{s})(\mathbf{i}'_{tdq} - \mathbf{i}_{tdq}) + \mathbf{F}_V - \mathbf{u}_{sdq}] \tag{4.5}$$

It is apparent that the choke filter dynamics can be represented with transfer function and included with the controller design. Therefore, a new inner control loop for simplified RMS model is proposed:

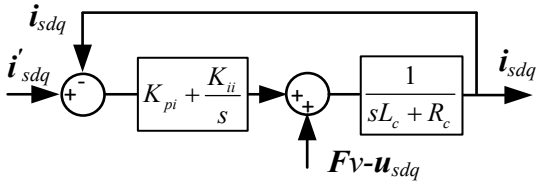

Fig. 4.3 Proposed inner control loop

The output voltage equation is given by:

$$\mathbf{E}_{dq} = \mathbf{u}_{sdq} + \frac{R_c + j\omega_1 L_c}{sL_c + R_c}[(K_{pi} + \frac{K_{ii}}{s})(\mathbf{i}'_{sdq} - \mathbf{i}_{sdq}) + \mathbf{F}_V - \mathbf{u}_{sdq}] \tag{4.6}$$

The assumption of removing dynamics of current control loop in Fig. 4.3 is only valid when the voltage feedforward is perfect ($\boldsymbol{F}_V = u_{sdq}$) and control parameters are large enough. However, in practical control design of Type-IV WTG, voltage feedforward is usually filtered or even missing. As a result of imperfect voltage feedforwards, the output current is greatly influenced by the voltage dip during fault.

Fig. 4.4 demonstrates the impact of voltage feedforward on current response of original EMTP Type-IV WP model under 40% voltage dip initiated at 2s. When the voltage feedforward is perfect ($\boldsymbol{F}_V = u_{sdq}$), output current can reach reference value instantly as shown in Fig. 4.4 (a), which means the simplification under this situation is valid. In contrast, when a regular low-pass filter ($\boldsymbol{F}_V = u_{sdq}/(1+0.001s)$) is added in the voltage feedforward, output current clearly overshoots before reaching reference value, which makes previous assumption invalid. When the voltage feedforward is removed, output current shows larger transient in the first few cycles following the voltage dip, as shown in Fig. 4.4 (c).

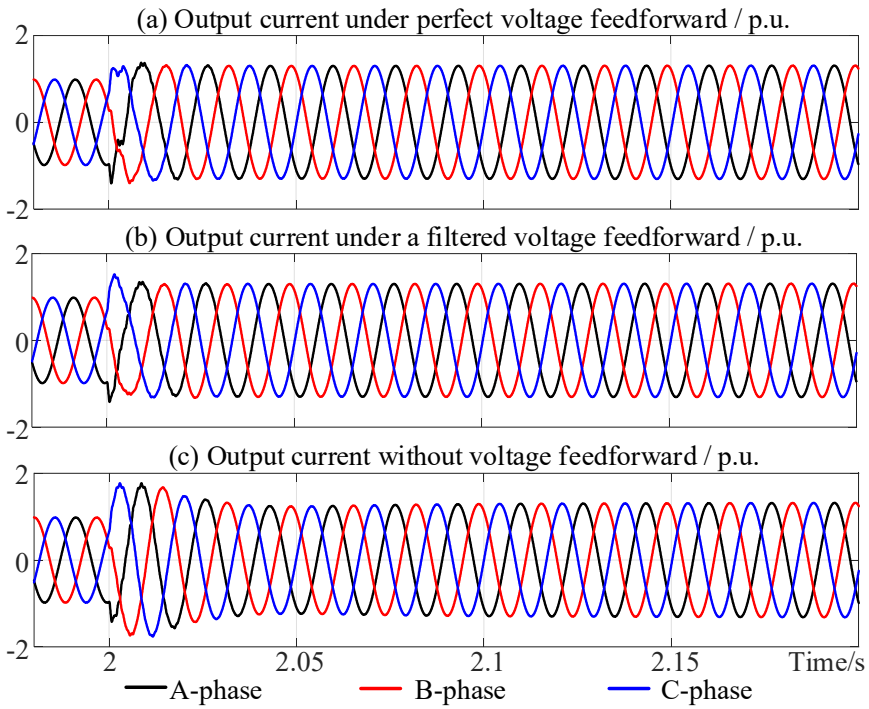

Fig. 4.4 Transient response with different voltage feedforwards

As shown in section □, the DC bus voltage can be written as a function of GSC power output:

$$U_{DC} = \frac{1}{C_{DC}} \int \frac{P_{GSC}^{'} - P_{GSC}}{U_{DC}} \mathrm{d}t \tag{4.7}$$

Where C_{DC} is DC bus capacitor's capacitance, P_{GSC} is GSC's output power, U_{DC} is DC bus voltage. GSC power is calculated by:

$$P = \frac{3}{2}(u_{sd} i_{sd} + u_{sq} i_{sq}) \tag{4.8}$$

Combining the proposed choke filter model, and the emulation of the DC bus with capacitor, the following controller can be constructed:

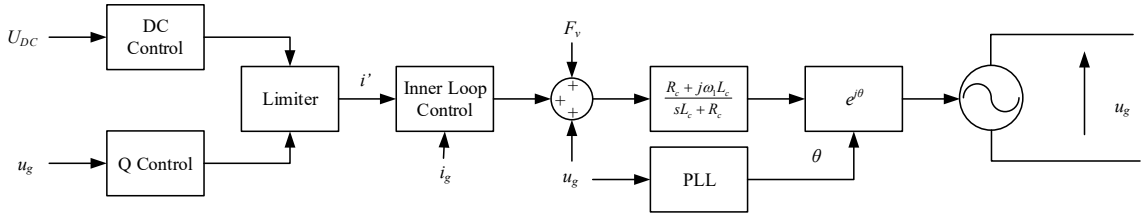

Fig. 4.5 Proposed voltage source-based Type IV WP controller

With the introduction of choke filter circuit, the inner control loop is also re-introduced. Therefore, the proposed RMS model has similar structure as the original EMT model, hence same parameters can be used. Following picture shows the added choke filter and feed forward signal calculation block.

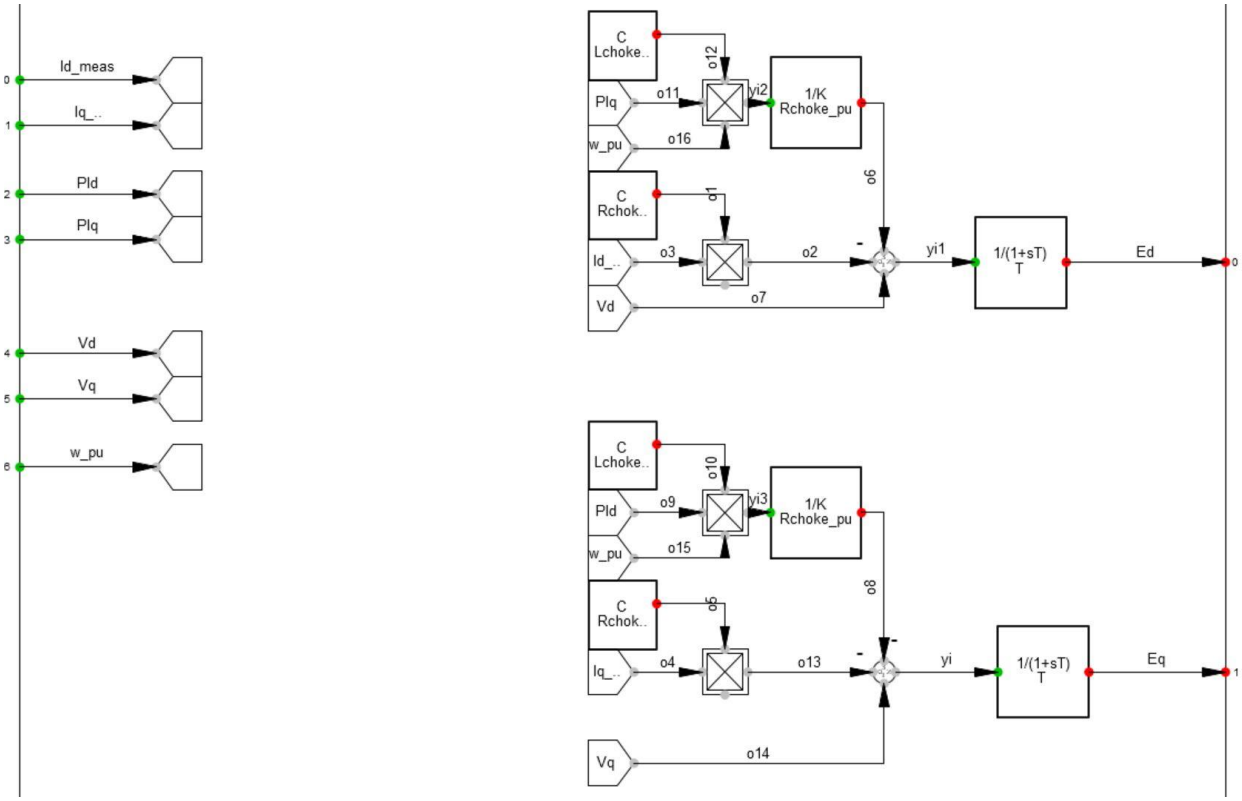

Fig. 4.6 Inner control loop with voltage feedforward

4.3 RMS modeling of DFIG WP

The RMS model of DFIG WP is built with internal voltage source model. For the stator winding of the DFIG, the internal voltage is defined in by

$$\mathbf{E}_s^{\alpha\beta} = \frac{L_m}{L_r}\frac{\mathrm{d}\boldsymbol{\psi}_r^{\alpha\beta}}{\mathrm{d}t} \tag{4.9}$$

By substituting (4.9) into (2.63), the DFIG stator variables can be written as

$$\mathbf{U}_s^{\alpha\beta} = R_s\mathbf{I}_s^{\alpha\beta} + \sigma L_s\frac{\mathrm{d}\mathbf{I}_s^{\alpha\beta}}{\mathrm{d}t} + \mathbf{E}_s^{\alpha\beta} \tag{4.10}$$

This indicates that, by using the internal voltage, the DFIG can be represented by a rotor flux linkage-controlled voltage source (stator internal voltage) behind a resistor–inductor (RL) circuit. By further substituting (4.10) into (2.69), the rotor flux linkage can be represented by rotor voltage and stator variables as

$$\frac{\mathrm{d}\boldsymbol{\psi}_r^{dqr}}{\mathrm{d}t} = \mathbf{U}_r^{dqr} + \frac{L_m \mathbf{I}_s^{dqr}}{\tau_r} - \frac{\boldsymbol{\psi}_r^{dqr}}{\tau_r} \tag{4.11}$$

$$\tau_r = L_r / R_r \tag{4.12}$$

The rotor voltage is generated by the RSC control as described in DFIG modelling. Above circuit and control equations can be combined by transforming these vectors into the dq synchronous reference frame (denoted by dq) corresponding to the voltage of the slack bus by

$$\begin{aligned} \mathbf{X}^{\alpha\beta} &= \mathbf{X}^{dq} e^{j\omega_1 t} \\ \mathbf{X}^{dqr} &= \mathbf{X}^{dq} e^{j\omega_s t} \\ \mathbf{X}^{PLL} &= \mathbf{X}^{dq} e^{-j\Delta\theta_{PLL}} \end{aligned} \tag{4.13}$$

where

$$\Delta\theta_{PLL} = \theta_{PLL} - \omega_1 t \tag{4.14}$$

And the reorganized DFIG equations become

$$\mathbf{U}_s^{dq} - \mathbf{E}_s^{dq} = (R_s + j\omega_1 \sigma L_s)\mathbf{I}_s^{dq} + \sigma L_s \frac{\mathrm{d}\mathbf{I}_s^{dq}}{\mathrm{d}t} \tag{4.15}$$

$$\mathbf{E}_s^{dq} = j\omega_1 \frac{L_m}{L_r} \boldsymbol{\psi}_r^{dq} + \frac{L_m}{L_r} \frac{\mathrm{d}\boldsymbol{\psi}_r^{dq}}{\mathrm{d}t} \tag{4.16}$$

By substituting (4.16) into (4.11), the dynamic of rotor flux linkage is obtained as

$$\frac{\mathrm{d}\boldsymbol{\psi}_r^{dq}}{\mathrm{d}t} = \mathbf{P}\mathbf{I}_{RSC}^{PLL} e^{j\Delta\theta_{PLL}} \tag{4.17}$$

Applying Laplace transform, the stator current is expressed as

$$\mathbf{I}_s^{dq} \approx \frac{\mathbf{U}_s^{dq} - j\omega_1 \dfrac{L_m}{L_r} \dfrac{\mathbf{P}\mathbf{I}_{RSC}^{PLL} e^{j\Delta\theta_{PLL}}}{s}}{R_s + (j\omega_1 + s)\sigma L_s} \tag{4.18}$$

For the choke filter and GSC control, by applying the same dq transformation, the reorganized equations can be obtained as

$$\mathbf{U}_s^{dq} - \mathbf{E}_l^{dq} = (R_l + j\omega_1 L_l)\mathbf{I}_l^{dq} + L_l \frac{\mathrm{d}\mathbf{I}_l^{dq}}{\mathrm{d}t} \tag{4.19}$$

$$\mathbf{E}_l^{dq} = \mathbf{U}_s^{dq} - j\omega_1 L_l \mathbf{I}_l^{dq} - \mathbf{PI}_{GSC}^{PLL} e^{j\Delta\theta_{PLL}} \tag{4.20}$$

By substituting (4.20) into (4.18), the dynamic of GSC current is obtained as

$$\frac{\mathrm{d}\mathbf{I}_l^{dq}}{\mathrm{d}t} = -\frac{R_l}{L_l}\mathbf{I}_l^{dq} + \frac{\mathbf{PI}_{GSC}^{PLL} e^{j\Delta\theta_{PLL}}}{L_l} \tag{4.21}$$

With Laplace transformation, the GSC current is expressed as

$$\mathbf{I}_l^{dq} = \frac{\mathbf{PI}_{GSC}^{PLL} e^{j\Delta\theta_{PLL}}}{sL_l + R_l} \tag{4.22}$$

In PF and other RMS simulation tools, fundamental-frequency components are the focus, and they are represented with phasors (denoted by dot superscript in this paper) with respective to the phase angle of the selected slack bus. Therefore, the real and imaginary parts (also the magnitude and phase angle) of these phasors are constant in dq reference frame during steady state. Therefore, the differential terms in circuit equations are removed and the network is replaced by impedance-based algebraic matrix.

The phasor-based expressions for the stator winding of DFIG can be written as

$$\dot{U}_s^{dq} - \dot{E}_s^{dq} = (R_s + j\omega_1 \sigma L_s)\dot{I}_s^{dq} \tag{4.23}$$

Similarly, the phasor-based expressions for the choke filter can be obtained as

$$\dot{U}_s^{dq} - \dot{E}_l^{dq} = (R_l + j\omega_1 L_l)\dot{I}_l^{dq} \tag{4.24}$$

Since the control plants (DFIG and choke filter) are simplified in RMS simulations, the controllers need to be modified accordingly to achieve similar dynamic responses in EMT simulations. Thus, the objective of the RMS modeling in this paper is to reconstruct the control branches behind internal voltage of stator winding and GSC to emulate the original dynamics of DFIG-based WPs in EMT simulations.

First, to mimic the complete dynamic of stator current in (4.24), the internal voltage phasor of the DFIG stator is reconstructed according to (4.22) as

$$\dot{E}_s^{dq} = j\omega_1 \frac{L_m}{L_r}\dot{\psi}_r^{dq} = j\omega_1 \frac{L_m}{L_r}\frac{\mathbf{PI}_{RSC}^{PLL} e^{j\Delta\theta_{PLL}}}{s} \tag{4.25}$$

According to (4.22), the rotor current can be replaced by stator current and rotor flux linkage by

$$\dot{I}_r^{PLL} = \frac{\dot{\psi}_r^{PLL}}{L_r} - \frac{L_m}{L_r}\dot{I}_s^{PLL} \tag{4.26}$$

To mimic the complete dynamic of GSC current, the internal voltage phasor of the DFIG stator is reconstructed as

$$\dot{E}_l^{dq} = \dot{U}_s^{dq} - \frac{R_l + j\omega_1 L_l}{R_l + sL_l}\mathbf{PI}_{GSC}^{PLL} e^{j\Delta\theta_{PLL}} \tag{4.27}$$

Second, since the input signals of stator voltage in RMS simulation tools are the real and imaginary parts of the phasor, the equations of the PLL for RMS simulations can still be modeled with (4.27) , but the error is changed to

$$U_{sq}^{PLL} = \mathrm{Im}(\dot{U}_s^{dq} e^{-j\Delta\theta_{PLL}}) \tag{4.28}$$

For calculating the DC voltage dynamic, the rotor voltage in (4.25) can be replaced by

$$\dot{U}_r^{dq} = R_r \dot{I}_r^{dq} + \mathbf{PI}_{RSC}^{PLL} e^{j\Delta\theta_{PLL}} + j\omega_s \dot{\psi}_r^{dq} \tag{4.29}$$

Based on above phasor-based expressions, the RMS model proposed in this paper is illustrated in Fig. 4.7.

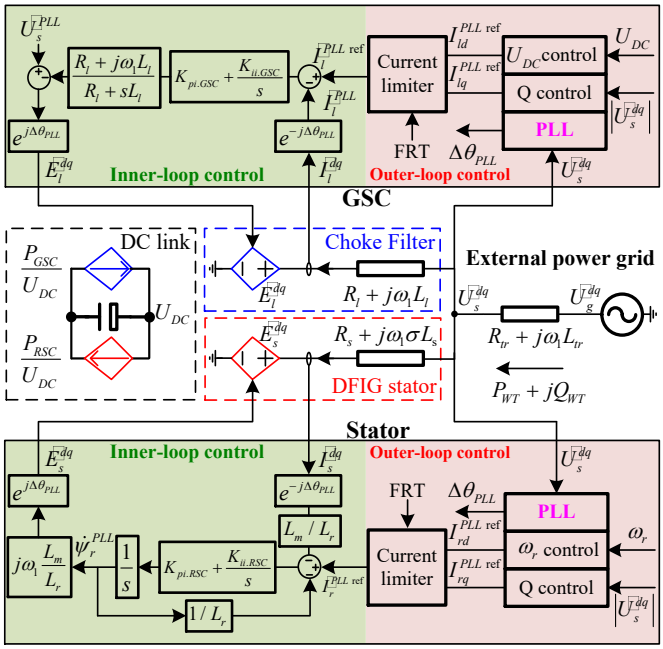

Fig. 4.7 Proposed controller for Type III RMS model

Compared with the current source-based RMS models, the proposed model is built on internal voltage and their equivalent circuits. The advantages are summarized as follows:

(1) The responses of the DFIG's stator winding and GSC are both emulated. Moreover, the coupling between two responses through DC bus is also emulated. These measures are expected to improve the accuracy of the RMS simulations.

(2) The dynamics of the inner-loop control of RSC and GSC are emulated in the proposed RMS model. Compared with the existing RMS models assuming the current reference can be tracked perfectly, the internal voltage-based RMS model is expected to accurately represent the high-frequency interactions with other WPs and converters. Moreover, the voltage source interface is also expected to reduce the risk of numerical oscillations.

(3) It is worth noting that rotor variables, including rotor angle and rotor phase currents, are shielded in the proposed RMS model and signal received by branches underneath stator internal voltage model is stator currents. Therefore, the DFIG dynamics could be emulated in a similar way as GSC. Apart from these rotor variables, state variables in the stator and GSC sides can be easily initialized as shown in following part. This is also expected to improve the efficiency of RMS simulations.

In project-specific studies, all state variables inside DFIG-based WPs need to be initialized using given operation point in certain scenarios. This can be achieved by executing EMT and RMS simulations in zero-state responses. However, this is time-consuming because zero-state responses may require minutes to converge or could be unstable in stringent cases for transient stability studies. Therefore, an adopted approach in existing simulation tools is to calculate steady-state values of state variables with results obtained from power flow studies.

For DFIG-based WP, the proposed RMS model is typically specified as a PQ or PU node in the network. The power-flow calculation will provide active and reactive power (PWT0 and QWT0) and stator voltage phasor ($\dot{U}_{s0}^{dq}$) with respect to the slack bus. The subscript 0 stands for the pre-fault initial value. According to power-flow results, the initialization is calculated as follows.

(1) According to wind turbine (WT) aerodynamics and parameters, the initial rotor speed ωr0 can be solved by substituting PWT0 into power coefficient curves.

(2) According to ωr0, the initial active power PWT0 is inherently allocated into stator (Ps0) and GSC (Pl0) as

$$P_{s0} = \frac{\omega_1}{\omega_{r0}} P_{WT0} \tag{4.30}$$

$$P_{l0} = \frac{\omega_{r0} - \omega_1}{\omega_{r0}} P_{WT0} \tag{4.31}$$

(3) Since the reactive power is mainly contributed by the DFIG stator, the initial stator current phasor can be calculated as

$$\dot{I}_{s0}^{dq} = (P_{s0} + jQ_{WT0}) / \dot{U}_{s0}^{dq} \tag{4.32}$$

Similarly, the initial GSC current phasor is determined as

$$\dot{I}_{l0}^{dq} = (P_{l0} + j0) / \dot{U}_{s0}^{dq} \tag{4.33}$$

(4) The initial rotor flux linkage phasor is calculated as

$$\dot{\psi}_{r0}^{dq} = \frac{L_r}{L_m} \frac{\dot{U}_{s0}^{dq} - (R_s + j\omega_1 \sigma L_s)\dot{I}_{s0}^{dq}}{j\omega_1} \tag{4.34}$$

(5) The initial values of the inner-loop, outer-loop and PLL controllers stand for the errors accumulated and thus should be set to zero.

In existing DFIG-based WP models, more calculations and coordinate transformations need to be calculated to determine and initialize the rotor variables.

CHAPTER 5 MODEL VERIFICATION

In this section, the proposed EMT and RMS models are benchmarked in the standard EPRI benchmark network:

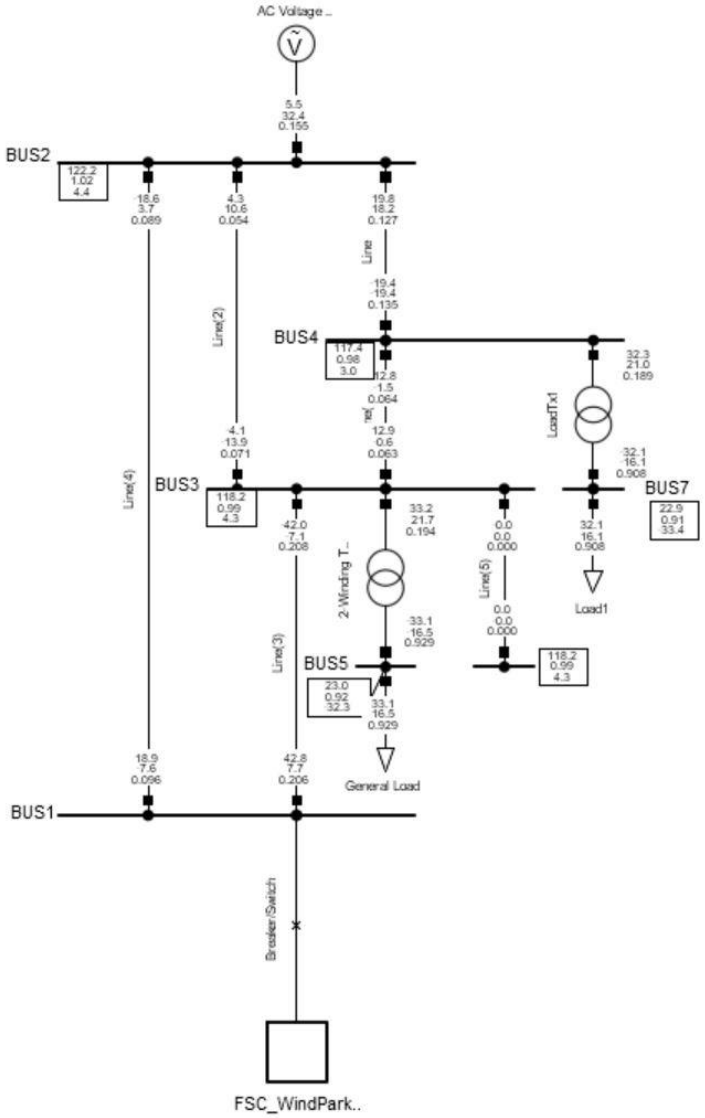

Fig. 5.1 EPRI Benchmark System

Where the wind park is connected to a 120KV system, the system consists of 4 HV buses and 2 LV buses, interconnected by transmission lines of various lengths and transformers. 2 constant loads are connected on LV buses. The system is connected to an external network on the other side, which is represented by a voltage source behind impedance.

5.1 Type IV EMT Model

A single phase to ground fault is applied at bus 5 at t=1s. The real and reactive power output of the wind park is monitored and plotted in the following diagram:

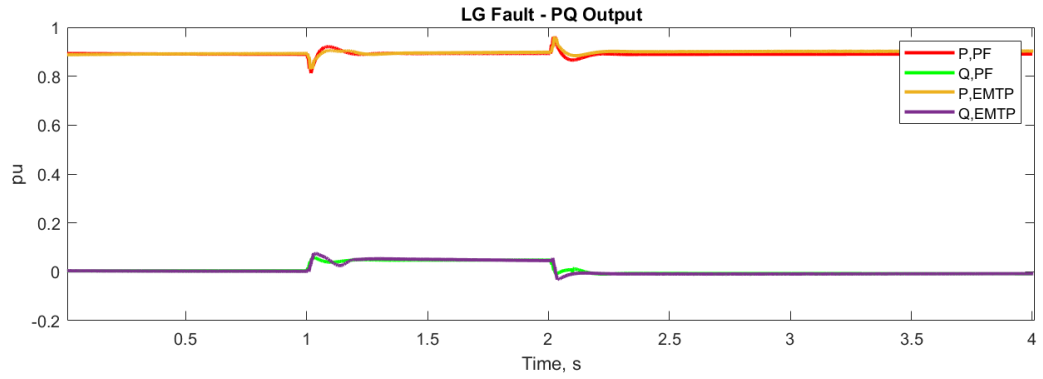

Fig. 5.2 PQ output of Type IV EMT models

Voltage measured at POI is also plotted:

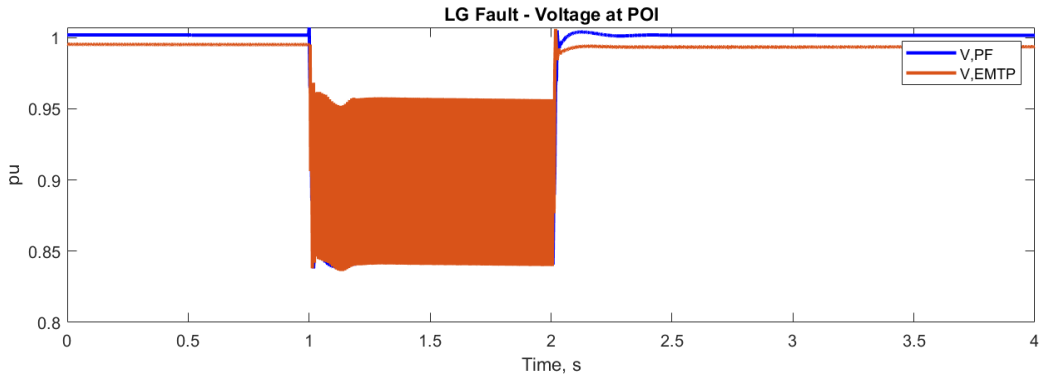

Fig. 5.3 Voltage at POI of Type IV EMT models

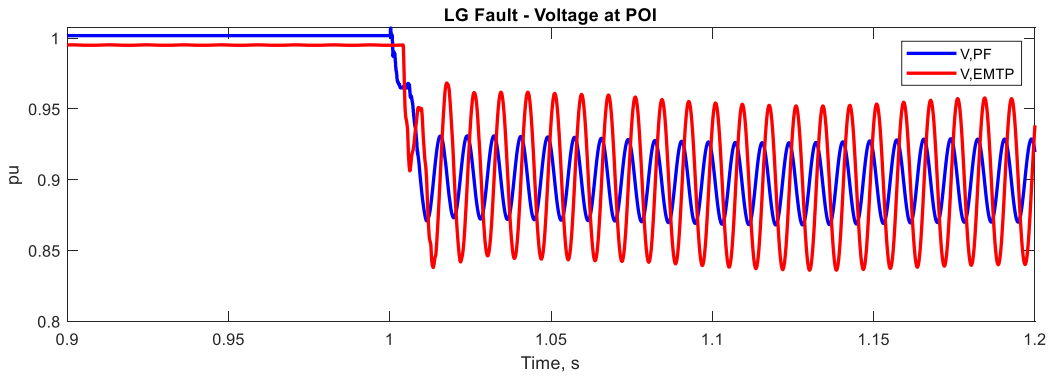

Fig. 5.4 Voltage at POI of Type IV EMT models during initial transient

As shown in Fig. 5.3 and Fig. 5.4, the PF model's real and reactive power output in steady state and during fault are very close to an identical model in a different EMT tool. The voltage at POI is also very close, and the double frequency oscillation is visible in both models due to the unbalanced nature of the fault.

Consider the inner control loop of GSC, the reference and measured current signals are plotted in the following diagram:

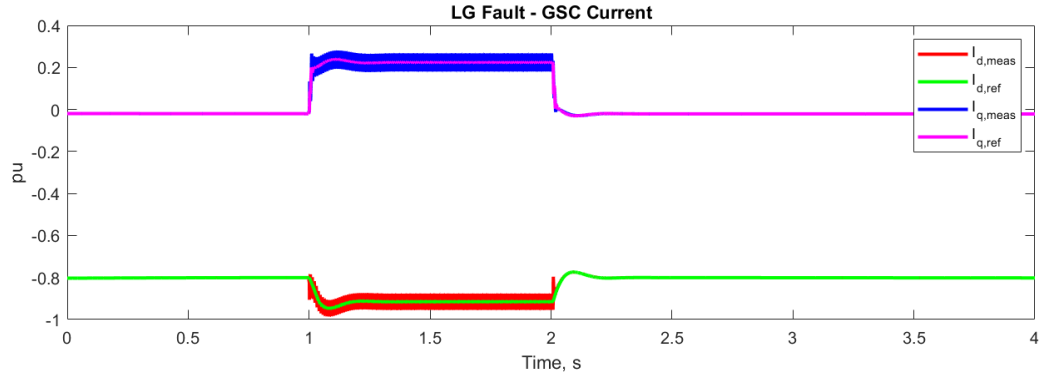

Fig. 5.5 GSC current

Which shows perfect tracking of the PI controller on both d and q axis current signals. Since the fault is unbalanced, double frequency oscillations can be observed on both current signals. The PI controller output is shown in following plot:

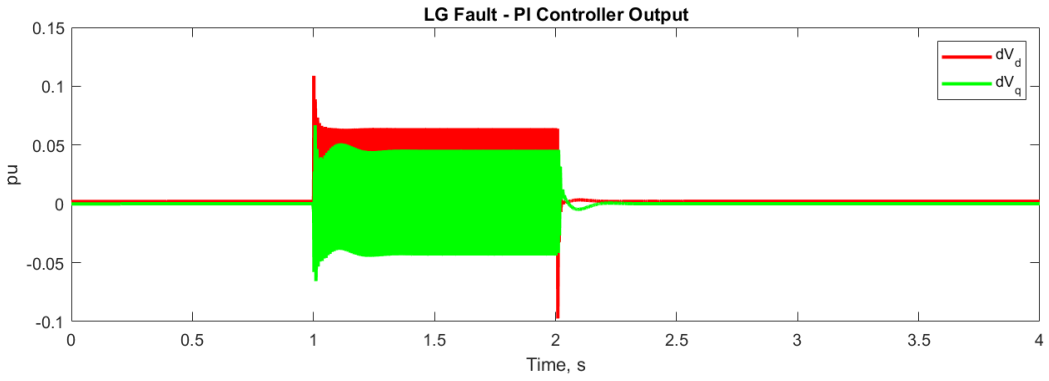

Fig. 5.6 PI controller output

In steady state, both PI controllers' output are close to zero, which means the feed forward terms are correct. MSC current signals are shown in following plot:

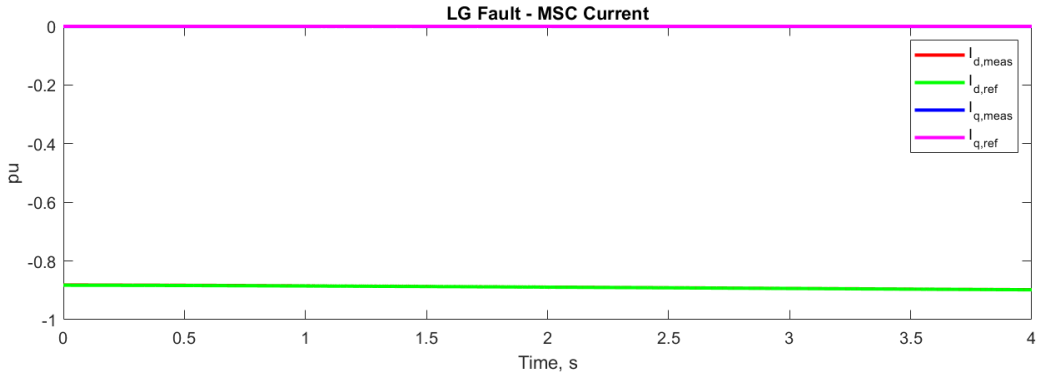

Fig. 5.7 MSC current

Which again shows perfect tracking of the PI controller. Since the synchronous machine is decoupled from the grid with the DC bus, fault on the grid side has little impact on MSC's output current. Finally, the DC bus voltage is shown in following plot:

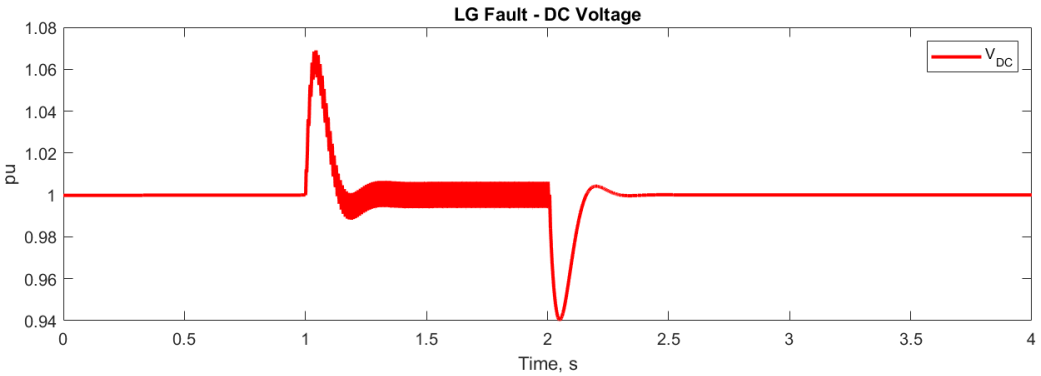

Fig. 5.8 DC voltage measurement

DC bus is controlled at 1 pu all the time, which again shows perfect tracking of the PI controller. Chopper is not activated since POI voltage is still around 1 pu and GSC can output rated power without any issue.

Now consider a more severe three phase to ground fault applied to bus 3 at t=1s. The measured real and reactive power output is shown in following plot:

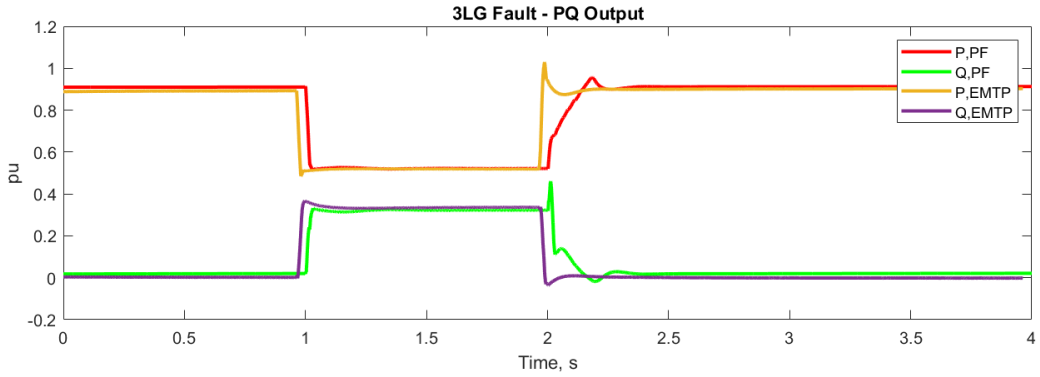

Fig. 5.9 PQ output of Type IV EMT models

As shown in the plot, real power output dips to around 0.5 p.u, and both models have very close output. GSC current is shown in following plot:

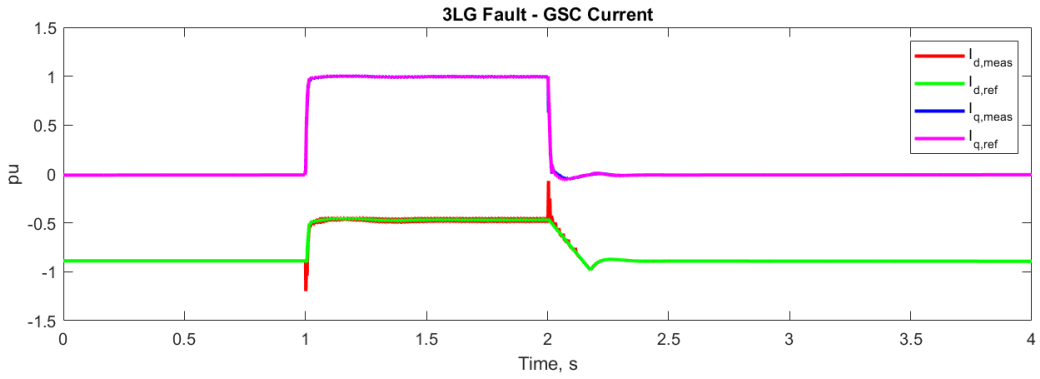

Fig. 5.10 GSC current

Apparently, the active current output during fault is limited to only around 0.5 p.u. and priority is shifted to reactive current output to support voltage. After fault is cleared, priority is given back to active current to output power to the grid, meanwhile reactive power drops down to around zero since reactive power setpoint is zero. Again, PI controller tracks the reference signal perfectly the

whole time, showing the PF model's accuracy to the original model. The MSC controller's current is shown in following plot, which also shows perfect tracking of the PI controller.

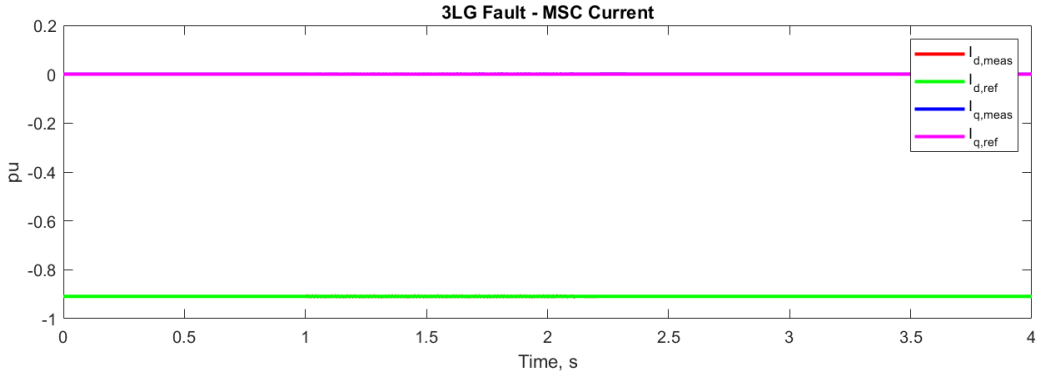

Fig. 5.11 MSC current

POI voltage drops down to around 0.3 pu during fault, therefore FRT is activated. After fault is cleared, FRT signal is reset and current limiter priority is given back to d axis active current.

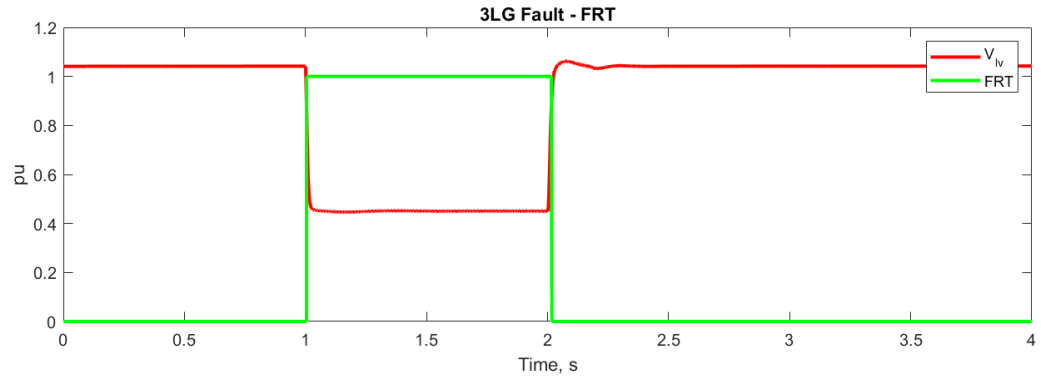

Fig. 5.12 FRT output

Finally, DC bus voltage is shown in following plot. Since current limiter priority is given to q axis during fault, real power output of GSC is limited. Since wind turbine and MSC are still injecting the same amount of real power as prefault condition, voltage on DC bus will rise and may cause damage. Therefore, DC bus chopper will be activated once DC bus voltage increases to a predefined value, and excessive power will be dissipated by the chopper resistor.

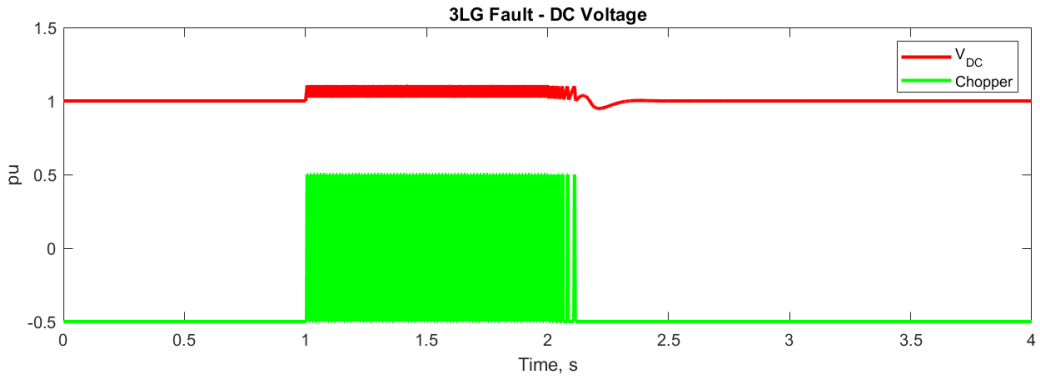

Fig. 5.13 DC bus voltage and chopper signal

5.2 Type III EMT Model

A single phase to ground fault is applied at bus 3 at t=1s. The real and reactive power output of the wind park is monitored and plotted in the following diagram:

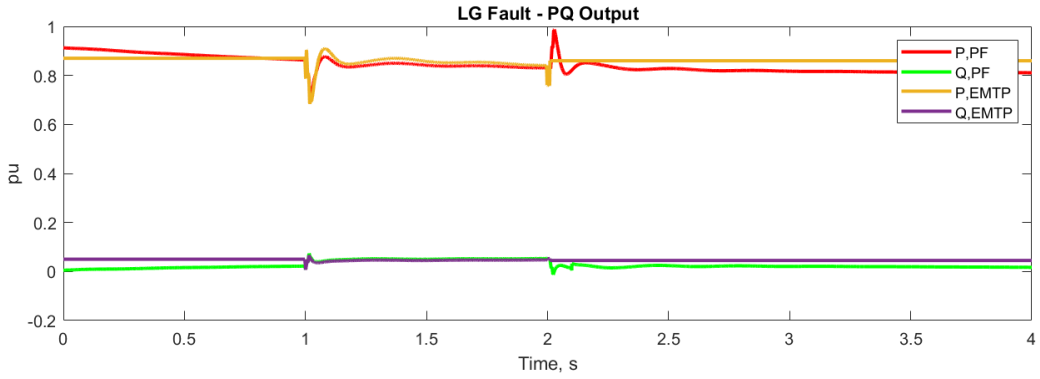

Fig. 5.14 PQ output

Voltage measured at POI is also plotted:

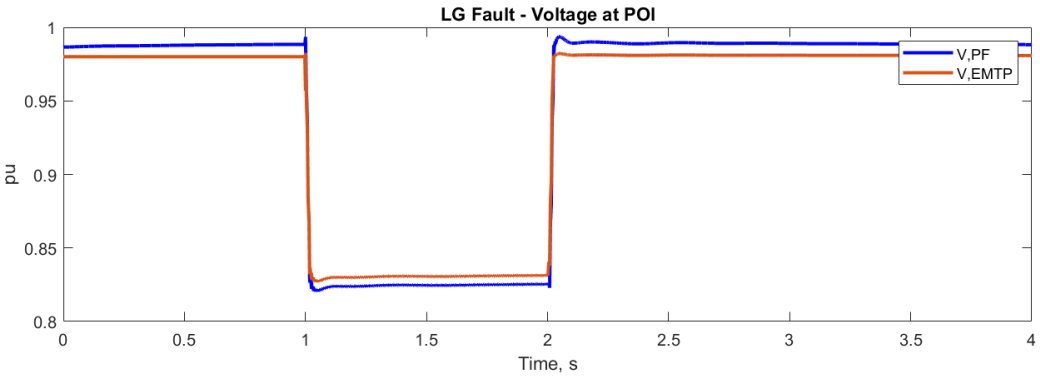

Fig. 5.15 POI voltage measurement

As shown in the diagram, the PF model's real and reactive power output in steady state and during fault are very close to the EMT model in a different EMT tool. The voltage at POI is also very close.

Consider the inner control loop of GSC, the reference and measured current signals are plotted in the following diagram:

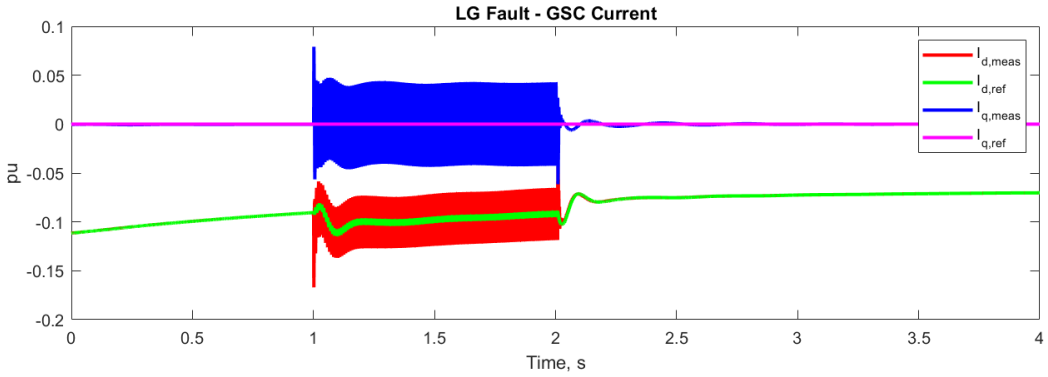

Fig. 5.16 GSC current

Which shows perfect tracking of the PI controller on both d and q axis current signals. RSC current signals are shown in following plot:

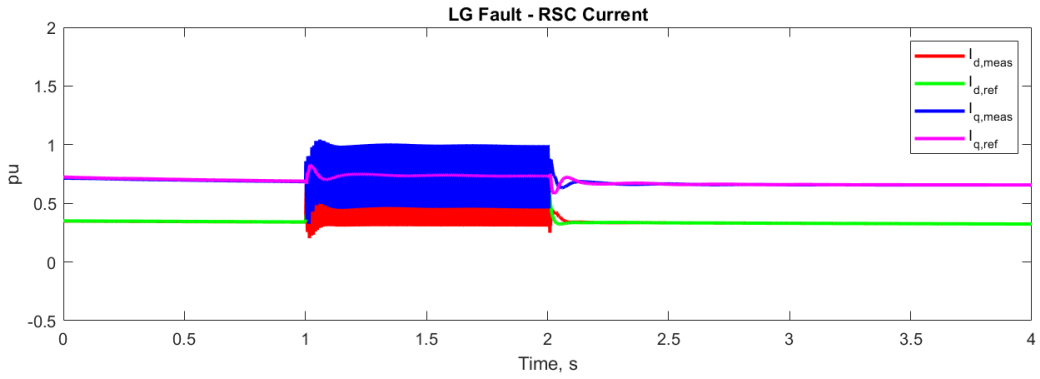

Fig. 5.17 RSC current

Which again shows perfect tracking of the PI controller. Unlike Type IV WTG, DFIG stator is connected directly to the grid, therefore fault current's impact on the DFIG is reflected on the rotor current signals. Finally, the DC bus voltage is shown in following plot:

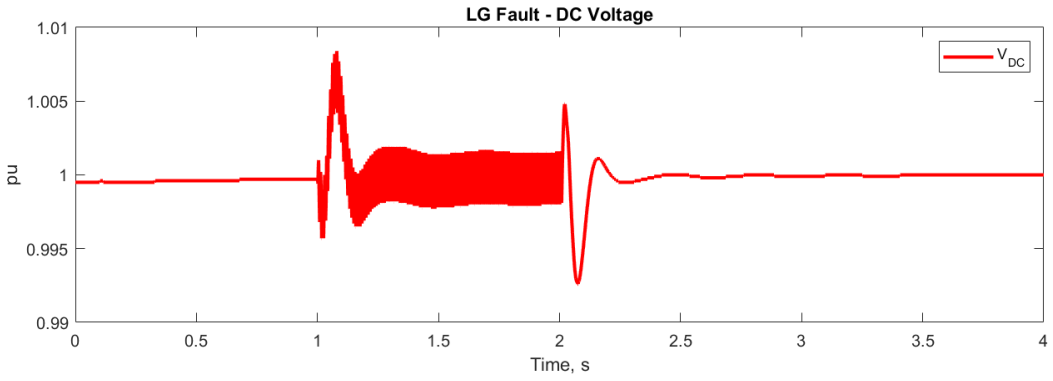

Fig. 5.18 DC bus voltage

DC bus is controlled at 1 pu all the time, which again shows perfect tracking of the PI controller. Chopper is activated during the fault when DC bus voltage rises to the defined threshold.

5.3 Type IV RMS Model - Full

A 3 phase to ground fault is applied at bus 3 at t=1s. The real and reactive power output of the wind park, as well as voltage at POI are plotted in the following diagram:

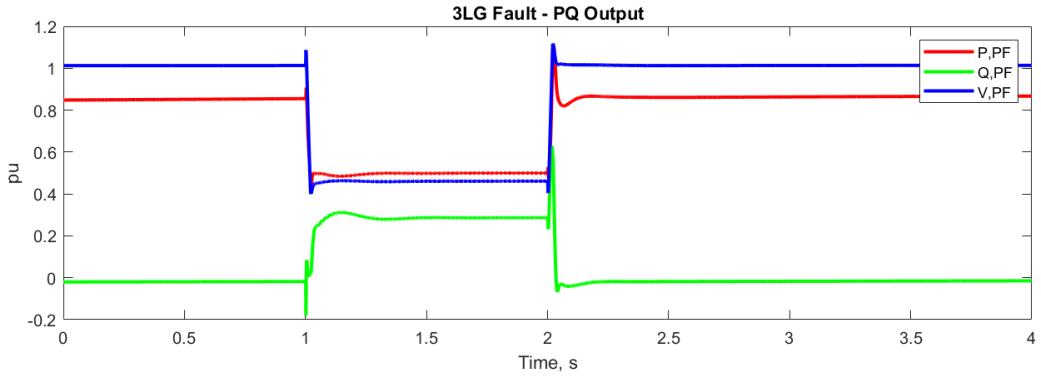

Fig. 5.19 PQ output at POI

As shown in the diagram, the RMS model's real and reactive power output in steady state and during fault are very close to the EMT model. The voltage at POI is also very close.

Consider the inner control loop of GSC, the reference and measured current signals are plotted in the following diagram:

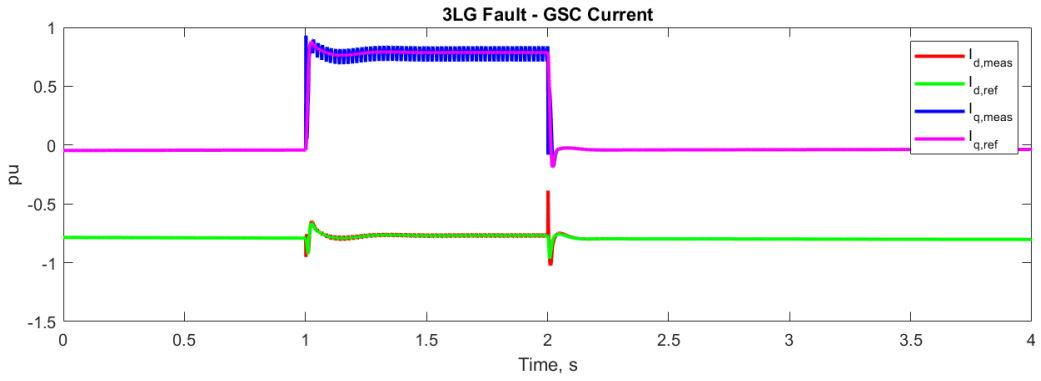

Fig. 5.20 GSC current

Which shows perfect tracking of the PI controller on both d and q axis current signals. MSC current signals are shown in following plot:

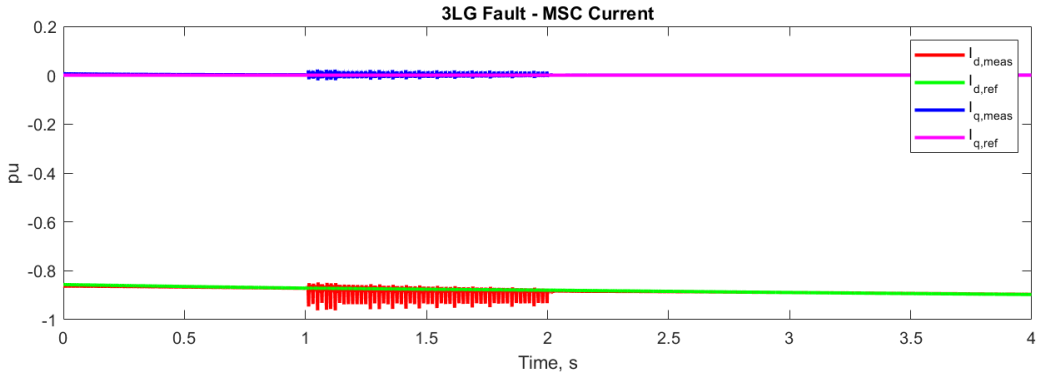

Fig. 5.21 MSC current

Which again shows good tracking of the PI controller. Finally, the DC bus voltage is shown in following plot:

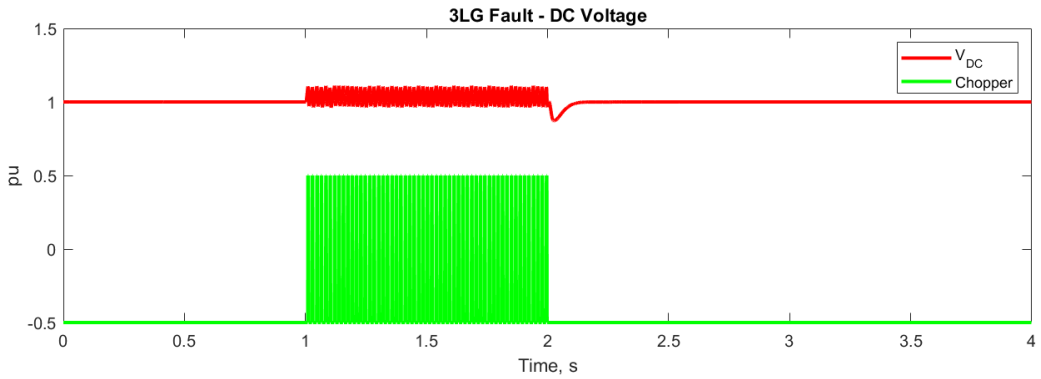

Fig. 5.22 DC bus voltage and chopper signal

DC bus is controlled at 1 pu all the time, which shows good tracking of the PI controller. Chopper is activated during the fault when DC bus voltage rises to the defined threshold.

5.4 Type III RMS Model

The same single phase to ground fault is applied at bus 3 at t=1s. The real and reactive power output of the wind park and voltage at POI are plotted in the following diagram:

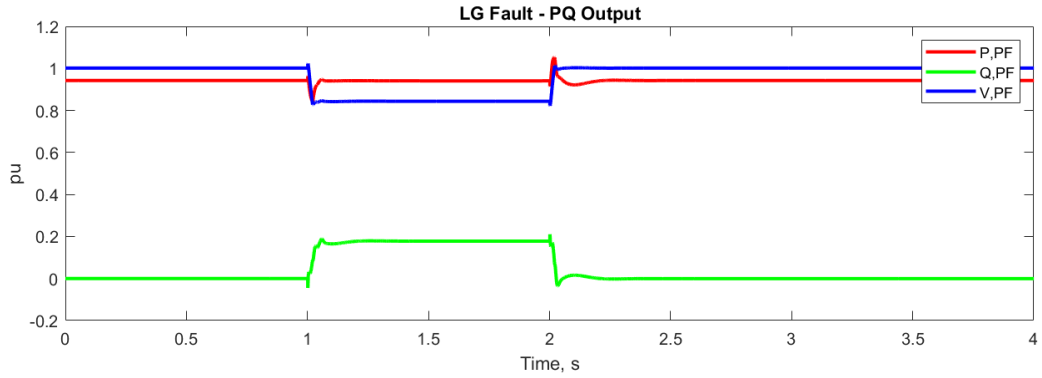

Fig. 5.23 PQ output at POI

As shown in the diagram, the PF model's real and reactive power output in steady state and during fault are very close to the original model. The voltage at POI is also very close.

Consider the inner control loop of GSC, the reference and measured current signals are plotted in the following diagram:

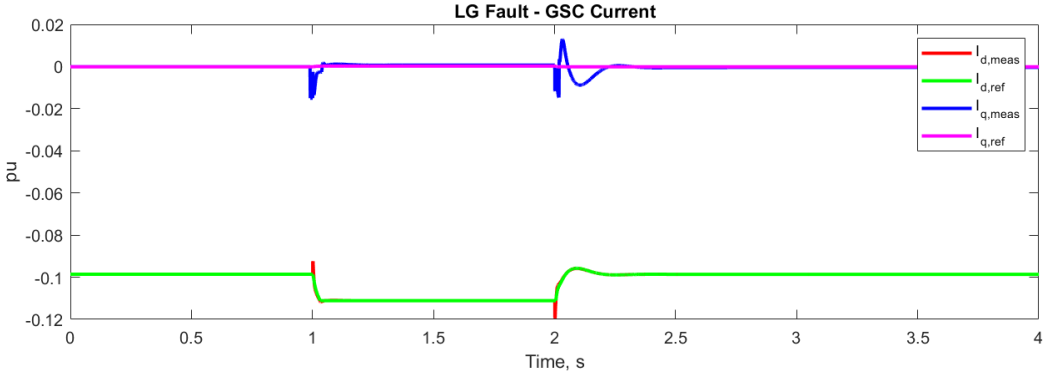

Fig. 5.24 GSC current

Which shows perfect tracking of the PI controller on both d and q axis current signals.

Finally, the DC bus voltage is shown in Fig. 5.25:

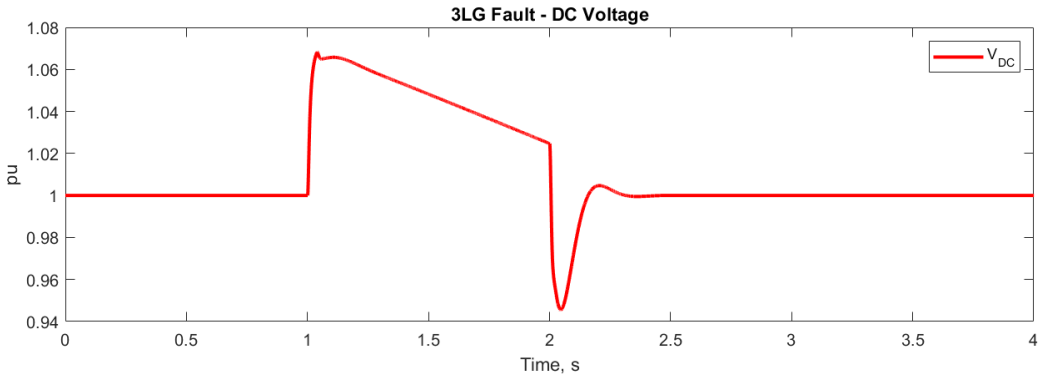

Fig. 5.25 DC bus voltage

DC bus is controlled at 1 pu all the time, which again shows perfect tracking of the PI controller. Chopper is activated during the fault when DC bus voltage rises to the defined threshold.

5.5 Type IV RMS Model - Improved

A single phase to ground fault is applied at bus 3 at t=1s. The real and reactive power output of the wind park is monitored and plotted in the following diagram:

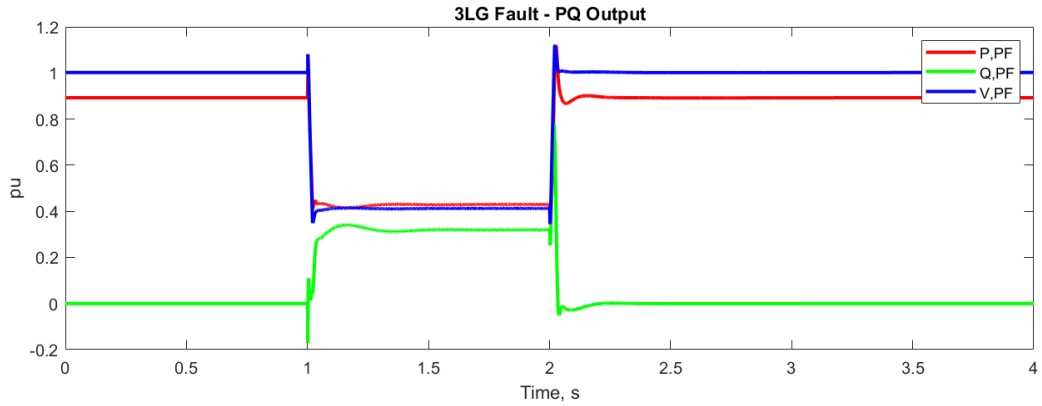

Fig. 5.26 PQ Output at POI

As shown in the diagram, the simplified RMS model's real and reactive power output in steady state and during fault are very close to the original model. The voltage at POI is also very close.

Consider the inner control loop of GSC, the reference and measured current signals are plotted in the following diagram:

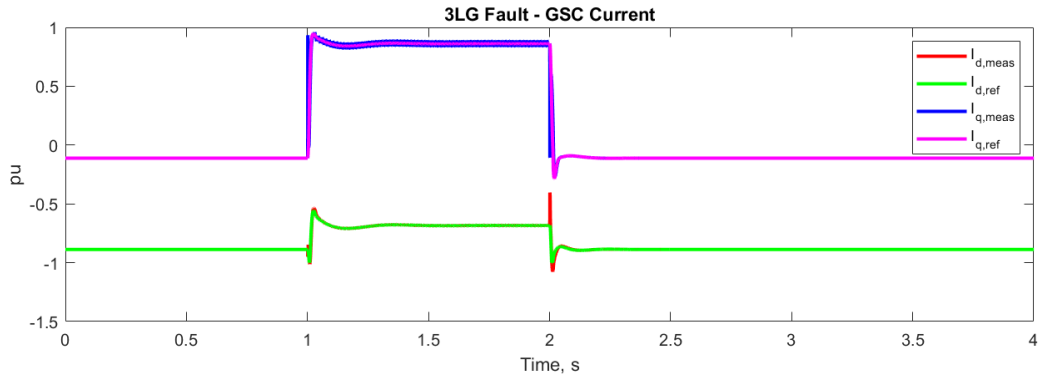

Fig. 5.27 GSC current

Which shows perfect tracking of the PI controller on both d and q axis current signals. Since the machine side is simplified into a controlled DC current source, there is no MSC controller in this model. Finally, the simulated DC bus voltage is shown in Fig. 5.28:

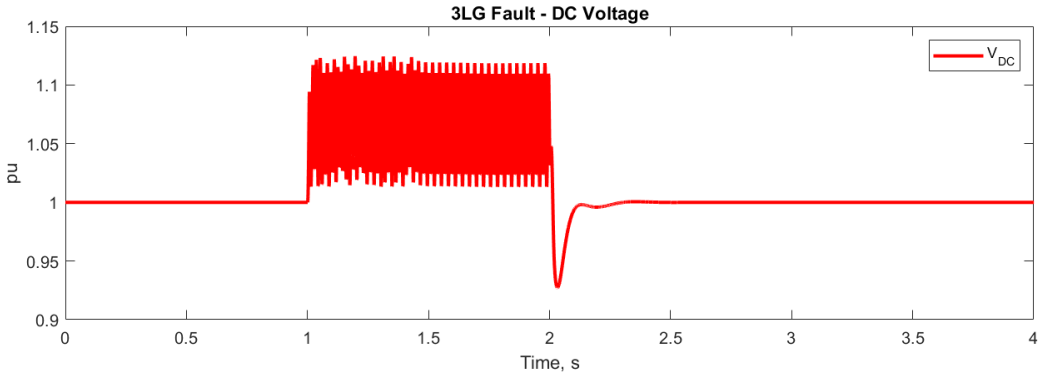

Fig. 5.28 DC bus voltage

DC bus is controlled at 1 pu all the time, which again shows perfect tracking of the PI controller.

5.6 Summary

According to simulation results, the developed EMT Type III and Type IV models are very accurate and shows very close results when compared against EMT models in another simulation software. The minor differences, such as differences in steady state values less than 0.01pu, differences in transient response waveforms and difference in oscillation amplitude, could be caused by difference in PI controller parameters, difference in model parameters and difference in solver options and initialization techniques between two software packages. For example, the transmission line model is defined as a simple pi circuit with positive, negative and zero sequence

impedance characteristics in PF, while in the other software the transmission line is defined by its propagation constant, therefore the pi circuit impedance values are chosen based on approximation. The solver of PF uses implicit methods which are considered to be more precise as opposed to Dommel's methods used in other EMT tools.

The developed RMS models also show stable simulation results under different fault scenarios. PI controllers show good tracing against the reference signals. The improved simplified RMS model for Type IV WP, shows very close results against the full RMS Type IV WP model, making it a good candidate for transient studies. However, the full RMS model is still needed for studies involving MSC, wind turbine pitch angle and wind speed, which the simplified model lacks.

CHAPTER 6 SIMULATIONS CASES

6.1 Power Swing Study

Power swing is a dynamic event described as temporal oscillation in active and reactive power flows on a transmission line consequent to a large disturbance in the system such as clearance of a fault by disconnecting a line, loss or connection of a large load and disconnection of a generator [34]. During a power swing, the impedance vector traced by distance relays shows a steady progression and may move inside the distance protection zone. A short circuit on a transmission line is also a dynamic event where the impedance after fault inception moves quickly from the operating point to the short circuit impedance in the distance protection zone [35-37]. These similar behaviors may lead to maloperation of line distance protection on a healthy line during a power swing.

Tripping of distance relay during power swing can be inhibited by using a traditional protective relaying element called power swing blocking (PSB) function, which distinguishes between power swing and short circuit, by measurement of the rate of change of impedance vector and comparison with a threshold [38-40]. Another function associated with power swing protection is Out-of-step Tripping (OST) function that differentiates between a stable and an unstable swing based on the swing impedance trajectory and initiates system partitioning in case of an unstable swing [41-43]. In summary, the objective of power swing protection in distance relaying is twofold. (i) Prevent from unintentional tripping of distance relay during a stable power swing to allow the system to return to a new balance of generation and load. (ii) Detect unstable power swings by checking out-of-step (OOS) condition and initiate tripping to separate the power system into sections with a generation load balance at predetermined locations to prevent widespread power outage and equipment damage.

Inverter-based resources (IBRs) include solar plants and wind parks employing Type-III and Type-IV wind turbine generators. Their dynamic behavior during a fault and after clearance are different compared to conventional synchronous generators (SGs) and depends largely on control schemes of inverters, which have fast response times [29,30]. Given that, there is a surge of interest in identifying the performance of various conventional protection schemes, including distance protection, directional protective relay elements, negative-sequence based protection schemes, Rate-Of-Change-Of-Frequency (ROCOF) protection and power swing protection [44-47].

Integration of IBRs can considerably speed up the power swing characteristics due to reduced system inertia and result in misinterpretations by PSB and OST functions if set under the assumption of conventional SGs [48-50]. Given the dynamics and complexity of control structures with fast response time, detailed transient models of IBRs have been used to identify misinterpretation issues of power swing protection and revise settings accordingly [51,52].

As the integration of IBRs continues, protection engineers face new challenges in modelling, analysis and simulation of power systems. This paper aims to identify solver requirements to conduct power swing studies under wind generation. This is necessary to ensure that protection engineers have confidence in their simulation tools and results.

This part studies the possible negative impacts of wind generation on power swing protection using both RMS and EMT solvers and provides examples of misinterpretations by traditional PSB and OST functions set under the assumption of conventional SGs. Finally, results obtained with RMS models are compared against original EMT models and the accuracy of developed RMS models are assessed.

6.1.1 Background

Consider first the PSRC WG-D6 test system given in Fig. 6.1 and its simplified version given in Fig. 6.2. The simplified circuit consists of two sources represented by voltage sources $\boldsymbol{E}_G$ and $\boldsymbol{E}_S$ behind impedances $\boldsymbol{Z}_{Geq}$ and $\boldsymbol{Z}_{S1}$, two identical transmission lines represented by $\boldsymbol{Z}_L$, and a distance relay denoted by D. $\boldsymbol{E}_G$ is leading $\boldsymbol{E}_S$ by δ, referred to as transmission angle.

Fig. 6.3 shows the application of a preliminary approach called equal area criterion for understanding and visualizing dynamic system stability following fault inception and auto-reclosure (ARC) attempt. In steady-state, the relay measures the load impedance with an angle of δ_0. Area A corresponds to the short-circuit period, where voltages collapse and mechanical power from the turbines exceeds transferred power leading to acceleration of generators. Area B represents the dead time in auto-reclosing whereas Area C successful auto-reclosure. During these periods, the generators will reduce speed as the transferred power exceeds mechanical power. With an ARC scheme that successfully operates, the generators will return to their initial stable operating point if the braking area is larger than the accelerating area which is possible with short fault clearance times. The same condition for stability holds without an ARC scheme or with an

unsuccessful ARC attempt, but the generators will move to another stable operating point in that case [53-55].

By dividing the voltages with load current, the power swing process explained above can be shown on an impedance diagram as seen in Fig. 6.4. The distance relay is located at the origin of this diagram. Dashed orange lines represent voltages that are assumed to be equal for simplicity. The load impedance trajectory is as follows: 0) Steady-state operation. 1) Fault inception. 2) Tripping of the faulted line. 3) Back to new load impedance with one line out. This is larger than the initial steady-state point due to disconnection of a line. 4) Advancing generator rotors. 5) Following ARC, a new impedance location while moving into distance protection zones. 6) All the way back to the starting point if ARC is successful or equilibrium in another location if line is disconnected (see the arrowhead).

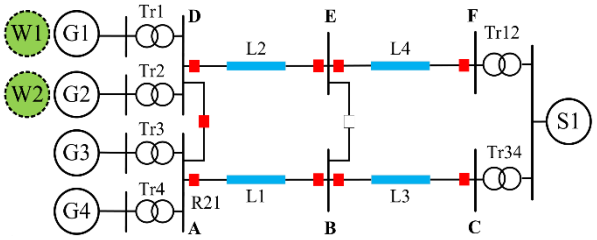

Fig. 6.1 PSRC WG-D6 test system

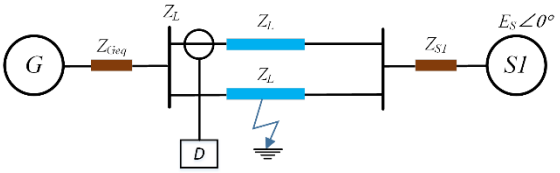

Fig. 6.2 Simplified two-machine system

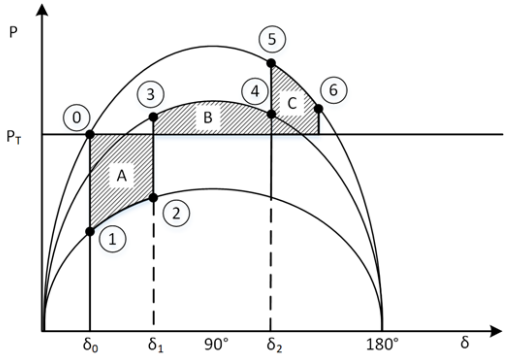

Fig. 6.3 Equal area criterion for dynamic stability

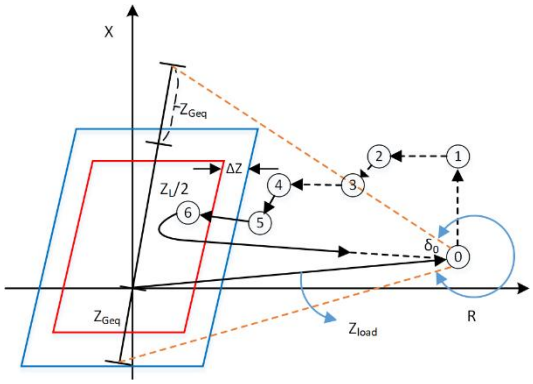

Fig. 6.4 Power swing trajectory on the impedance plane

If the load impedance enters in the distance protection zone and remains for a sufficient amount of time, distance relay tripping may occur. The PSB function of relay measures the rate of change of the apparent impedance, to distinguish a power swing from a fault. This rate is slower during a power swing because it is proportional to the slip frequency of machines, which is a function of the large inertia of machines. Typical settings are $\Delta Z = 10 - 20\% Z_A$ and $\Delta t = 20 - 40ms$ which allows detecting power swings in the range of 2 – 3 Hz [56,57].

Integration of wind generation reduces system inertia and results in faster dynamics and larger rate of change of impedance. If PSB settings are determined considering SGs, the function may not be able to distinguish power swing from short circuit under wind generation [58,59].

Wind generation alters also the trajectory of impedance vector. The reach of an OST element determined based on stability limits under SGs may not be adequate under wind generation [60].

6.1.2 Simulation and results

The IEEE PSRC WG-D6 test system is shown in Fig. 6.1. Two generating stations, denoted as A and D, are connected to an equivalent system S1 by a 500 kV transmission system that consists of four transmission lines L1-L4. Four 250 MVA SGs, marked as G1-G4 are connected to two generating stations A and D. All SGs are connected to the transmission system through identical generator transformers Tr1-Tr4. SG models G1-G4 are identical, with controllers consisting of IEEEST1 power system stabilizer and SEXS exciter. The rest of the network is modeled with S1, a 240 kV ideal voltage source behind a Thevenin impedance. Breaker connecting bus E and bus B is open and all other breakers are closed. Power flow is from generators G1-G4 to S1.

In order to investigate the system's performance with different levels of wind generation, SGs G1 and G2 are replaced with two wind parks, marked as W1 and W2. It is already discussed that, in the original network, loss of a transmission line L1 or L2 caused by a fault could result in either a stable or unstable power swing. Whether the power swing is stable or not is determined by pre-fault loading conditions and the fault clearing time. Unstable power swing could be triggered by longer fault clearing times due to for example stuck breakers, and the power swing between G1-G4 and the rest of the system is a result of the acceleration of SGs during fault and the reduced power transfer capability after fault clearance.

To study power swing characteristics, a power swing relay R21 is added to the original network in Fig. 6.1. The distance relay zones and power swing relay elements are shown in Fig. 6.5. All impedances are measured from the secondary side of the relay. The current transformer (CT) ratio is 800/5A, and the voltage transformer (VT) ratio is 500/0.115kV. These CT and VT configurations are based on the original network without any wind generation. The distance relay has its zone 1, 2 and 3 set to 80%, 135% and 200% of line L1 respectively. There is no time delay for zone 1, but zone 2 and zone 3 have time delay of 20 and 40 cycles, respectively.

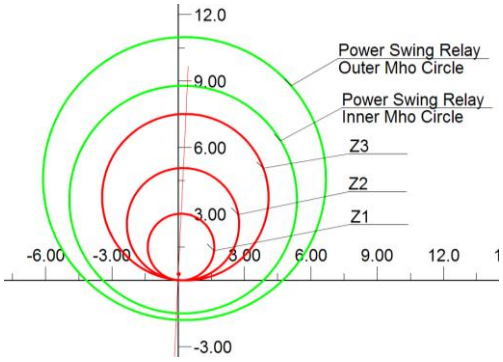

Fig. 6.5 Distance and power swing relay MHO circles

The power swing protection relay uses a two-step mho detection scheme, which supervises all three zones of the distance relay. Detailed relay settings are shown in Table 6.1.

Table 6.1. Settings of distance and power swing protection of relay R21

Setting	Value	Calculation procedure
Distance Relay		

Z1	3.00Ω	80% of L1
TD1	0 cycles	Time delay of Z1
Z2	5.07Ω	135% of L1
TD2	20 cycles	Time delay of Z2
Z3	7.51Ω	200% of L1
TD3	40 cycles	Time delay of Z3
Power Swing Relay		
Line impedance	3.75Ω ∠87°	Positive sequence
	11.26Ω ∠84°	Zero sequence
Forward reach outer	11Ω	Set to more than the forward reach inner.
Reverse reach outer	1.8Ω	
Forward reach inner	8.8Ω	Set to encompass the largest distance protection zone to be blocked by PSB.
Reverse reach inner	1.1Ω	
Forward RCA	87°	Set equal to the phase angle of the positive sequence line impedance.
Reverse RCA	87°	Set the same as forward RCA.
PSB time delay	0.08s	Set based on the maximum rate of change of impedance to ensure fastest OOS conditions are detected.
PSB reset delay	0.16s	

PSB: The PSB function uses inner and outer Mho circles which are separated by impedance ΔZ, together with a timer ΔT. If the trajectory crosses the outer and inner circles before the timer expires, the PSB determines the event as a fault and does not signal PSB. However, if the measured impedance trajectory enters the inner circle before the timer expires, a PSB signal is issued and the distance relay tripping is blocked.

OST: The OST function uses inner Mho circle to determine whether a power swing is stable or unstable. The OST function is set according to the most severe stable power swing, to ensure the most severe stable power swing is not declared as unstable.

Power swing in PRSC-D6 network is simulated under three different scenarios: no wind generation, 25% wind generation and 50% wind generation. For 25% wind generation, SG G1 is replaced with wind park W1, and for 50% wind generation, SGs G1 and G2 are replaced with wind parks W1 and W2. All wind parks are configured to inject same amount of real and reactive power as SGs to achieve same pre-fault condition.

A 270-ms three-phase-to-ground fault is applied to L2 close to substation E. Fault is cleared at t=2s by disconnecting line L2 and therefore resulting in an unstable power swing. The scenario is simulated using both RMS and EMT methods, under no wind generation and 25% wind generation. The impedance trajectory measured by the power swing relay is shown in Fig. 6.6, and its output is shown in Fig. 6.7. The same simulation is repeated under 50% wind generation and the results for both simulations are shown in Fig. 6.8 and Fig. 6.9.

In Fig. 6.6, both EMT and RMS simulations show that under no wind generation, the trajectory crosses the outer and inner element of the power swing relay after the PSB timer expires. Therefore, the relay successfully detects the power swing and issues PSB signal, as shown in Fig. 6.7. OOS signal is also issued when the trajectory leaves the outer Mho element of the power swing relay. Under 25% wind generation of Type IV WP, the impedance trajectory travels faster compared to no wind condition, and it enters the inner element before the timer expires, causing the power swing protection maloperation. As shown in Fig. 6.7, no PSB signal is issued until the trajectory leaves the outer element. Since no PSB signal is issued, Z2 element of distance protection operates and could result in outage of line L1 if the distance protection relay is used in a pilot relaying scheme like Permissive Overreaching Transfer Trip (POTT). Both EMT and RMS simulations show that the impedance trajectory travels faster under 25% wind generation condition, which is expected. As for Type III WP, measured trajectory shows no maloperation with 25% wind generation.

Comparing different RMS models against the EMT model, it can be observed that the proposed improved voltage source-based RMS model and complete RMS model of Type IV WP has very close results when compared against the original EMT model, whereas the current source based RMS model shows some difference in simulation results when compared against the EMT model.

Same for Type III WPs, the EMT and proposed RMS model have close results, where the current source-based introduces additional error.

When wind generation level is increased to 50%, i.e. two SGs are replaced with WPs, PSB maloperation can be observed in all simulations. When comparing simulation results against the EMT model, it can be observed that Type IV proposed voltage source-based model and Type IV complete model both show close results to the EMT model, where the current based model shows even more discrepancies. Similar behavior can be observed for Type III RMS models, where the current based model has stability issues pre fault and the whole system loses synchronization before the fault is applied.

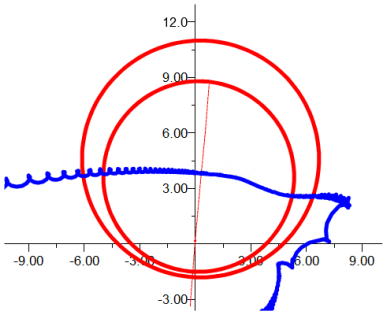

4SG EMT

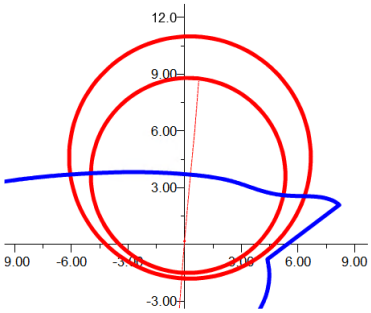

4SG RMS

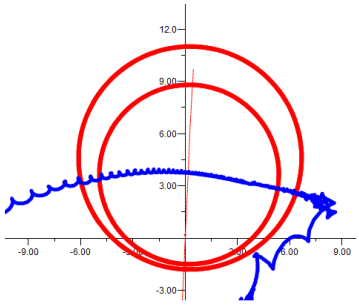

3SG1WP Type IV EMT

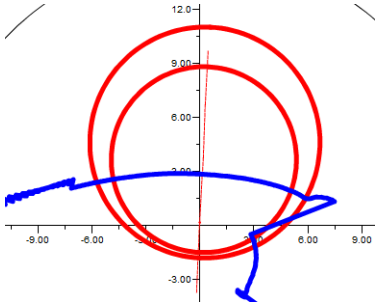

3SG1WP Type IV RMS Simple

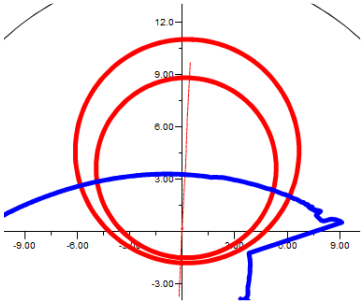

3SG1WP Type IV RMS Proposed

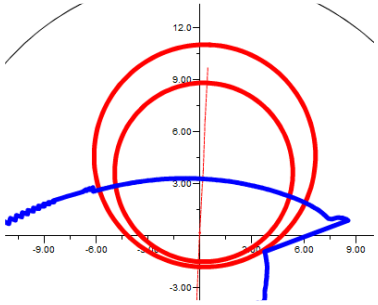

3SG1WP Type IV RMS Full

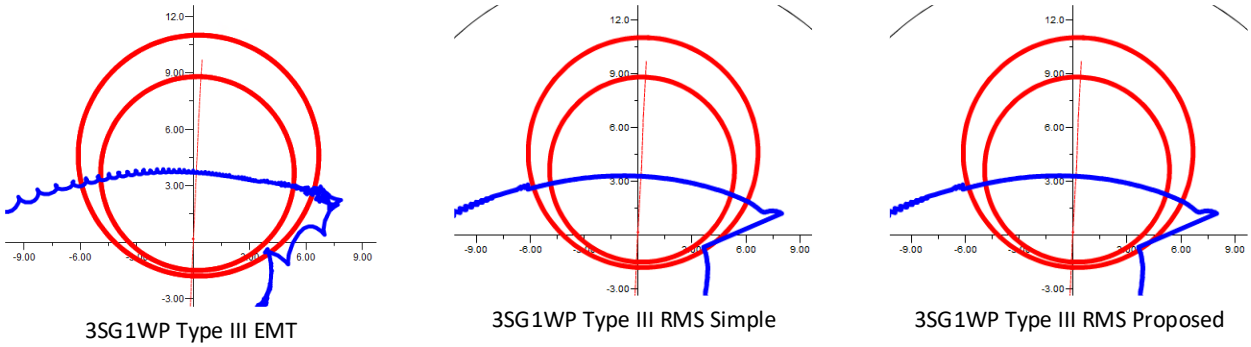

Fig. 6.6 Impedance trajectory with no wind and 25% wind generation

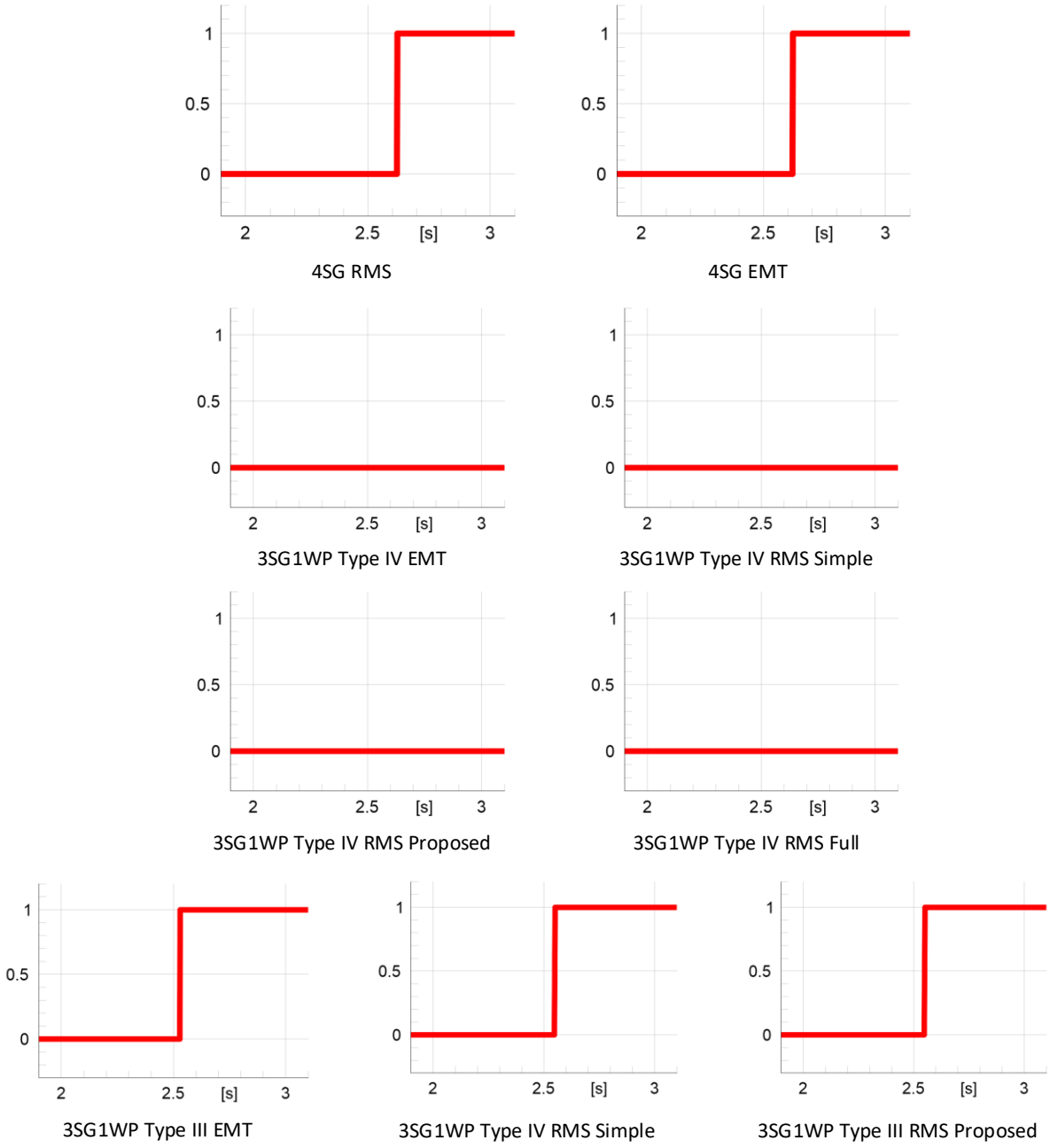

Fig. 6.7 PSB relay output with no wind and 25% wind generation

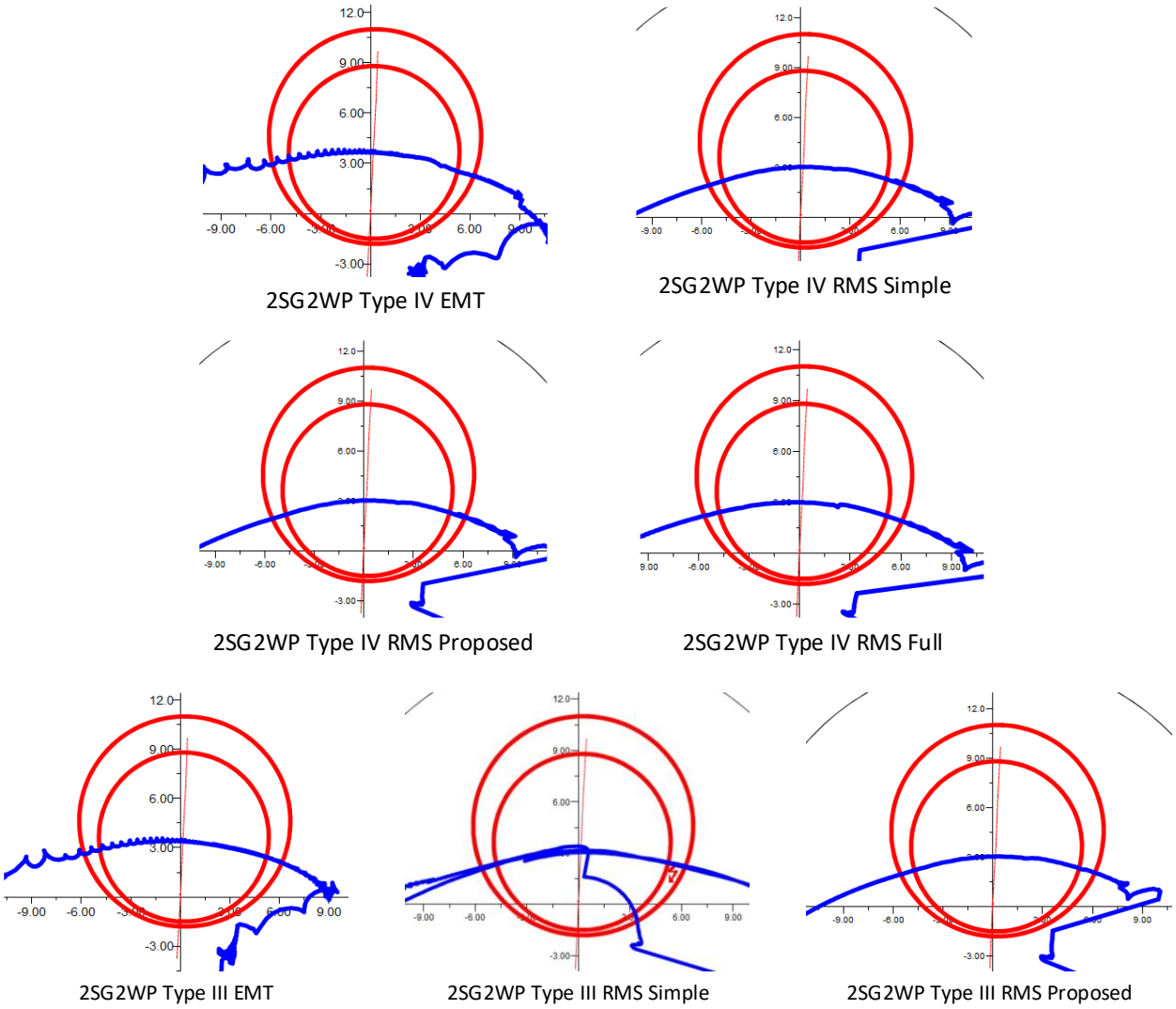

Fig. 6.8 Impedance Trajectory with 50% wind generation

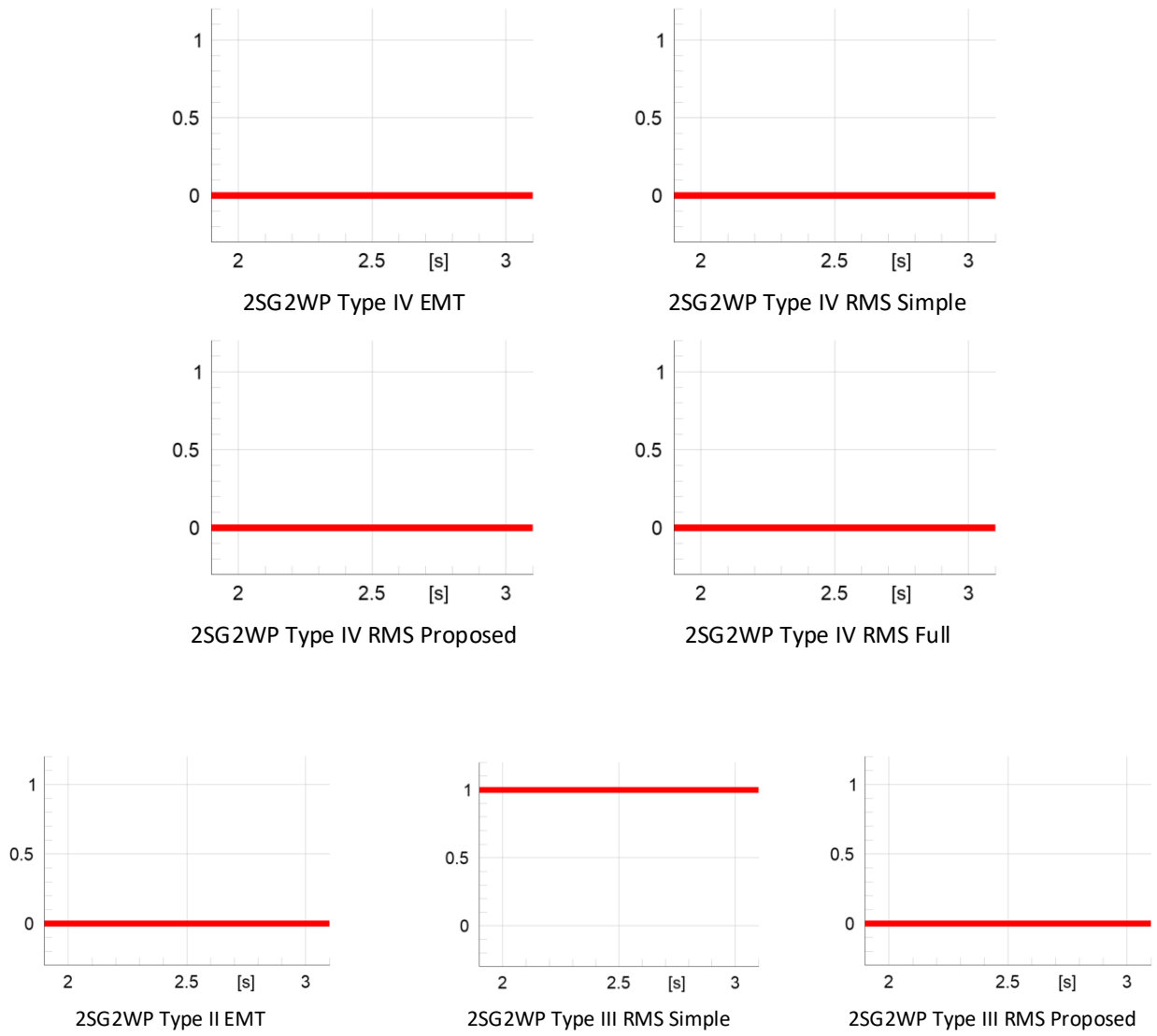

Fig. 6.9 PSB Relay output with 50% wind generation

The simulations show that under high level of wind integration, PSB may not operate as expected due to the increased rate of change of the swing impedance vector under wind generation. Simulation results also show that the proposed voltage source-based RMS models give very accurate results in terms of $\Delta Z/\Delta t$ as summarized in Table 6.2. Since RMS solver only runs on fundamental frequency and ignores high frequency and DC components, it does not capture the full transient characteristics of a fault event and therefore the shape of EMT and RMS trajectories are different at a closer look.

Table 6.2 PSB time delay in cycles

PSB time delay (cycles)			
Model	Wind generation level (%)		
	0	25	50
EMT Type IV	5.52	4.47	3.21
EMT Type III	5.22	4.87	4.39
RMS Type IV Simple	5.22	4.38	3.01
RMS Type IV Proposed	5.22	4.51	3.18
RMS Type IV Full	5.22	4.53	3.23
RMS Type III Simple	5.22	4.81	N/A
RMS Type III Proposed	5.22	4.85	4.36

To demonstrate the OST maloperation, most severe power swing is considered for no wind generation and 50% wind generation conditions. In the original network, the most severe power swing for no wind generation happens when an 88-ms three-phase-to-ground fault occurs on L2 and followed by the clearance of the fault by disconnecting L2 at t=2s. For 50% wind generation condition, the duration of the fault to trigger the most severe stable power swing is determined experimentally. Simulations are executed using both EMT and RMS methods, and the result is shown in Fig. 6.10.

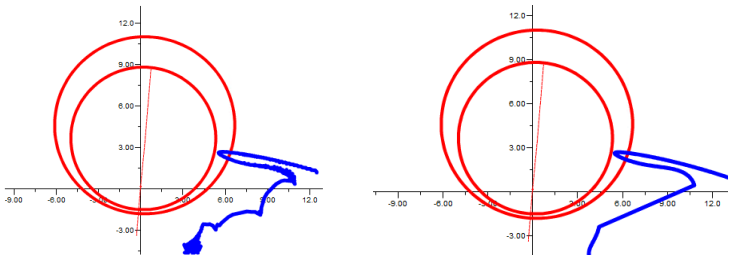

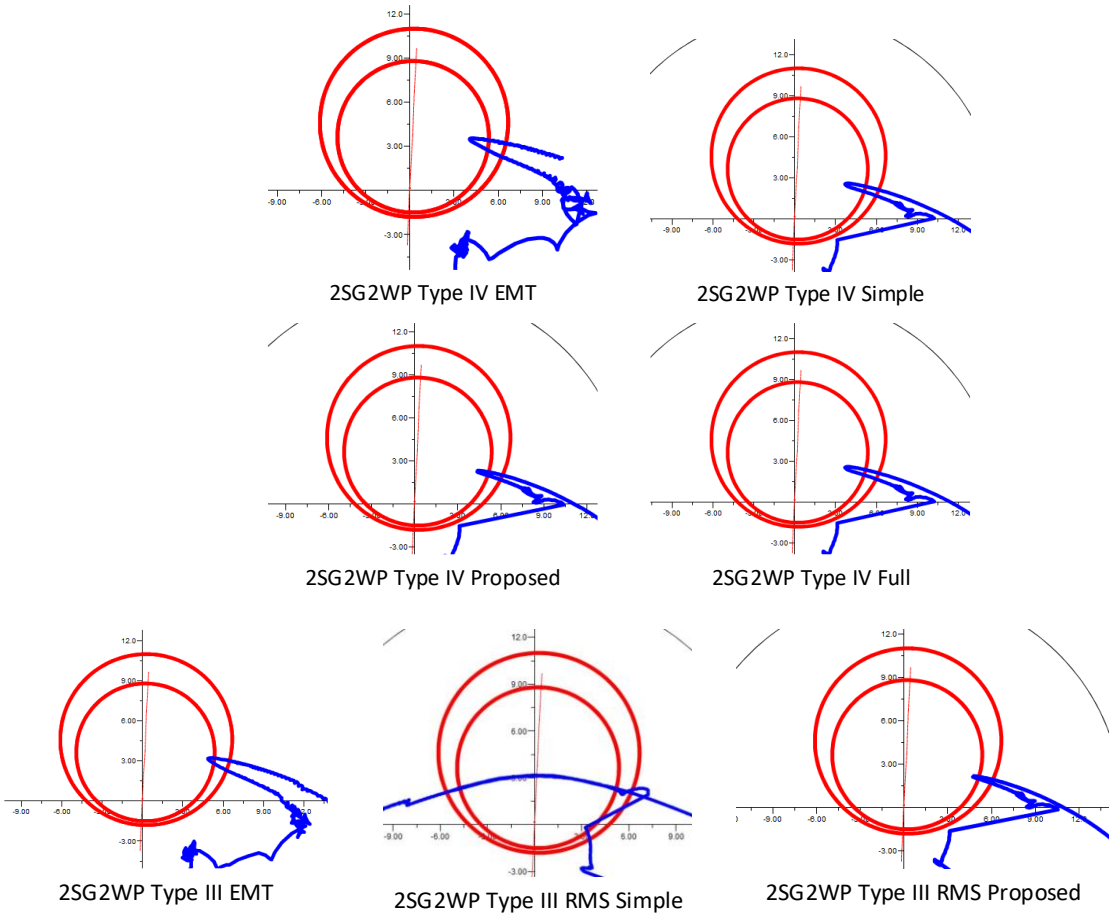

Fig. 6.10 Trajectory of most stable power swing with 50% wind generation

R-X plot in Fig. 6.10 shows that the impedance trajectory of the most severe power swing under no wind condition reverses direction before it enters the inner Mho element of the power swing relay. Therefore, only PSB signal is issued and the relay does not detect OOS. Under 50% wind generation condition, the trajectory of the most severe power swing reverses direction inside the inner element of the power swing relay, causing maloperation of the OST function, as demonstrated in Fig. 6.11.

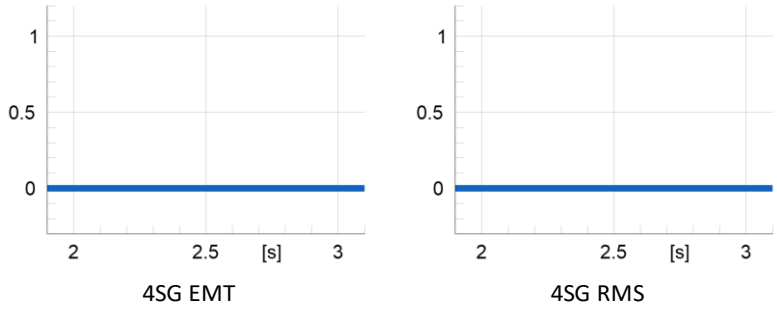

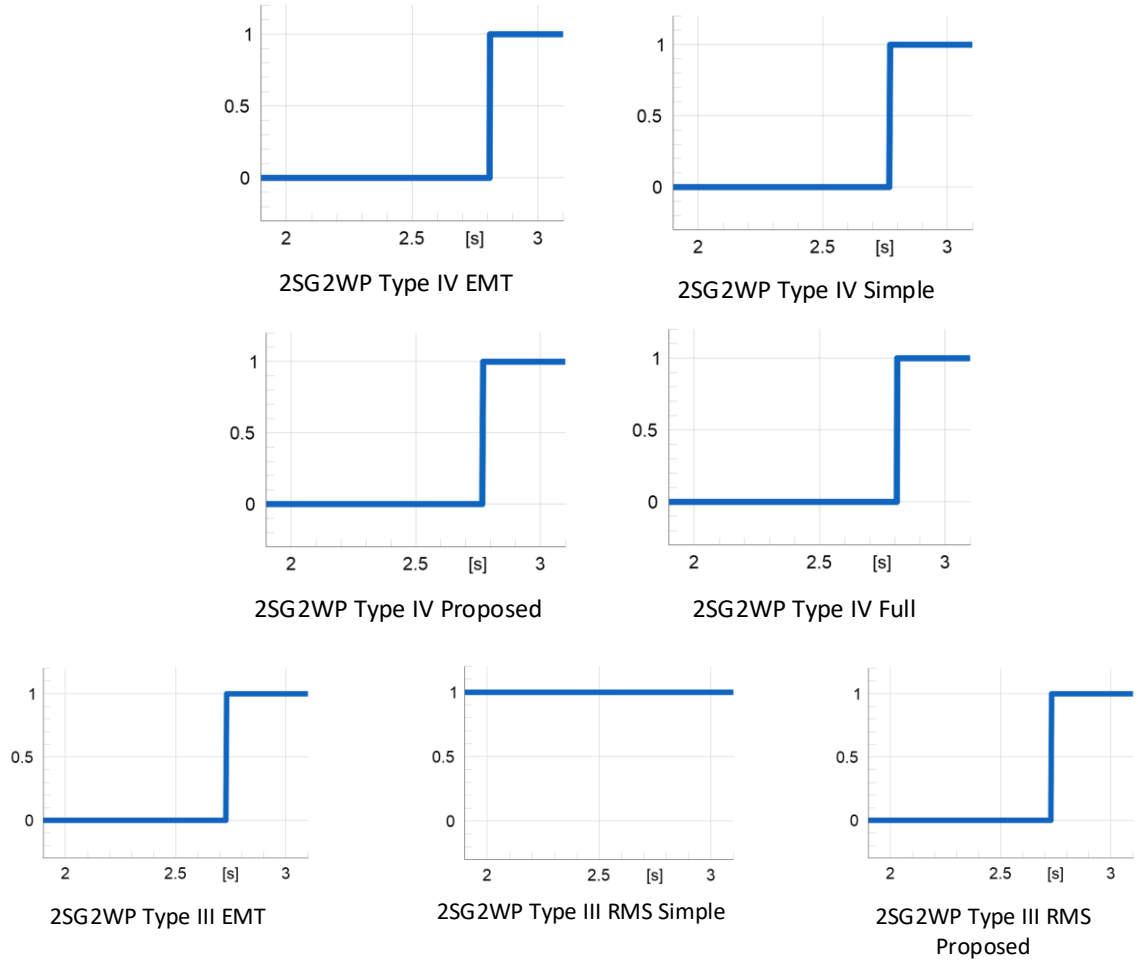

Fig. 6.11 OOS relay output signal with 50% wind generation

Comparing simulation results of EMT and RMS models, it can be observed that the proposed voltage source based Type III and Type IV RMS models show close results against the EMT models. The Type III current source-based RMS model again shows some stability issues when wind generation is at 50% level, where stable power swing could not be found.

Table 6.3 Total simulation time

Total simulation time (seconds)			
Model	Wind generation level (%)		
	0	25	50

EMT Type IV	14.3	83.2	105.8
EMT Type III	15.7	87.7	112.1
RMS Type IV Simple	1.3	2.1	2.8
RMS Type IV Proposed	1.3	2.7	3.2
RMS Type IV Full	1.3	3.1	3.6
RMS Type III Simple	1.3	2.2	2.7
RMS Type III Proposed	1.3	2.8	3.2

Finally, the total simulation time is also recorded in Table 6.3. As shown in the table, all RMS models are considerably faster than EMT models, up to 35 times faster when multiple WP models present in the same network. Even with the more complicated Type IV full RMS model, time difference between as opposed to simple current source-based RMS model is negligible. Considering the close results obtained from voltage source-based RMS models proposed before, using RMS simulation could potentially save considerable amount of time for trial and error-based studies.

6.2 Critical clearing time study

Transient stability following fault inception is an important study to be considered in power system planning. For conventional power systems, RMS simulation is proven to be fast and accurate. However, as IBR penetration level increases, the mechanism governing transient stability and power swing changes. This section briefly demonstrates the principle behind transient stability, and discusses potential challenges caused by IBR integration.

6.2.1 Background

In conventional power systems dominated by SGs, transient stability is determined by rotor angle of SGs, and the underlying mechanism is well elaborated [61-63]. Take the single-machine infinite bus system in Fig. 1 as an example, the electromagnetic power Pe produced by the SG is a function of power angle δ_{SG} and the transient internal voltage magnitude:

$$P_e = \frac{E' U_g}{X_T} \sin \delta_{SG} \tag{6.1}$$

where X_T is the sum of SG's transient impedance X'_d and the transfer impedance of the network X_{tr}. δ_{SG} is the angle difference between rotor and grid voltage, i.e. $\delta_{SG} = \theta_r - \theta_g$. U_g is the open-circuit voltage magnitude of the power grid.

Once a three-phase short circuit occurs, U_g and P_e rapidly decreased due to low fault impedance. Since the input power P_m is determined by the mechanical system and cannot be changed instantly, the power unbalance P_m-P_e drives the rotor to accelerate [64]. After the fault is cleared, U_g recovers to rated value, and the rotor starts to decelerate. The system is transient unstable when the fault duration is greater than the CCT, which implies the deceleration area is less than the acceleration area. From operational and empirical perspective, transient instability occurs once power angle δ_{SG} exceeds 180°, as power angle larger than 180° will reduce P_e, which in turn further increases δ_{SG} [65-67]. Typically, CCT of a practical SG is determined by the pre-fault operation point (P_m) and grid strength (X_{tr}).

With the increasing integration level of WPs and other IBRs using full-scale converters, modern power systems have different dynamics in transient stability because IBR transient dynamics are dominated by control-loops [68-70]. As shown in the control schematic previously, PLL measures the terminal voltage and governs the synchronization dynamics of the WP. Furthermore, due to the

existence of grid impedance, the inner-loop control and its current references (governed by outer-loop and current limiter) can significantly change the terminal voltage [71-73]. Therefore, active and reactive current references have critical impact on the transient stability of modern power systems. Take the same single-machine infinite bus system in Fig. 6.12 as an example, the angular frequency of PLL ω_{PLL} is

$$\omega_{PLL} = \omega_1 + K_{pPLL} U_{tq}^{PLL} + K_{iPLL} \int U_{tq}^{PLL} \, \mathrm{d}t \tag{6.2}$$

where ω_1 is the angular frequency of grid voltage. K_{pPLL} and K_{iPLL} are the proportional and integral parameters of PLL's PI controller, and can be obtained as

$$U_{tq}^{PLL} = -U_g \sin(\delta_{PLL}) - X_{tr} I_t \sin\theta_I \tag{6.3}$$

where θ_I is the angle of injected current with respect to the PLL reference frame. δ_{PLL} is the angle difference between PLL reference frame and the grid voltage, i.e.

$$\delta_{PLL} = \theta_{PLL} - \theta_g = \int \omega_{PLL} \, \mathrm{d}t - \theta_g \tag{6.4}$$

During a three-phase short circuit close to the Type-IV WP, the first term in (6.4) dips to zero and the terminal voltage is only determined by the voltage drop on Z_{tr}. The sign of the second term U_{tq}^{PLL} depends on θ_I, and it determines whether ω_{PLL} rise or fall from the rated value ω_1 as shown in Fig. 6.13. After the fault is isolated, the first term in (6.4) recovers and ω_{PLL} is supposed to converge to ω_1. However, if ω_{PLL} deviates too far from ω_1, ω_{PLL} will fail to recover, which results in transient instability in PLL's measured frequency δ_{PLL}, as shown in Fig. 6.13.

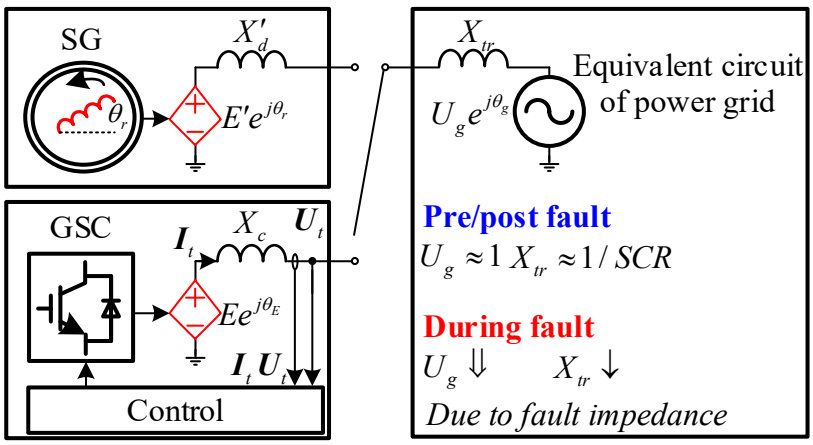

Fig. 6.12 Equivalent circuit of transient stability model

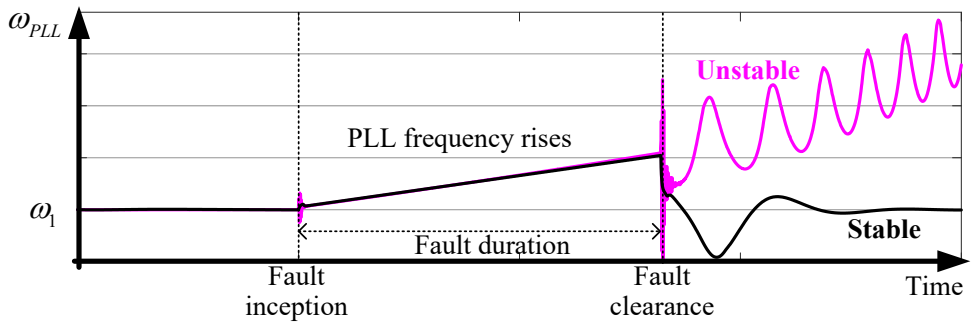

Fig. 6.13 Stable vs unstable transients

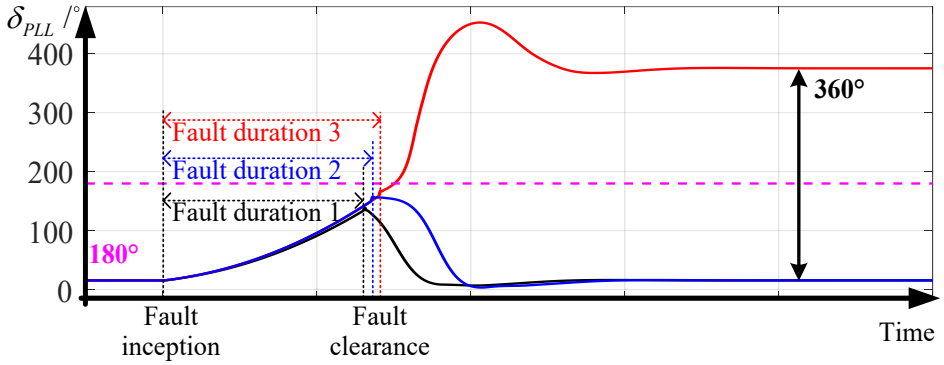

Fig. 6.14 Unstable transients caused by longer fault duration

It's worth noting that, different from rotor angle instability of SGs, δ_{PLL} of IBRs exceeding 180° won't always lead to transient instability [74-76]. Owing to the path-dependent damping effect introduced by control loops, δ_{PLL} is possible to eventually converge as shown in Fig. 6.14. As a result, although calculating methods for transient instability of δ_{PLL} with simplifications are available, dynamic simulation is still the dominating method for project specific studies [77-80].

From the perspective of power system planners, accurate and efficient models are required to assess CCTs of different SG/IBR-integrated power systems in order to coordinate protection elements to prevent possible transient instability and protection maloperation.

6.2.2 Simulation and results

The detailed EMT model as well as the proposed RMS model of DFIG-based WP are integrated in the revised EPRI benchmark system shown in Fig. 6.15 for CCT assessment of the wind farm. A bolted three-phase short circuit is applied at BUS1 at 1s. In EMT simulations, a fixed time step (50μs in these studies) is adopted to ensure accuracy. In contrast, for the RMS simulations, variable-

step solver is adopted (maximal time step is set to 3.33ms). The EMT and RMS simulation results of PLL variables governing synchronizing process in different fault durations are compared in Fig. 6.16 to Fig. 6.19. The EMT simulations suggest that the power system becomes unstable when the fault duration is greater than 0.25s, whereas RMS simulation results suggests 0.28s. The CCT error of using the proposed RMS model is 30ms and 12%. The discrepancy is caused by the simplifications of DFIG-based WP model and networks in RMS simulation. It is worth noting that the above transient instability is dominated by the PLL, and no transient instability can be detected when using the original current source-based RMS model.

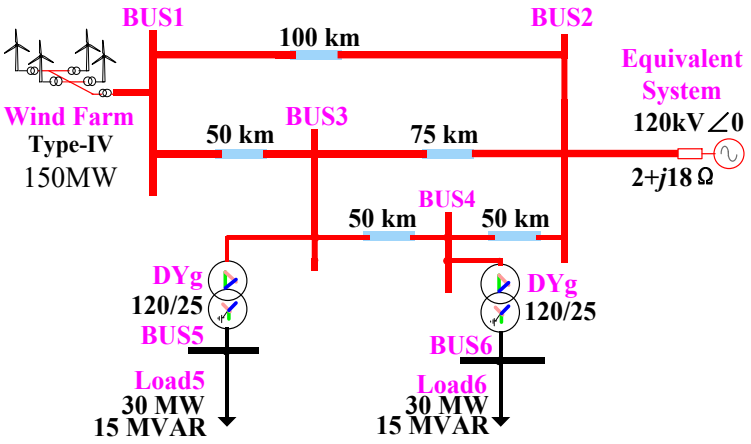

Fig. 6.15 Modified EPRI benchmark system

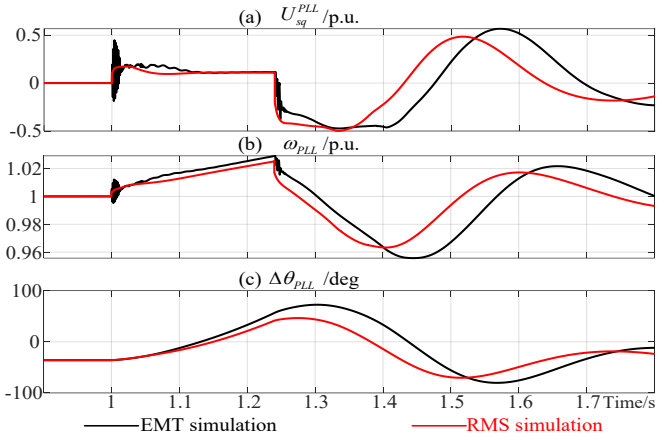

Fig. 6.16 EMT and RMS simulation results of synchronizing process when fault duration is 0.24s

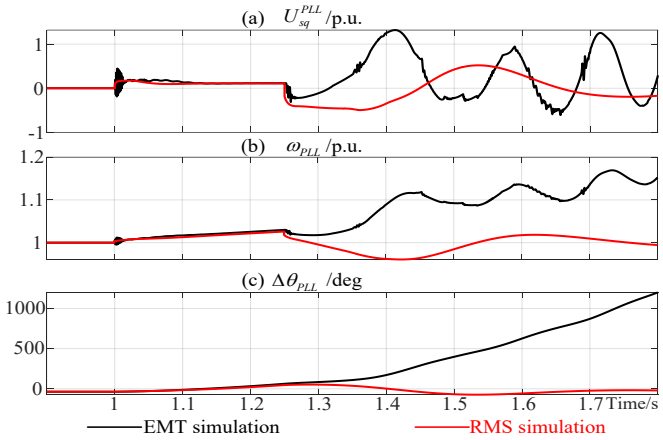

Fig. 6.17 EMT and RMS simulation results of synchronizing process when fault duration is 0.25s

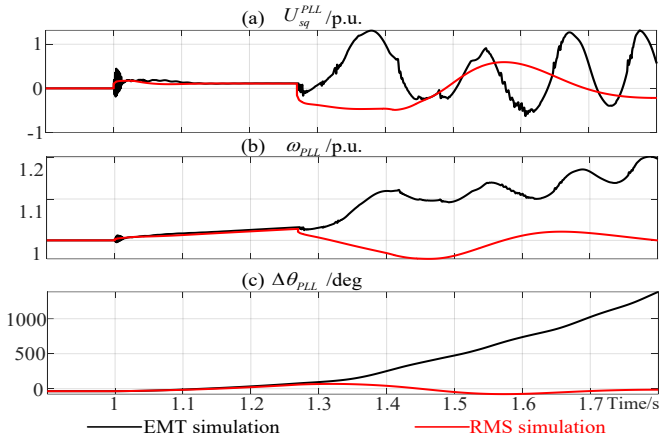

Fig. 6.18 EMT and RMS simulation results of synchronizing process when fault duration is 0.27s

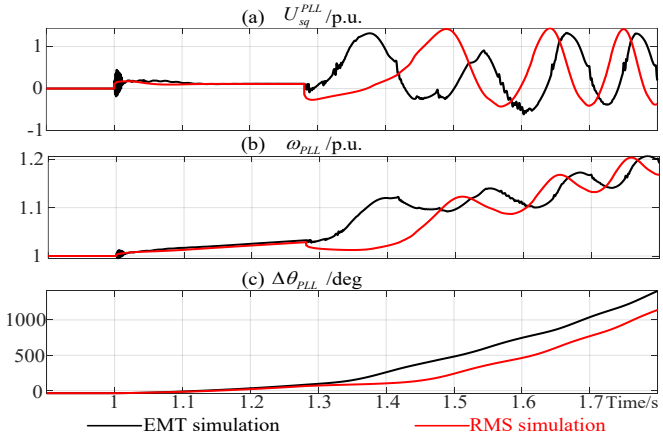

Fig. 6.19 EMT and RMS simulation results of synchronizing process when fault duration is 0.28s

The execution time of above 2 seconds case study in EMT is around 30 secs, while the execution time for RMS simulation using the proposed model is only about 3 seconds. Compared with the existing RMS models of DFIG-based WP, the proposed model is an efficient way to study transient instability dominated by converter control, especially for trial-and-error based CCT assessment where a series of varying fault duration need to be simulated.

The same simulation is repeated for Type IV WP models in the revised EPRI 6-bus benchmark system, as shown in Fig. 6.15. A 150 MW Type-IV WP is connected to a relatively weak AC system with 2.9 SCR seen from the WP. The CCT of this WP is determined by trial-and-error, where bolted three-phase-to-ground short circuit of different durations are applied on Bus 1.

First, EMT simulations are executed in PF with detailed EMT Type-IV WP model. Based on 14 trials with different fault durations, the CCT is between 0.23s and 0.24s, since ω_{PLL} and δ_{PLL} are stable when fault duration is 0.23s and are unstable when fault duration is increased to 0.24s, as presented in Fig. 6.20 and Fig. 6.21. These EMT studies set a reference for following CCT assessment using RMS simulation. It is worth noting that EMT simulation requires small time step (50μs in these studies) to ensure accuracy. The execution time of each EMT study is around 30s, and the execution time for CCT assessment with EMT simulation will dramatically increase in large-scale networks.

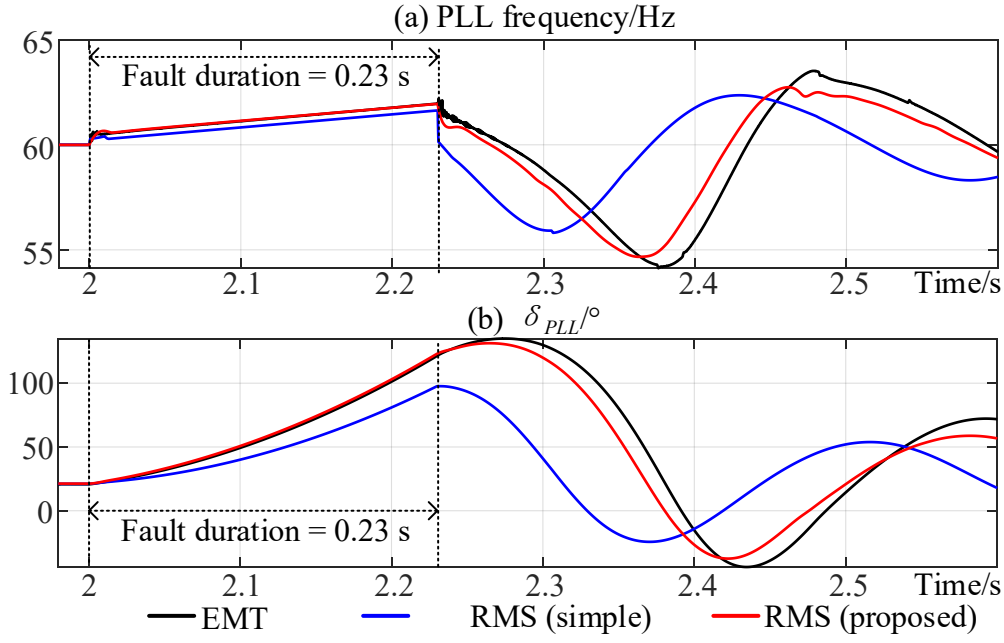

Fig. 6.20 EMT and RMS simulation results of ω_{PLL} and δ_{PLL} when fault duration is 0.23s.

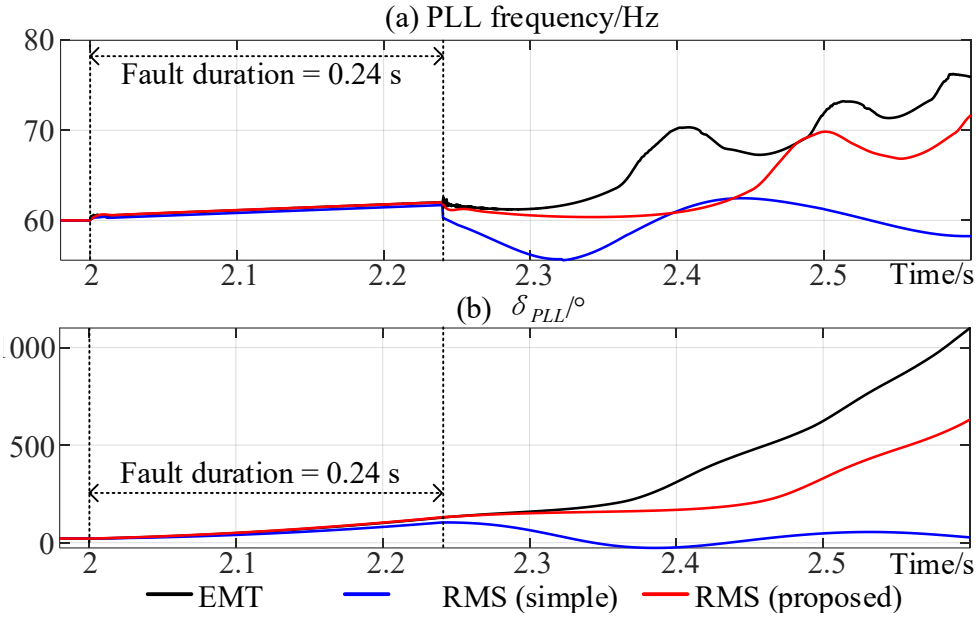

Fig. 6.21 EMT and RMS simulation results of ω_{PLL} and δ_{PLL} when fault duration is 0.24s.

Second, by changing the simulation method into RMS, the CCT is evaluated again with the current source-based RMS model (denoted by previous in comparison). With similar trial-and-error method, the CCT is determined to be between 0.28s and 0.29s as suggested by simulation results in Fig. 22. Moreover, both ω_{PLL} and δ_{PLL} are stable when fault durations are 0.23 s and 0.24 s as shown in Fig. 6.22. This indicates a significant error (50ms, 21.7%) in the CCT assessment caused by the previous RMS model

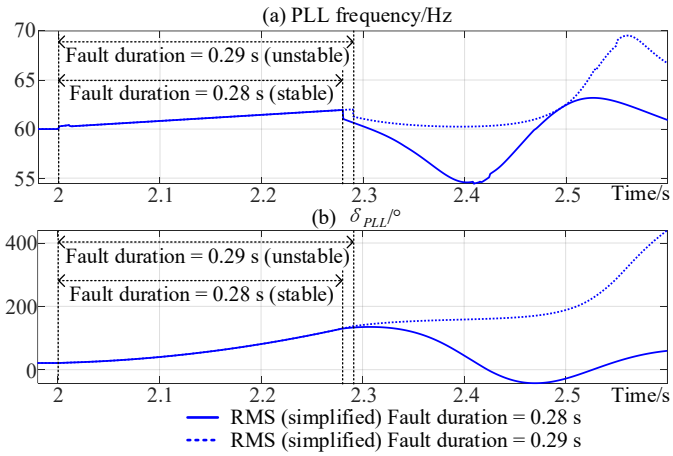

Fig. 6.22 RMS simulation results of ω_{PLL} and δ_{PLL} with the original RMS model in two different fault durations

Finally, previous RMS model is replaced with the proposed simplified model, and the CCT of the WP is evaluated again with a fixed time step of 1ms and a maximum error tolerance of 0.01%. The CCT is determined to be between 0.23 s and 0.24 s as shown in Fig. 6.20 and Fig. 6.21, which falls in the same range as the one obtained through EMT studies. This indicates that, by using the proposed RMS model, error of the CCT assessment can be reduced to an acceptable range (<5ms, <2.2%). It is worth noting that, due to greater time step used and algebraic representation of networks in RMS simulations, errors in time-domain waveforms still exist when compared with EMT simulation results. However, thanks to the nature of RMS solution, the execution time of each simulation is only 7s, which is 330% faster. This advantage makes the proposed RMS model a suitable tool for CCT assessment in complicated networks. The accuracy of RMS simulation is improved because the dynamics introduced by imperfect voltage feedforward and DC bus are recaptured in the proposed RMS model.

CHAPTER 7 CONCLUSION AND FUTURE DEVELOPMENT

7.1 Conclusion

Compared with EMT simulation, RMS simulation is a more efficient choice for trial-and-error based power system studies such as power swing and CCT simulations. However, the accuracy of RMS simulation becomes a major concern because of new dynamics introduced by IBRs. This research project develops RMS models of Type III and Type IV WPs for power system simulations. Compared with the existing RMS Type III WP models using current source interfaces and lacking PLL, the proposed Type III WP model is built with internal voltage equivalent circuits on the stator and GSC sides. The original equations of control plants and schemes are analyzed and transformed from EMT to RMS levels. Therefore, all critical state variables in the inner-loop control, PLL, FRT, and DC bus can be accurately emulated in the proposed model to ensure the accurate reproduction of the fundamental-frequency dynamics governing the synchronizing process of WPs. Moreover, by adopting the internal voltage interface on the DFIG stator side, rotor variables do not need to be initialized with complicated calculations and all state variables can be easily initialized from power flow results. Compared with the detailed EMT simulations that need to be run with small time steps, the proposed RMS model can be incorporated into variable-step solver and has much less execution time.

The developed RMS FSC-based WP model with proper representation of inner-loop and DC control branches is a fast yet accurate replacement of EMT model for transient stability studies. Compared with detailed EMT model, existing current source-based RMS model is simplified on the assumption of perfect current tracking. However, considering the imperfect voltage feedforward in practical designs, considerable overshooting and transients may occur in reference current's response to voltage dip. Moreover, the DC bus and MSC are also simplified in existing models, therefore DC bus dynamics are missing in the simplified RMS model. The proposed RMS model fully considers the effect of imperfect voltage feedforward and properly represents it in the inner-loop control. DC bus dynamics are also added by calculating DC bus voltage analytically. The accuracy of the proposed RMS model is verified against the current source-based simplified RMS model and the detailed EMT model in transient stability studies. Comparing simulation results, the proposed RMS model has very close results compared against EMT model, while being

considerably faster. The existing current source-based RMS model, however, shows significant errors when compared against the EMT model.

7.2 Future development

Future development of PF RMS models comes in two categories: 1) Development of decoupled sequence controllers-based RMS models, and 2) Integration of deep reinforcement learning-based damping control into inner control loop

7.2.1 Development of decoupled sequence controller-based RMS models

As covered in [81-83], decoupled sequence controller has been developed to control the negative sequence response of the converter to achieve different goals. For Type IV WP, negative sequence current can be controlled and injected into the network to eliminate double frequency power oscillations during unbalanced conditions. The double frequency oscillation will appear on DC bus and therefore induce oscillations in torque on PMSG, which may cause damage in long term. Another use of decoupled sequence control is to inject negative sequence current proportional to negative sequence voltage to satisfy grid code requirements, such as German grid code described in [84].

Working decoupled sequence controller for Type IV EMT and RMS models have already been developed in PF, but due to time and length constraints they are not covered in this thesis. Fig. 7.1 shows the block diagram of the developed Type IV EMT WP model, Fig. 7.2 shows outer control loop of the negative sequence controller and Fig. 7.3 shows inner control loop of the negative sequence controller. The outer control loop generates reference current signals based on negative sequence voltage measurement on LV bus. The inner control loop is the same as positive sequence one, which calculates reference voltage signal based on current signal measurements. The calculated negative and positive voltage signals are added together then passed to the PWM converter for output.

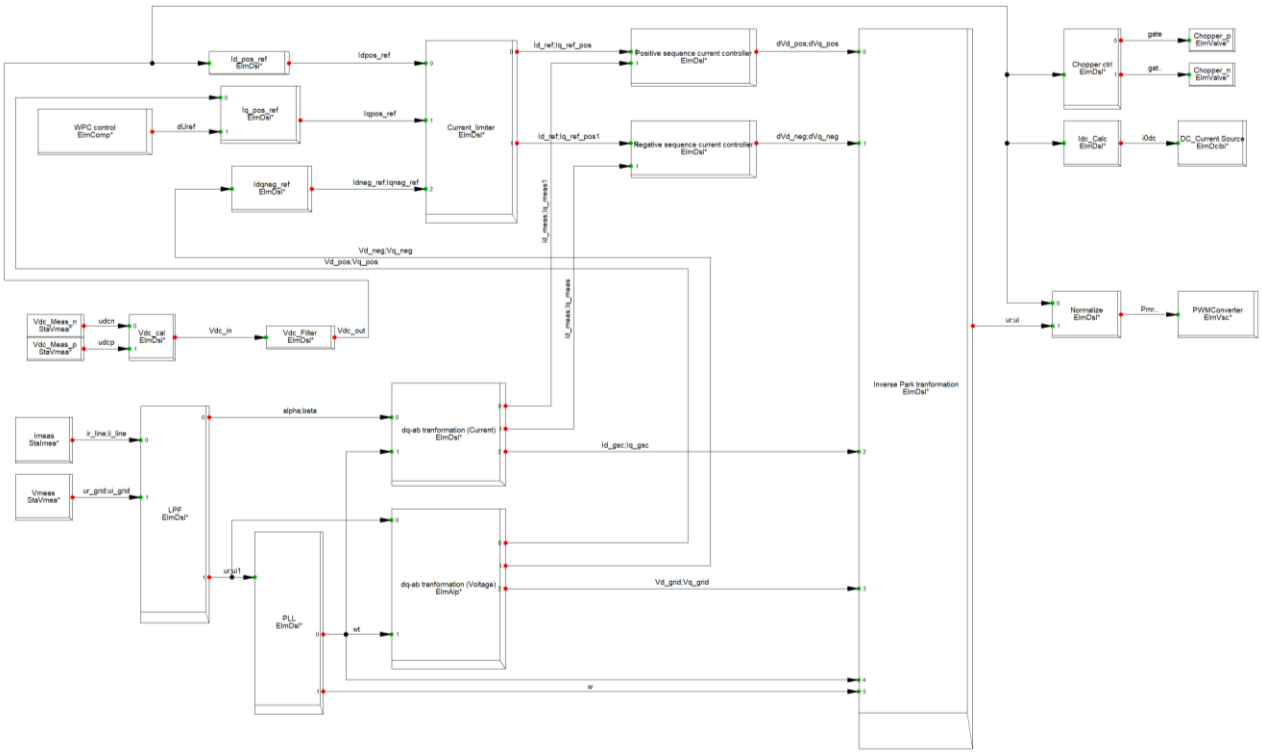

Fig. 7.1 Decoupled sequence controller for Type IV EMT WP model

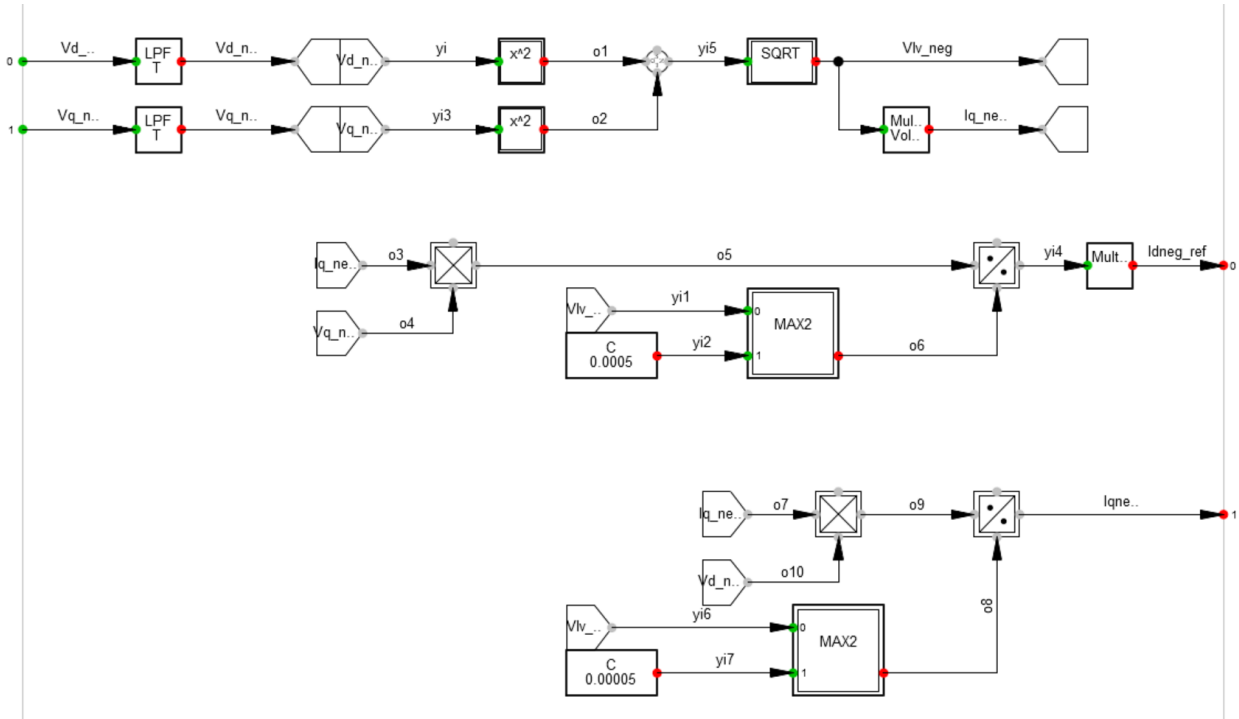

Fig. 7.2 Negative sequence reference current signal calculation

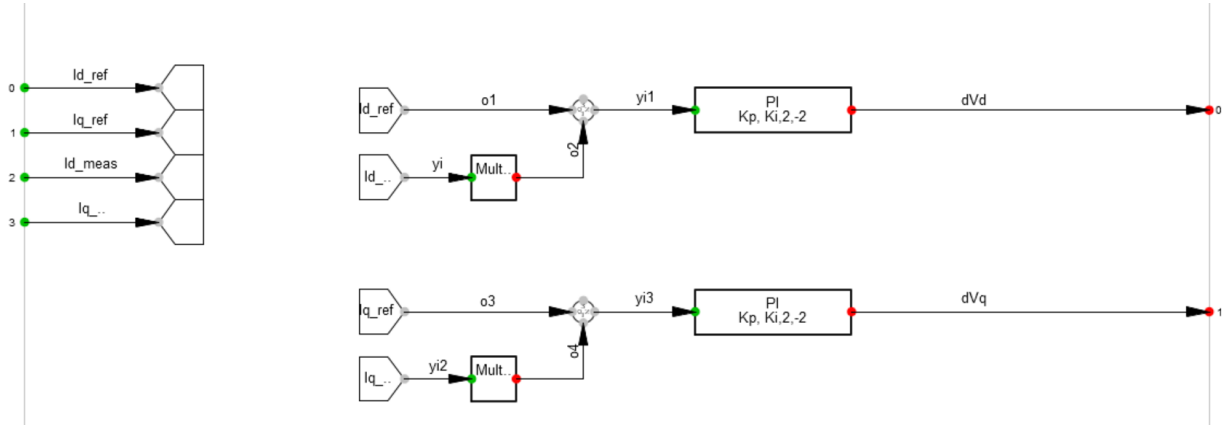

Fig. 7.3 Negative sequence reference voltage signal calculation

The negative sequence controller for Type IV RMS model is developed with the same idea, but with one major difference. Fig. 7.4 shows the negative sequence part of the GSC controller, and the calculated negative sequence voltage signals are fed directly into the PWM converter, instead of being mixed with positive sequence signals due to the nature of unbalanced RMS simulation.

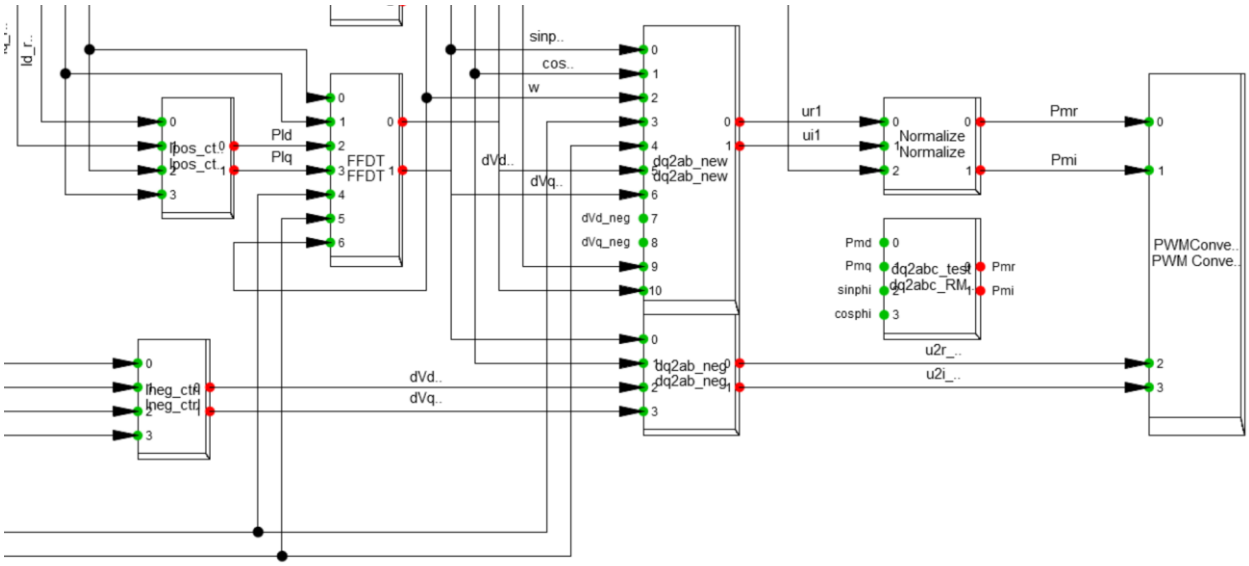

Fig. 7.4 Negative sequence controller for Type IV RMS WP model

The same idea applies to Type III WP models, due to time constraints the work is still unfinished. Based on results obtained from decoupled sequence controllers for Type IV WP models, Type III WP models could also provide accurate simulation results once finished.

7.2.2 Integration of deep reinforcement learning-based damping control into inner control loop

With the rapid development of machine learning, its application in IBRs has already been discussed, such as predicting wind turbine's response with deep learning in [85] and power forecasting for photovoltaic plants in [86]. Another project being worked on is using a deep reinforcement learning-based agent as an adaptive supplementary damping controller for Type IV WP models to improve stability under weak grid conditions.

Traditional mitigation strategies for Type IV WP includes modifying PLL and PI controller parameters. However, wind turbine's transient response might be negatively impacted. Supplementary damping controllers (SDCs) could also be used to resolve weak grid instability, but due to changing grid conditions, it may suffer from large resonance frequency shifts. By using deep reinforcement learning (DRL) agents, powerful function estimators can handle more complex tasks and environments than traditional RL approaches. DRL-Agents have demonstrated improved damping performance using advanced algorithms, such as asynchronous advantage actor-critic (A3C) for PSS parameter tuning in IEEE 10-machine 39-bus (10M39B) system, proximal policy optimization (PPO) for multiple low frequency oscillation (LFO) mode damping in the IEEE 16-machine 68-bus (16M68B) system and multi-agent DRL for coordinated PSS gain adjustment [87-89]. Due to the slow simulation speed of EMT models, as shown in CHAPTER 6, using of DRL-Agents in IBR instability mitigation is still in its early stages due to long training periods. With the development of highly efficient RMS models, implementation of DRL-Agent based SDCs becomes feasible. The design of a DRL-Agent based SDC is shown in Fig. 7.5. The DRL-Agent takes measurements from the electrical system, and generates reference current signals I_{dqSDC}, which is added to the reference current signals generated by outer control loop.

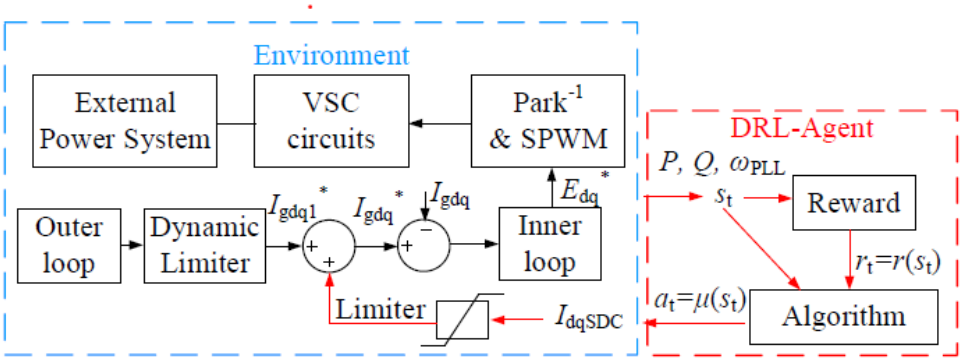

Fig. 7.5 DRL-Agent based SDC

The reward function of the DRL-Agent is designed as:

$$r_i = R_1(\omega_{PLL}) + R_2(P) + R_3(Q) \tag{7.1}$$

Where R_1, R_2 and R_3 are piecewise functions of PLL frequency measurement ω_{PLL}, real and reactive power output of the wind park P and Q, respectively. Based on the reward function r_1, the DRL-Agent adjusts its output to maximize rewards. The DDPG algorithm is used and its diagram is shown in Fig. 7.6.

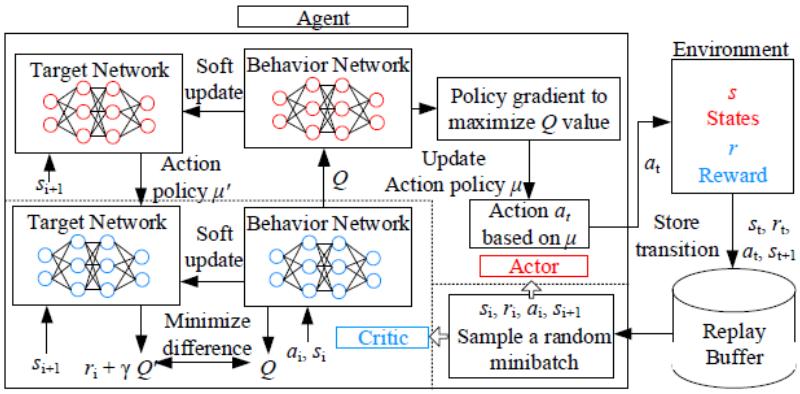

Fig. 7.6 DDPG framework diagram

Based on limited data obtained from another simulation software and simplified network, the DRL-Agent based SDC is working as expected and provides stable results under weak grid condition in a single WP infinite bus system. With highly efficient Type IV RMS WP models in PF, DRL-Agent based SDC could be integrated into the PF RMS model and verify its applicability in a large-scale network.

REFERENCES

[1] GWEC (2024) *Global wind report 2024*, Tech. rep., Global Wind Energy Council.

[2] GWEC (2024) *Global wind workforce outlook 2024 - 2028*, Tech. rep., Global Wind Energy Council.

[3] Munteanu, I., Bratcu, A.I., Cutululis, N.A., and Ceanga, E. (2008) *Optimal Control of Wind Energy Systems: Towards a global approach*, Springer Science & Business Media.

[4] Conroy, J.F. and Watson, R. (2008) *Frequency response capability of full converter wind turbine generators in comparison to conventional generation*. IEEE Transactions on Power Systems, 23 (2), 649–656.

[5] P. Pourbeik *et al*., "Generic Dynamic Models for Modeling Wind Power Plants and Other Renewable Technologies in Large-Scale Power System Studies," in *IEEE Transactions on Energy Conversion*, vol. 32, no. 3, pp. 1108-1116, Sept. 2017.

[6] A. Lorenzo-Bonache, A. Honrubia-Escribano, F. Jiménez-Buendía and E. Gómez-Lázaro, "Field Validation of Generic Type 4 Wind Turbine Models Based on IEC and WECC Guidelines," in *IEEE Transactions on Energy Conversion*, vol. 34, no. 2, pp. 933-941, June 2019.

[7] WECC Second Generation Wind Turbine Models, January 23, 2014.

[8] K. Clark, N. W. Miller, and J. J. Sanchez-Gasca, Modeling of GE Wind Turbine-Generators for Grid Studies, Version 4.5, General Electric International, Inc., New York, NY, USA, Apr. 2010.

[9] D. Gautam, V. Vittal and T. Harbour, "Impact of Increased Penetration of DFIG-Based Wind Turbine Generators on Transient and Small Signal Stability of Power Systems," in *IEEE Transactions on Power Systems*, vol. 24, no. 3, pp. 1426-1434, Aug. 2009.

[10] Honrubia-Escribano, E. Gómez-Lázaro, J. Fortmann, P. Sørensen, S. Martin-Martinez, "Generic dynamic wind turbine models for power system stability analysis: A comprehensive review," Renewable and Sustainable Energy Reviews, vol. 81, pp. 1939-1952, 2018.

[11] IEC 61400-27-1:2020. Wind energy generation systems - Part 27-1: Electrical simulation models - Generic models, International Standard, Rev. Edition 2, July 2020.

[12] J. Fortmann, S. Engelhardt, J. Kretschmann, C. Feltes and I. Erlich, "New Generic Model of DFG-Based Wind Turbines for RMS-Type Simulation," in IEEE Transactions on Energy Conversion, vol. 29, no. 1, pp. 110-118, March 2014.

[13] J. L. Rueda, A. W. Korai, J. C. Cepeda, I. Erlich and F. M. Gonzalez-Longatt, “Implementation of Simplified Models of DFIG-Based Wind Turbines for RMS-Type Simulation in DIgSILENT PowerFactory,” in PowerFactory Applications for Power System Analysis, 1, Springer, 2014, pp.197-220.

[14] *WECC Wind Power Plant Dynamic Modeling Guide prepared by: WECC Renewable Energy Modeling Task Force*, April 2014.

[15] P. Pourbeik, "Proposed Changes to the WECC WT4 Generic Model for Type 4 Wind Turbine Generators", Prepared under Subcontract No. NFT-1-11342-01 with NREL, Issued to WECC REMTF and IEC TC88 WG27 12/16/11; (last revised 8/29/12).

[16] P. Pourbeik, "Proposed Changes to the WECC WT3 Generic Model for Type 3 Wind Turbine Generators", Prepared under Subcontract No. NFT-1-11342-01 with NREL, Issued to WECC REMTF and IEC TC88 WG27 3/26/12; (last revised 8/29/12).

[17] I. Erlich, J. Kretschmann, J. Fortmann, S. Engelhardt and H. Wrede, "Modeling of wind turbines based on doubly-fed induction generators for power system stability studies", IEEE Trans. Power Syst., vol. 22, no. 3, pp. 909-919, Aug. 2007.

[18] X. Wang, L. Harnefors and F. Blaabjerg, "Unified impedance model of grid-connected voltage-source converters", *IEEE Trans. Power Electron.*, vol. 33, no. 2, pp. 1775-1787, Feb. 2018.

[19] X. He and H. Geng, "Transient Stability of Power Systems Integrated With Inverter-Based Generation," in *IEEE Transactions on Power Systems*, vol. 36, no. 1, pp. 553-556, Jan. 2021.

[20] D. Ramasubramanian, W. Wang, P. Pourbeik, E. Farantatos *et al*., "Positive sequence voltage source converter mathematical model for use in low short circuit systems," in *IET Gener. Transm. Distrib.*, vol. 14, no. 1, pp. 87-97, Jan. 2020.

[21] T. -T. Nguyen, T. Vu, T. Ortmeyer, G. Stefopoulos, G. Pedrick and J. MacDowell, "Real-time Modeling of Offshore Wind Turbines for Transient Simulation and Studies," *IECON 2021 – 47th Annual Conference of the IEEE Industrial Electronics Society*, Toronto, ON, Canada, 2021, pp. 1-6.

[22] P. Pourbeik, N. Etzel and S. Wang, "Model Validation of Large Wind Power Plants Through Field Testing," in *IEEE Transactions on Sustainable Energy*, vol. 9, no. 3, pp. 1212-1219, July 2018.

[23] N. Hatziargyriou et al., "Definition and Classification of Power System Stability – Revisited & Extended," in IEEE Transactions on Power Systems, vol. 36, no. 4, pp. 3271-3281, July 2021.

[24] Q. Hu, L. Fu, F. Ma, F. Ji and Y. Zhang, "Analogized Synchronous-Generator Model of PLL-Based VSC and Transient Synchronizing Stability of Converter Dominated Power System," in IEEE Transactions on Sustainable Energy, vol. 12, no. 2, pp. 1174-1185, April 2021.

[25] G. Wang, L. Fu, Q. Hu, C. Liu and Y. Ma, "Transient Synchronization Stability of Grid-Forming Converter During Grid Fault Considering Transient Switched Operation Mode," in *IEEE Transactions on Sustainable Energy*, vol. 14, no. 3, pp. 1504-1515, July 2023.

[26] W. Wang, G. M. Huang, D. Ramasubramanian and E. Farantatos, "Transient stability analysis and stability margin evaluation of phase-locked loop synchronised converter-based generators," in *IET Gener. Transm. Distrib.*, vol. 14, no. 22, pp. 5000–5010, July. 2020.

[27] B. Wen, D. Dong, D. Boroyevich, R. Burogs, P. Mattavelli and Z. Shen, "Impedance-based analysis of grid-synchronization stability for three phase paralleled converters", *IEEE Trans. Power Electron.*, vol. 31, no. 1, pp. 26-38, Jan. 2016.

[28] Q. Hu, L. Fu, F. Ma and F. Ji, "Large signal synchronizing instability of PLL-based VSC connected to weak AC grid", *IEEE Trans. Power Syst.*, vol. 34, no. 4, pp. 3220-3229, Jul. 2019.

[29] U. Karaagac *et al*., "A Generic EMT-Type Model for Wind Parks With Permanent Magnet Synchronous Generator Full Size Converter Wind Turbines," in *IEEE Power and Energy Technology Systems Journal*, vol. 6, no. 3, pp. 131-141, Sept. 2019

[30] T. Kauffmann, U. Karaagac, I. Kocar, S. Jensen, J. Mahseredjian, and E. Farantatos, "An accurate type III wind turbine generator short circuit model for protection applications," *IEEE Trans. Power Del.,* vol. 32, no. 6, pp. 2370-2379, Dec. 2017

[31] S. Huang, J. Yao, J. Pei, S. Chen, Y. Luo and Z. Chen, "Transient Synchronization Stability Improvement Control Strategy for Grid-Connected VSC Under Symmetrical Grid Fault," in *IEEE Transactions on Power Electronics*, vol. 37, no. 5, pp. 4957-4961, May 2022

[32] N. R. Ullah, T. Thiringer and D. Karlsson, "Voltage and transient stabilitysupport by wind farms complying with the E.ON Netz grid code", *IEEE Trans. Power Syst.*, vol. 22, no. 4, pp. 1647-1656, Nov. 2007.

[33] H. Yuan, H. Xin, L. Huang, Z. Wang and D. Wu, "Stability analysis and enhancement of type-4 wind turbines connected to very weak grids under severe voltage sags", *IEEE Trans. Energy Convers.*, vol. 34, no. 2, pp. 838-848, Jun. 2019.

[34] E.W. Kimbark, "Power system stability",vol2,6 edition, April, 67, John Wiley &sons edition

[35] A. Mechraoui and D. W. P. Thomas, "The influence of power swing on transmission line distance protection measurement of power and voltage phasor oscillation at the relaying point", *UPEC 93*, vol. 2, pp. 585-588, 93-September.

[36] C. V. Naray, "Influence of power swing on transmission line protection", *Brown Boveri REV.*, vol. 53, no. 1, pp. 841-848, Nov/Dec 1966.

[37] F. Ilar and Baden, "Innovations in the detection of power swing in electrical networks", *Brown Boveri REV.*, vol. 2-81, pp. 87-93.

[38] Z.D. Gad and G.B. Wang, "A new power swing block in distance protection based on a microcomputer- Principle and performance analyses", *International Conference in Advanced power system Control operation and management*, pp. 843-847, 1991-Nov.

[39] A. Mechraoui and D. W. P. Thomas, "A new blocking principle with phase and earth fault detection during fast power swings for distance protection," in *IEEE Transactions on Power Delivery*, vol. 10, no. 3, pp. 1242-1248, July 1995.

[40] J. Machowski and D. Nelles, "New power swing blocking method", Proc. Int. Conf. Developments in Power System Protection, pp. 218-221, 1997-Mar.

[41] "Application of Out-of-Step Protection Schemes for Generators", *Working Group J5 of the Rotating Machinery Subcommittee Power Systems Relaying Committee*.

[42] SEL Application Guide AG97-13, "SEL-321-5 Relay Out-Of-Step Logic," Daqing Hou, Shaojun Chen, and Steve Turner.

[43] O. Faucon, and Laurent Dousset, "Coordinated Defense Plan Protects Against Transient Instabilities," IEEE Computer Applications in Power, Vol 10, Issue 3, July 1997.

[44] V. Centeno, A.G. Phadke and A. Edris, "Adaptive out-of-step relay with phasor measurements", IEE Conf. Pub. No. 434, Developments in Power System Protection, London, 1997, pp. 210-213.

[45] Bahman Alinezhad, Hossein Kazemi Karegar, "Out-of-Step Protection Based on Equal Area Criterion", *IEEE Transactions on Power Systems*, vol.32, no.2, pp.968-977, 2017.

[46] M.C. Bozchalui, M. Sanaye-Pasand, "Out of step relaying using phasor measurement unit and equal area criterion", *2006 IEEE Power India Conference*, pp.6 pp.-, 2006.

[47] D. Tziouvaras and D. Hou, "Out-of-Step Protection Fundamentals and Advancements," Proc.30th Annual Western Protective Relay Conference, Spokane, WA, October 21-23, 2003.

[48] R. W. Kenyon, M. Bossart, M. Marković, K. Doubleday, R. Matsuda-Dunn, S. Mitova, et al., "Stability and control of power systems with high penetrations of inverter-based resources: An accessible review of current knowledge and open questions", *Solar Energy*, vol. 210, pp. 149-168, 2020.

[49] M. J. Reno, S. Brahma, A. Bidram and M. E. Ropp, "Influence of inverter-based resources on microgrid protection: Part 1: Microgrids in radial distribution systems", *IEEE Power and Energy Magazine*, vol. 19, no. 3, pp. 36-46, 2021.

[50] G. K and M. K. Jena, "A practical approach to inertia distribution monitoring and impact of inertia distribution on oscillation baselining study for renewable penetrated power grid", *IEEE Systems Journal*, pp. 1-9, 2022.

[51] R. Chowdhury and N. Fischer, "Transmission line protection for systems with inverter-based resources – part i: Problems", *IEEE Transactions on Power Delivery*, vol. 36, no. 4, pp. 2416-2425, 2021.

[52] J. C. Quispe and E. Orduña, "Transmission line protection challenges influenced by inverter-based resources: a review", *Protection and Control of Modern Power Systems*, vol. 7, no. 1, pp. 1-17, 2022.

[53] A. Fazanehrafat, S. A. M. Javadian, S. M. T. Batbaee and M. R. Haghifam, "Maintaining the recloser-fuse coordination in distribution systems in presence of DG by determining DG's size", *Proc. IET 9th International Conference on Developments in Power System Protection (DPSP)*, pp. 132-137, Mar. 2008.

[54] A. Girgis and S. M. Brahma, "Effect of distributed generation on protective device coordination in distribution system", *Proc. Large Engineering Systems Conference on Power Engineering*, pp. 115-119, Jul. 2001.

[55] S. Santoso and T. A. Short, "Identification of fuse and recloser operations in a radial distribution systems", *IEEE Trans. on Power Delivery*, vol. 22, no. 4, pp. 2370-2377, Oct. 2007.

[56] S. Gautam and S. Brahma, "Out-of-step blocking function in distance relay using mathematical morphology", *IET Gen. Transm. Distrib.*, vol. 6, no. 4, pp. 313-319, Apr. 2012.

[57] U. B. Parikh, N. G. Chothani and B. R. Bhalja, "New support vector machine-based digital relaying scheme for discrimination between power swing and fault", *IET Gen. Transm. Distrib.*, vol. 8, no. 1, pp. 17-25, Jan. 2014.

[58] P. K. Nayak, A. K. Pradhan and P. Bajpai, "A fault detection technique for the series-compensated line during power swing", *IEEE Trans. Power Del.*, vol. 28, no. 2, pp. 714-722, Apr. 2013.

[59] P. Kundu and A. K. Pradhan, "Synchro phasor-assisted zone 3 operation", *IEEE Trans. Power Del.*, vol. 29, no. 2, pp. 660-667, Apr. 2014.

[60] P. K. Nayak, A. K. Pradhan and P. Bajpai, "Secured zone 3 protection during stressed condition", *IEEE Trans. Power Del.*, vol. 30, no. 1, pp. 89-96, Jul. 2015.

[61] N. Yorino, H. Sasaki, Y. Tamura and R. Yokoyama, "A generalized analysis method of auto-parametric resonances in power systems", *IEEE Trans. Power Syst.*, vol. 4, no. 3, pp. 1057-1064, Aug. 1989.

[62] T. Athey, R. Podmore and S. Virmani, "A practical method for direct analysis of transient stability", *IEEE Trans. Power App. Syst.*, vol. PAS-98, pp. 573-584, 1979.

[63] G. A. Maria, C. Tang and J. Kim, "Hybrid transient stability analysis", *IEEE Trans. Power Syst.*, vol. 5, no. 2, pp. 384-393, May 1990.

[64] Y. Xue, L. Wehenkel, R. Belhomme, P. Rous-Seaux, M. Pavella, E. Euxibie, et al., "Extended equal area criterion revised", *IEEE Trans. Power Syst.*, vol. 7, no. 3, pp. 1012-1022, Aug. 1992.

[65] G. D. Irisarri, G. C. Ejebe and J. G. Waight, "Efficient solution for equilibrium points in transient energy function analysis", *IEEE Trans. Power Syst.*, vol. 9, no. 2, pp. 693-699, May 1994.

[66] P. Kundur and J. Paserba, "Definition and classification of power system stability", *IEEE Trans. on Power Systems*, vol. 19, no. 2, pp. 1387-1401, 2004.

[67] R. T. Treinen, V. Vittal and W. Kliemann, "An improved technique to determine the controlling unstable equilibrium point in a power system", *IEEE Trans. Circuits Syst. I Reg. Papers*, vol. 43, no. 4, pp. 313-323, Apr. 1996.

[68] C. C. Inwai, W. J. Lee, P. Fuangfoo et al., "System impact study for the interconnection of wind generation and utility system", *IEEE Trans. on Industry Applications*, vol. 41, no. 1, pp. 163-168, 2005.

[69] D. J. Trudnowski, A. Gentile, J. M. Khan and E. M. Petritz, "Fixed-speed wind-generator and wind-park modelling for transient stability studies", *IEEE Trans. on Power Systems*, vol. 19, no. 4, pp. 1911-1917, 2004.

[70] L. Holdsworth, X. G. Wu, J. B. Ekanayake and N. Jenkins, "Comparison of fixed speed and doubly-fed induction wind turbines during power system disturbances", *IEE Proc. Generation Transmission and Distribution*, vol. 150, no. 3, pp. 343-352, 2003.

[71] K. C. Divya and P. S. Nagendra Rao, "Study of dynamic behaviour of grid connected induction generators", *IEEE Power Engineering Society General Meeting*, pp. 2200-2205, 2004.

[72] W. S. Mota, L. S. Barros, F. M. P. Pamplona, A. N. Epaminondas, E. R. B. Filho and A. A. F. Santos, "Wind generation dynamic simulation connected to an electric power system", *IEEE/PES Transmission & Distribution Conference & Exposition*, pp. 179-184, 2004.

[73] A. A. Fouad and Vijay Vittal, Power System Transient Stability Analysis Using the Transient Energy Function Method, NJ 07632: Prentice Hall Englewood Cliffs, 1992.

[74] Z. Zou, B. D. Besheli, R. Rosso, M. Liserre and X. Wang, "Interactions between two phase-locked loop synchronized grid converters", *IEEE Trans. Ind. Appl.*, vol. 57, no. 4, pp. 3935-3947, Jul.-Aug. 2021.

[75] D. Dong, B. Wen, D. Boroyevich, P. Mattavelli and Y. Xue, "Analysis of phase-locked loop low-frequency stability in three-phase grid- connected power converters considering impedance interactions", *IEEE Trans. Ind. Electron.*, vol. 62, no. 1, pp. 310-321, Jan. 2015.

[76] X. Wang, M. G. Taul, H. Wu, Y. Liao, F. Blaabjerg and L. Harnefors, "Grid synchronization stability of converter-based resources-An overview", *IEEE Open J. Ind. Appl.*, vol. 1, pp. 115-134, Aug. 2020.

[77] O. R. Teodorescu, C. L. Bak, F. Iov and P. C, "Instability of wind turbine converters during current injection to low voltage grid faults and PLL frequency-based stability solution", *IEEE Trans. Power Syst.*, vol. 29, no. 4, pp. 1683-1691, Jul. 2014.

[78] H. Wu and X. Wang, "Design-oriented transient stability analysis of PLL-synchronized voltage-source converters", *IEEE Trans. Power Electron.*, vol. 35, no. 4, pp. 3573-3589, Apr. 2020.

[79] Y. Zhang, C. Zhang and X. Cai, " Large-signal grid-synchronization stability analysis of PLL-based VSCs using Lyapunov's direct method", *IEEE Trans. Power Syst.*, vol. 37, no. 1, pp. 788-791, Jan. 2022.

[80] Y. Ma, D. Zhu, Z. Zhang, X. Zou, J. Hu and Y. Kang, "Modeling and Transient Stability Analysis for Type-3 Wind Turbines Using Singular Perturbation and Lyapunov Methods", *IEEE Trans. Ind. Electron.*, vol. 70, no. 8, pp. 8075-8086, Aug. 2023.

[81] U. Karaagac, J. Mahseredjian, H. Gras, H. Saad, J. Peralta and L. D. Bellomo, *Simulation models for wind parks with variable speed wind turbines in EMTP-RV*, Apr. 2019.

[82] T. Demiray, F. Milano and G. Andersson, "Dynamic phasor modeling of the doubly-fed induction generator under unbalanced conditions", *Proc. IEEE Power Tech*, pp. 1049-1054, 2007.

[83] T. Kauffmann *et al*., "Short-Circuit Model for Type-IV Wind Turbine Generators with Decoupled Sequence Control," in *IEEE Transactions on Power Delivery*, vol. 34, no. 5, pp. 1998-2007, Oct. 2019.

[84] Transmission Code 2007. *Network and System Rules of the German Transmission System Operators*.

[85] S. Woo, J. Park, J. Park and L. Manuel, "Wind Field-Based Short-Term Turbine Response Forecasting by Stacked Dilated Convolutional LSTMs," in *IEEE Transactions on Sustainable Energy*, vol. 11, no. 4, pp. 2294-2304, Oct. 2020.

[86] A. G. Kavaz and A. Karazor, "Solar Power Forecasting by Machine Learning Methods in a Co-located Wind and Photovoltaic Plant," *2023 12th International Conference on Power Science and Engineering (ICPSE)*, Eskisehir, Turkiye, 2023, pp. 55-59.

[87] G. Zhang et al., “Deep Reinforcement Learning-Based Approach for Proportional Resonance Power System Stabilizer to Prevent Ultra-Low-Frequency Oscillations,” IEEE Trans. Smart Grid, vol. 11, no. 6, pp. 5260-5272, Nov. 2020.

[88] G. Zhang, W. Hu, J. Zhao, D. Cao, Z. Chen and F. Blaabjerg, “A Novel Deep Reinforcement Learning Enabled Multi-Band PSS for Multi-Mode Oscillation Control,” IEEE Trans. Power Systems, vol. 36, no. 4, pp. 3794-3797, July 2021.

[89] G. Zhang et al., “A Multiagent Deep Reinforcement Learning-Enabled Dual-Branch Damping Controller for Multimode Oscillation,” IEEE Trans. Control Syst. Technol., vol. 31, no. 1, pp. 483-492, Jan. 2023.